

**NASA
Technical
Paper
2995**

1990

Panel Methods—An Introduction

Larry L. Erickson
*Ames Research Center
Moffett Field, California*



National Aeronautics and
Space Administration
Office of Management
Scientific and Technical
Information Division

TABLE OF CONTENTS

	Page
SUMMARY	1
1. INTRODUCTION	1
2. WHAT PANEL METHODS CAN AND CANNOT DO	2
3. COMMON ROOTS OF PANEL METHODS	3
4. DISTINCTIONS BETWEEN PANEL CODES	6
Surface Geometry	7
Singularity Distributions	7
Continuity of Doublet Strength	8
Summary of Methods	9
5. MODELING	10
Mass-Flux and Velocity Boundary Conditions	10
Interior Potential	12
Wakes	14
6. TRANSONIC FLOW	15
7. CONCLUDING REMARKS	16
APPENDIX A – PAN AIR IMPLEMENTATION OF SECTION 3 MATERIAL	19
Panel and Network Singularity Parameters	19
Panel Influence Coefficient Matrices	20
Assembled Influence Coefficients	21
The Aerodynamic Influence Coefficient Matrix Equation	21
APPENDIX B – EVALUATION OF INFLUENCE-COEFFICIENT SURFACE INTEGRALS	23
Velocity Owing to a Flat, Linear Source Panel	23
Velocity Owing to a Flat, Quadratic Doublet Panel	25
Evaluation of $H(1,1,3)$	26
The Jump Property of $hH(1,1,3)$	27
The Line Integral $F(1,1,1)$	28
APPENDIX C – IMPROPER INTEGRALS AND THEIR FINITE PART	29
Integration Before Setting $z = 0$	29
Integration After Setting $z = 0$	30
REFERENCES	31
TABLE	35
FIGURES	36

SUMMARY

Panel methods are numerical schemes for solving (the Prandtl-Glauert equation) for linear, inviscid, irrotational flow about aircraft flying at subsonic or supersonic speeds. The tools at the panel-method user's disposal are (1) surface panels of source-doublet-vorticity distributions that can represent nearly arbitrary geometry, and (2) extremely versatile boundary condition capabilities that can frequently be used for creative modeling. This report discusses panel-method capabilities and limitations, basic concepts common to all panel-method codes, different choices that have been made in the implementation of these concepts into working computer programs, and various modeling techniques involving boundary conditions, jump properties, and trailing wakes. An approach for extending the method to nonlinear transonic flow is also presented.

Three appendixes supplement the main text. In appendix A, additional detail is provided on how the basic concepts are implemented into a specific computer program (PAN AIR). In appendix B, we show how to evaluate analytically the fundamental surface integral that arises in the expressions for influence-coefficients, and evaluate its jump property. In appendix C a simple example is used to illustrate the so-called finite part of improper integrals.

1. INTRODUCTION

Panel methods are numerical schemes for solving (the Prandtl-Glauert equation) for linear, inviscid, irrotational flow at subsonic or supersonic free-stream Mach numbers. Currently, panel-method codes are the only codes commonly in use that are sufficiently developed for routinely analyzing the complex geometries of realistic aircraft. The objective of this report is to give the reader some idea of what panel methods can and cannot do, to describe their common roots, to describe the differences between various specific implementations, and to show some example applications. In addition, recent progress in solving nonlinear transonic flow problems by combining portions of panel-method technology with other numerical techniques, is described. This material is followed by three appendixes that contain additional details: appendix A describes how the basic ideas common to all panel methods are actually implemented in a specific code; appendix B shows how to evaluate some of the integrals that arise in the influence-coefficient equations; and appendix C discusses the so-called finite part of improper integrals.

There are fundamental analytic solutions to the Prandtl-Glauert equation known as source, doublet, and vorticity singularities. Panel methods are based on the principle of superimposing surface distributions of these singularities over small quadrilateral portions, called panels, of the aircraft surface, or to some approximation to the aircraft surface. The resulting distribution of superimposed singularities automatically satisfies the Prandtl-Glauert equation. To make the solution correspond to the desired geometry, boundary conditions are imposed at discrete points of the panels. (Mathematicians refer to these discrete points as collocation points; panel-method users refer to them as control points.)

Panel codes are often described as being lower-order or higher-order. The term lower-order refers to the use of constant-strength singularity distributions over each panel, and the panels are usually flat. Higher-order codes use something of higher order than constant, for example, a linear or quadratic singularity distribution, and sometimes curved panels.

Panel methods were initially developed as lower-order methods for incompressible and subsonic flows (e.g., refs. 1, 2; see ref. 3 for a review of panel methods existing through about 1976). The first successful panel method for supersonic flow became available in the mid-1960s (refs. 4, 5). This was also a lower-order method, and is variously referred to as the constant-pressure panel method, or the Woodward-Carmichael method.

The panel methods for three-dimensional subsonic flow allowed the actual vehicle surface to be paneled, whereas the Woodward-Carmichael method was more severely restricted in the placement of the panels. For example, the wing was a planar array of panels, the body (fuselage) volume was modeled with a line distribution of source and doublet singularities (resulting in a body-of-revolution) and the body boundary conditions were imposed with a cylindrical "interference" shell of wing-type panels. This representation was later extended to include multiple wing-body components (ref. 6), but was still restricted to the planar panel representation. These two extremes of actual-surface models and mean-surface models (Woodward-Carmichael) are illustrated in figure 1.

The mean-surface model used in the Woodward-Carmichael panel method was a consequence of numerical stability problems that arose in supersonic flow. The constant-strength, elementary horseshoe vortex singularity distribution (producing a constant pressure over each panel) often produced unstable numerical behavior (the solutions would "blow-up") when a panel was inclined to

a supersonic flow. The method worked only when all the panels were kept parallel to the free-stream flow. This required that angle of attack, wing thickness, camber, and twist be simulated through the boundary conditions; that is, it was necessary to have the panels generate flow perpendicular to themselves and thereby turn the flow through the desired angles, as is done in classic thin-wing theory. As a consequence of this restricted geometric model, several new approaches to the supersonic problem were pursued in the 1970s.

The first of these was also due to Woodward; it evolved into the series of computer programs known as USSAERO (ref. 7). For fuselage panels, USSAERO uses constant-strength source singularities. Wing panels use elementary horseshoe-vortex singularities whose strength distribution varies linearly in the chordwise direction and is constant in the spanwise direction. Although this representation gave an improved modeling capability, numerical problems would still often occur when the wing panels were inclined to a supersonic free-stream flow.

Another approach, developed by Morino and his associates, uses a superposition of constant-strength sources and doublets on hyperboloidal panels. The constant strength doublets produce a velocity field that is identical to that produced by line-vortex elements, having the same strength as the doublet panel, placed head to tail around the panel perimeter (a so-called ring-vortex panel). This method is available in the computer program called SOUSSA; it too is unable to handle the steady supersonic case (ref. 8, pp. 2-20; private communication, L. Morino, Feb. 1981).

The key to eliminating the numerical stability problems associated with supersonic flow, was to use doublet distributions that were continuous over the entire surface of the aircraft. This approach, using quadratic doublet distributions (equivalent to linear vorticity distributions) was first used in the PAN AIR code (refs. 9-14) and its pilot code predecessor (ref. 15). It has since been implemented in the European version of PAN AIR, called HISSS (ref. 16). The continuous-doublet distribution eliminates the appearance of spurious line-vortex terms at the panel edges, which was the cause of the numerical stability problems in the earlier approaches.

Within the limitations of the Prandtl-Glauert equation, the higher-order singularity distributions used in the PAN AIR and HISSS codes allowed the actual-surface paneling models, long in use for subsonic flow, to also be used for supersonic flow. It also had a very beneficial side effect: the numerical solutions turned out to be much less sensitive to the size, shape, and arrangement of the panel-

ing than in earlier methods, including the subsonic-only methods. Partly for this reason, continuous quadratic doublets were incorporated into the subsonic-only MCAERO code (ref. 17). These advantages did not come free however. The higher-order distributions require much more analytic work to derive the influence-coefficient equations, and demand many more arithmetic operations than the simpler lower-order (constant-strength) methods, which results in significantly higher run costs.

It was subsequently discovered that for subsonic flow, setting the perturbation potential to zero at the interior side of panels, in conjunction with the original lower-order singularity distributions, also reduced the solution sensitivity to variations in panel layout. This led to a renewed interest in the lower-order methods, resulting in the VSAERO (refs. 18, 19) and QUADPAN (refs. 20, 21) codes. QUADPAN was later revised to handle the supersonic case by changing its constant-strength doublets to continuous linear doublets.

2. WHAT PANEL METHODS CAN AND CANNOT DO

Panel-method-based computer programs are currently the workhorse codes for predicting the aerodynamics of complete configurations. Representative aircraft examples that have been analyzed with panel method codes are shown in figure 2. Although such codes are routinely used to analyze very complicated geometries, they do so at the expense of ignoring much fluid physics. The equation that panel codes solve is the Prandtl-Glauert equation. For steady subsonic flow this equation is usually written as

$$\tilde{\nabla}^2 \phi = (1 - M_\infty^2) \phi_{xx} + \phi_{yy} + \phi_{zz} = 0 \quad (1)$$

and for supersonic flow it is sometimes multiplied by -1 ,

$$-\tilde{\nabla}^2 \phi = (M_\infty^2 - 1) \phi_{xx} - \phi_{yy} - \phi_{zz} = 0 \quad (2)$$

where M_∞ is the free-stream Mach number and ϕ is the perturbation velocity potential.

For subsonic free-stream flow, equations (1) and (2) are elliptic, being similar to Laplace's equation. Such equation types have the property that any disturbance at some point is felt everywhere in the flow field (although the effect usually dies out rapidly with distance). For supersonic free-stream flow the equations are hyperbolic, with the x -derivative term behaving like time in the wave equation. Solutions for the supersonic case are fundamentally different, disturbances having restricted

zones of influence (or in Von Karman's words, zones of "silence," or "forbidden signals"; ref. 22). The disturbances only propagate downstream, along rays defined by the Mach cones (characteristic surfaces), reflecting off downstream geometry and interfering in a wave-like manner with other disturbances.

The Prandtl-Glauert equation is the simplest form of the fluid-flow equations that contain compressibility effects (i.e., the effect of Mach number on fluid density). It is obtained from the more general Navier-Stokes equation by (1) neglecting all the viscous and heat-transfer terms; (2) assuming that the flow is irrotational, thereby admitting the introduction of a velocity potential; and (3) discarding all nonlinear terms. This restricts the flow to be inviscid, irrotational, and linear. Often, the flow is also assumed to be steady. Physically, these restrictions mean that important flow behavior such as separation, skin-friction drag, and transonic shocks are not predicted with panel methods. Items that are predicted include drag-due-to-lift (often called induced drag for subsonic flow, and vortex drag for supersonic flow), and wave drag.

Wave drag is predicted because the Prandtl-Glauert equation admits solutions that approximate the weak-shock solutions of shock-expansion theory (ref. 23, pp. 215, 216). A simple example is the supersonic flow over a thin wedge (fig. 3(b)). For small wedge (deflection) angles, the shock is attached at the wedge leading edge, forms at an angle very nearly to that of the Mach angle, and the flow remains supersonic on the downstream side of the shock. The limiting case for these weak shocks, in which the shocks form at exactly the Mach angle, is predicted by the Prandtl-Glauert equation.

The absence of any explicit viscous effects causes subsonic flow solutions to be non-unique unless a Kutta condition at sharp trailing edges is somehow imposed (ref. 24, pp. 80, 81). This is done with the addition of some type of wake panels that trail downstream from lifting-surface trailing edges (fig. 3(a)), causing the flow to separate smoothly from these edges and allowing the potential to jump (be discontinuous) across the wake. Most panel methods require the user to assume the shape and position of the wakes. For a simple wing body this poses no difficulty, the wake position being relatively unimportant. However, for multiple-lifting-surface configurations, the wake placement is important since it affects the flow experienced by downstream geometry. A few codes iteratively solve for the wake shape and location.

Because panel methods are able to treat complete configurations, they have often been used in combination with other methods to approximately account for addi-

tional physics neglected by the Prandtl-Glauert equation. One fairly common practice is to include the presence of the wing boundary layer (ref. 25). The basic idea is to use the pressure distribution from the panel-code solution as input to a boundary-layer code and compute the displacement thickness. This incremental thickness is then represented in a second run of the panel code. This is usually done in one of two ways, as illustrated in figure 4 (ref. 25). The first is to actually recompute the wing surface coordinates and the new wing-body intersection by adding the displacement thickness to the actual wing geometry. An alternative approach is to use "blowing," in which the source strengths of the wing panels are adjusted such that each panel ejects (or sucks) enough fluid to cause the resultant flow field to be approximately displaced by the displacement thickness. For either approach, the resulting change in actual or apparent wing shape has two effects: it reduces the effective camber of a cambered wing and it increases the wing thickness. For a specified angle of attack, the primary aerodynamic effect of these changes is a reduced lift owing to the reduced camber. The second, but usually less important effect, is a slight increase in lift owing to the increased wing thickness.

Another example is the coupling of panel codes to propulsion codes. In reference 26, the PAN AIR code is coupled to a parabolized Navier-Stokes propulsion code. The purpose was to account for the viscous, high-energy, exhaust-flow effect on the aerodynamic flow about the complete aircraft.

Panel-method codes have also been built to model the flow separation that occurs off highly swept wings with sharp leading edges (refs. 27, 28). In these codes, wake panels emanate from the wing leading edge, as well as from the trailing edge (fig. 5). Iterative techniques are used to solve for the correct shape and position of the leading-edge wake panels. The criteria to be satisfied are (1) that the Kutta condition be enforced and (2) that the entire wake surface be a stream surface (i.e., no flow crosses it, and it supports no pressure jump).

3. COMMON ROOTS OF PANEL METHODS

As indicated in section 2, panel methods rely on surface distributions of sources, doublets, and vorticity. We will see later that doublet and vortex distributions are related. Since surface vorticity is a vector and a doublet is a scalar, it is often easier to work with doublets than with vorticity, and then compute the vorticity from the doublet-strength distribution. Most higher-order panel-method codes take this approach.

It can be verified by direct substitution, that the following expressions, called unit point sources and doublets, respectively, satisfy the Prandtl-Glauert equation (eqs. (1) or (2)).

Point source:

$$\phi_P^S(\vec{x}_Q) = \frac{-1}{R(\vec{x}_P, \vec{x}_Q)} \quad (3)$$

Point doublet:

$$\phi_P^D(\vec{x}_Q) = \hat{n} \cdot \vec{\nabla}_Q \frac{1}{R(\vec{x}_P, \vec{x}_Q)} = \hat{n} \cdot \frac{-\vec{R}(\vec{x}_P, \vec{x}_Q)}{R^3} \quad (4)$$

where the so-called hyperbolic distance R is given by

$$R = \sqrt{(x_Q - x_P)^2 + \beta^2 [(y_Q - y_P)^2 + (z_Q - z_P)^2]} \quad (5a)$$

where

$$\beta^2 = 1 - M_\infty^2 \quad (5b)$$

In these expressions, point P is the influenced point in space having coordinates $\vec{x}_P = (x_P, y_P, z_P)$ and point Q is the influencing point $\vec{x}_Q = (x_Q, y_Q, z_Q)$ at which the unit point source or doublet is located (see fig. 6). There is an elemental area dS_Q associated with the doublet, and the doublet axis is normal to this area. (Recall from elementary fluid mechanics that a doublet can be thought of as a source-sink pair approaching each other along an axis. This definition of a doublet produces the same result as eq. (4).) The subscript Q on the scaled gradient operator means that the derivatives are to be taken with respect to the coordinates of point Q , not point P .

For incompressible flow, R becomes simply the geometric distance between the two points P and Q . Equation (3) then tells us that a point source at Q produces a disturbance at P that diminishes inversely as the distance between the two points. The meaning of equation (4) is not so obvious until one works out the expression indicated by the dot product. If one chooses the xyz coordinate system at point Q as shown in figure 6, then the unit normal \hat{n} equals the unit vector \mathbf{k} and equation (4) becomes simply

$$\phi_P^D = \frac{-\sin \theta}{R^2} \quad (6)$$

This form clearly shows the directional properties of a point doublet and reveals that a doublet disturbance dies off at least as rapidly as the inverse of the distance squared.

Since the Prandtl-Glauert equation is a linear partial differential equation, sums of the source and doublet solutions are also solutions. Thus, panel methods are usually thought of as superposition methods, and, hence, are restricted to linear problems. There is a more general approach, however, that, while containing superposition as a special case, can also be used to solve nonlinear problems. In section 6 we will take a look at how panel-method technology can be combined with other techniques to solve the nonlinear full-potential equation, so it is advantageous to look at this more general approach, known as Green's third theorem (ref. 29, p. 21, eq. (7)).

In reference 29, the derivation corresponds to incompressible potential flow; in reference 30, this is generalized to the compressible case. The result is the following identity:

$$\begin{aligned} \phi_P \equiv & \iint_S [\sigma(\vec{x}_Q) K_\sigma(\vec{x}_Q, \vec{x}_P) + \mu(\vec{x}_Q) K_\mu(\vec{x}_Q, \vec{x}_P)] dS_Q \\ & + \iiint_V (\vec{\nabla}^2 \phi) K_\sigma(\vec{x}, \vec{x}_P) dV \end{aligned} \quad (7)$$

where

$$K_\sigma(\vec{x}_Q, \vec{x}_P) = \frac{1}{k} \phi_P^S(\vec{x}_Q)$$

$$K_\mu(\vec{x}_Q, \vec{x}_P) = \frac{1}{k} \phi_P^D(\vec{x}_Q)$$

$$K_\sigma(\vec{x}, \vec{x}_P) = \frac{1}{k} \phi_P^S(\vec{x})$$

$$dV = dx dy dz$$

$$\sigma = \Delta(\hat{n} \cdot \vec{w})$$

$$\mu = \Delta \phi$$

$$\vec{w} = (\beta^2 u, v, w) = (\beta^2 \phi_x, \phi_y, \phi_z) = \vec{\nabla} \phi$$

In the above equations σ is the source strength and μ is the doublet strength at any point Q , on the surface S , which in our case will be all (for subsonic flow) or part (for supersonic flow) of the aircraft surface and wakes. These strengths are equal to jumps (discontinuities) across the panels of certain flow properties. The source strength equals the jump in the normal component of the mass-flux vector \vec{w} . The doublet strength equals the jump in

potential, and the gradient of the doublet strength equals the jump in tangential component of velocity. The values of these strengths are the (as yet unknown) amplitudes of the source and doublet singularity solutions appearing in equations (3) and (4). Here, these source and doublet solutions, when multiplied by a constant k^{-1} , are denoted as K_σ and K_μ , respectively (K is used to denote that the singularities are called kernels). For $M_\infty < 1$, $k = 4\pi$, and S is the entire surface of the aircraft and wake(s). For $M_\infty > 1$, $k = 2\pi$, and S is that portion of the aircraft surface and wake(s) that lies in the upstream Mach cone emanating from the influenced point P .

Equation (7) shows us that the velocity potential at point P is related to the source and doublet distributions on S , and to the spatial distribution of $\tilde{\nabla}^2 \phi$ in the volume V bounded (wetted by) both sides of S . If ϕ_P is constructed according to the surface integral terms in equation (7), that is,

$$\phi_P = \iint_S [\sigma K_\sigma + \mu K_\mu] dS_Q \quad (9)$$

then, because equation (7) is an identity, it follows that

$$\iiint_V (\tilde{\nabla}^2 \phi) K_\sigma dV = 0 \quad (10)$$

Since K_σ is a function of the arbitrary point P , $\tilde{\nabla}^2 \phi$ must be zero. Thus, construction of ϕ_P according to equation (9) implies that equations (1) and (2), the Prandtl-Glauert equation, has been satisfied throughout V .

Equation (9) is the basic starting formula for panel methods using sources and doublets. If the source and doublet strength distribution is known (we will see how this is done later), then the velocity at point P is obtained from equation (9) by differentiating with respect to the coordinates at P , that is

$$\tilde{v}_P = \tilde{\nabla}_P \phi_P = \iint_S [\sigma \tilde{\nabla}_P K_\sigma + \mu \tilde{\nabla}_P K_\mu] dS_Q \quad (11)$$

Equations (9) and (11) are used to generate influence-coefficient equations that relate source and doublet strengths at particular points Q on the surface S to the potential and velocity at field points P . The basic idea is to break S into a collection of panels Σ and to assume a functional form for σ and μ over each panel. For example, a constant-strength source-doublet panel with index j is given simply by

$$\sigma(\vec{x}_j) = \sigma_j(\xi, \eta) = \lambda_j^S \quad (12a)$$

$$\mu(\vec{x}_j) = \mu_j(\xi, \eta) = \lambda_j^D \quad (12b)$$

where the unknown constants λ_j^S and λ_j^D are called source and doublet singularity parameters, respectively, for panel j , and (ξ, η) are local surface coordinates associated with the panel.

Once the functional form for $\sigma_j(\xi, \eta)$ and $\mu_j(\xi, \eta)$ are specified, equations (9) and (11) can be integrated over each panel (a nontrivial task) so that ϕ_P and \tilde{v}_P are expressions involving only the unknown singularity parameters. If P is made a control point (a panel point at which a boundary condition will be imposed) with index i , equations (9) and (11) give the potential and velocity at that point in terms of (as influenced by) the source and doublet distributions of the single panel j (see fig. 7). Note that the fixed point P and the variable point Q of the analytic formulation correspond to control point i and panel j , respectively, in the discretized implementation. Summing the effects from all the panels on the aircraft surface gives the potential and velocity at control point i in terms of the total number (N) of singularity parameters.

If \tilde{v}_{ij} denotes the velocity at control point i , owing to the source-doublet distributions at panel j , then the velocity at point i owing to all N panels is

$$\tilde{V}_i = \tilde{V}_\infty + \sum_{j=1}^N \tilde{v}_{ij} \quad (13)$$

If the panel associated with control point i is to be a solid (impermeable) panel represented by a zero normal component of the total velocity, then the boundary condition is

$$\tilde{V}_i \cdot \hat{n}_i = \left(\tilde{V}_\infty + \sum_{j=1}^N \tilde{v}_{ij} \right) \cdot \hat{n}_i = 0 \quad (14)$$

Thus, for control point i , we have

$$\sum_{j=1}^N \tilde{v}_{ij} \cdot \hat{n}_i = -\tilde{V}_\infty \cdot \hat{n}_i \quad (15)$$

and since the \tilde{v}_{ij} are known (from eq. (11)) in terms of the N singularity parameters, equation (15) can ultimately be expressed as the single equation

$$\sum_{j=1}^N \text{VIC}_{ij} \lambda_j = b_i \quad (16)$$

where the VIC_{ij} are called velocity influence coefficients and $b_i = -\vec{V}_\infty \cdot \hat{n}_i$.

Repeating the process for a total of N control points and applying boundary conditions at each of these points leads to the equation

$$[\text{AIC}]\{\lambda\} = \{b\} \quad (17)$$

In this equation, $[\text{AIC}]$ is called the matrix of aerodynamic influence-coefficients, $\{\lambda\}$ is the vector of unknown singularity parameters, and the elements of $\{b\}$, the so-called right-hand-side quantities, are known from the boundary conditions. Solving for the singularity parameters then makes it possible to compute (from eqs. (9) and (11)) the potential and velocity distributions, and hence the pressures acting at the paneled approximation to the surface S . Integrating the pressures and their moments yields the resultant aerodynamic force and moment.

To summarize the basic ideas, a panel method uses the fact that sources and doublets are solutions to the Prandtl-Glauert equation. The numerical procedure is as follows:

1. Break the aircraft surface into an assemblage of panels
2. Use the panels to create source-doublet distributions in terms of singularity parameters $\{\lambda\}$, whose values are to be determined
3. Form influence-coefficient expressions for the potential or velocity or both at each of N panel control points owing to the source-doublet distribution of any panel; for supersonic flow the zones of silence must be accounted for
4. Use the influence-coefficient expressions to enforce boundary conditions at N points, giving the $N \times N$ system of equations

$$[\text{AIC}]\{\lambda\} = \{b\}$$

5. Solve for the singularity parameters $\{\lambda\}$, then compute the potential and velocity at any point of interest

6. Knowing the velocity, compute the panel pressure distributions

7. Integrate the pressure distributions to obtain forces and moments

The above process, in one form or another, is common to all panel methods. Selecting a way to break the surface S into panels Σ , choosing and implementing functional forms for σ and μ , and evaluating the influence-coefficient surface integrals are the fundamental tasks.

In section 4 we discuss how various codes differ in the selection of Σ , and of $\sigma(\xi, \eta)$ and $\mu(\xi, \eta)$. Section 5 describes various means of specifying boundary conditions and other aspects of modeling physical problems. Appendix A gives additional details about how the basic approach described above is actually implemented into the PAN AIR code. This will lead to specific surface integrals that must be evaluated to obtain the influence-coefficients. The analytic evaluation of some of these integrals for subsonic flow is given in appendix B.

The reader is warned that the above description has ignored some subtle points that will be addressed later. Specifically, a panel with both source and doublet distributions requires two boundary conditions per panel. These boundary conditions generally require some statement about the flow on each side of the panel. (There is an exception in supersonic flow.) The boundary conditions must also produce a well-posed mathematical problem, that is, one with a unique solution; otherwise the AIC matrix will be singular. Also, some of the analytic expressions for the potential and velocity can become singular (blow up) when the influenced point is a point of the influencing panel (when $i = j$); hence use of the name source-doublet "singularities." Boundary conditions will be discussed in section 5, and improper integrals (those having a nonintegrable singularity) will be discussed in appendix C.

4. DISTINCTIONS BETWEEN PANEL CODES

Having outlined the basic approach used by panel methods, let us now look at various implementations. Different ways of approximating the actual aircraft surface with surface panels will be described first, followed by the selection of singularity distributions and their functional forms. Finally, a summary of several specific panel codes will be presented.

Surface Geometry

Current actual-surface panel codes generally allow the user to break the configuration into logical pieces such as forebody, canopy, and the wing upper and lower surfaces. In the PAN AIR code, such logical pieces are called networks of panels (fig. 8). A component such as a wing can also be broken into several networks. For example, two different models for the F-16XL wing upper surface are shown in figure 9. The 3-network model is appropriate if control-surface deflections are not of interest; the 10-network model allows leading and trailing-edge control surface deflections to be made.

Panel codes typically use arrays of $M \times N$ surface grid points to define the corner points of panels, as illustrated in figure 10. Since the four panel corner points are not, in general, coplanar, a single flat panel cannot be used to connect the four corner points.

The lower-order (constant-strength) codes usually use some kind of flat "average" panel defined by the four corner points. Using flat quadrilateral panels to represent a curved surface causes gaps to exist between the edges of adjacent panels (fig. 11, courtesy of John Hess). This approach begs the natural question about "leaks" through the gaps. Actually, for constant-strength panels, the panels themselves leak rather badly everywhere except at the control points x , where the discrete boundary conditions are imposed. The constant-strength, singularity influence-coefficient-computed velocities at any points on the panel other than the control point are not generally reliable. Surface and near-surface values of velocity away from the control points are usually obtained by interpolation.

Parabolically curved panels have been used in at least three higher-order, subsonic-flow codes (refs. 31-33). For a given number of panels on a curved surface, such panels generally provide better accuracy than do flat panels. The parabolically curved panels are similar to the flat panels in that they still leave gaps between adjacent panels.

As indicated in the introduction, the difficulties encountered with extending panel methods to supersonic flow were eventually traced to using doublet-strength distributions that were not continuous at panel edges. The task of building continuous doublet-strength distributions requires that the panel edges themselves be contiguous (have no gaps) since the doublet strengths are referenced to the panel geometry.

There are several ways to connect an $M \times N$ array of arbitrary points with $(M - 1) \times (N - 1)$ quadrilateral panels that have no gaps along adjacent panel edges. Probably

the simplest is to use several piecewise flat subpanels to connect four corner points. The most recent version of the QUADPAN code uses four triangular subpanels (fig. 12(a)), whereas the PAN AIR, HISSS, AND MCAERO codes use four triangular subpanels and a flat interior parallelogram (fig. 12(b)). Although not shown in figure 12(b), the flat parallelogram portion of the panel is further subdivided into four more triangular panels defined by the diagonals of the parallelogram. This is done to facilitate the construction of the continuous quadratic doublet-singularity distributions within the panel.

Two codes, SOUSSA and the most recent version of the LEV code (leading-edge vortex code, also called the free vortex sheet code, ref. 27), use hyperbolic-paraboloid panels, (fig. 12(c)). The curved shape of these panels is the same as for a structural plate that is loaded as in figure 12(d), that is, a twisted shape is produced (ref. 34). The side edges remain straight and hence produce no gaps.

Use of the contiguous piecewise flat panels has enabled the influence-coefficient-equation surface integrals (eqs. (9) and (11)) to be evaluated analytically for both subsonic and supersonic free-stream flow. Use of the hyperbolic-paraboloid panels has been restricted to subsonic flow (no one has been able to evaluate the surface integrals when using these panels for supersonic flow).

Singularity Distributions

Most codes use a combination of source and doublet distributions on the panels. The primary exceptions are the Woodward-Carmichael and USSAERO (also called Woodward-2) codes, which use elementary horseshoe vortices instead of doublets. The elementary horseshoe vortex potential is obtained by integrating the doublet potential in the x (streamwise) direction (ref. 35, p. 87). The strength of the vortex distribution, also called the surface vorticity vector $\vec{\gamma}$, is related to the doublet strength as follows (ref. 2, eq. (A-3); ref. 11, eq. (B.3.9)).

$$\vec{\gamma}(\xi, \eta) = \hat{n} \otimes \vec{\nabla} \mu(\xi, \eta) \quad (18)$$

Both $\vec{\gamma}$ and $\vec{\nabla} \mu$ are in the plane of the panel, \hat{n} is a unit vector normal to the panel, and \otimes is the cross-product operator.

Source, doublet, and vorticity surface distributions cause certain flow properties to be discontinuous with respect to the panel surface; that is, there is a jump in the flow properties. In general, this means that the velocity

vectors on opposite sides of a panel are different. This is illustrated in figure 13, where the subscripts U and L refer to the "upper" and "lower" sides of the panel, respectively. For incompressible flow, a source-only panel causes the normal component of the velocity at point (ξ, η) of the panel to jump by an amount given by

$$(\vec{V}_U - \vec{V}_L) \cdot \hat{n} = \sigma(\xi, \eta) \quad (19)$$

and a doublet-only panel causes both the potential and the tangential component of velocity to jump. These jumps are given by

$$\phi_U - \phi_L = \mu(\xi, \eta) \quad (20)$$

$$\vec{V}_{TU} - \vec{V}_{TL} = \vec{\nabla} \mu(\xi, \eta) \quad (21)$$

The jump property given by equation (21) is derived in appendix B. Each of the jump properties is derived in reference 33.

The velocity jump across a panel for incompressible flow is then given by

$$\vec{V}_U - \vec{V}_L = \sigma \hat{n} + \vec{\nabla} \mu \quad (22)$$

The generalization of equation (22) for compressible flow is given by equation B.3.29 of reference 12 (version 3.0, 1990).

Equations (18) and (22) provide some guidance for selecting consistent functional forms for the singularity distributions. A constant-strength source panel combined with a constant-strength vorticity panel or a linear-strength doublet panel will produce a velocity-jump distribution that is constant over the panel surface. A linear velocity-jump distribution requires a linear-source and linear-vorticity or quadratic-doublet distribution. As will be discussed later, popular sets of boundary conditions are those that include setting the perturbation potential to zero on the interior side of panels (the side not wetted by the external flow field). Consequently there is no interior perturbation velocity, and the velocity jump across the panel equals the perturbation velocity on the exterior side.

As discussed in reference 32, consistency also depends on the surface shape used for the panels. Flat panels are consistent with constant sources, and parabolic panels are consistent with linear sources. In this sense, the methods of references 32 and 33 (which use parabolic panels, linear sources, and linear vorticity or quadratic

doublets) are among the few totally consistent higher-order formulations.

Continuity of Doublet Strength

The reason discontinuous doublet strength can cause disastrous numerical problems in supersonic flow is illustrated in figure 14. For a problem simple enough to solve in closed form, the actual doublet strength might look something like that in the top part of the figure, that is, μ varies in a continuous manner. A panel method that does not enforce doublet-strength continuity at panel edges will produce a solution like that shown in the lower part of the figure, that is, the doublet strength jumps at the panel edge. Now consider either of the panels separately. In this view the doublet strength has a nonzero value at the panel edge. The velocity field produced by the doublet distribution on either panel is given by the second term of equation (11). This term can be integrated by parts (appendix B of ref. 11) to obtain

$$\begin{aligned} \vec{v}_P = & \frac{1}{K} \iint_S \vec{\gamma} \otimes (\vec{\nabla}_P R^{-1}) d\xi d\eta \\ & + \frac{1}{K} \int_{\ell} \mu(\ell) \vec{\nabla}_P (R^{-1}) \otimes d\vec{\ell} \end{aligned} \quad (23)$$

where the line integral is around the panel perimeter.

The surface integral in equation (23) involves the surface vorticity vector $\vec{\gamma}$, and is called the regular part of the doublet velocity. The line integral involves the doublet strength at the panel edges and is called the line-vortex term. The two line-vortex terms from the common edges of the two panels in figure 14 produce a single line-vortex of strength $\Gamma(\ell) = \Delta\mu(\ell)$, where $\Delta\mu(\ell)$ is the jump in the doublet strength along the panel edge. The velocity field from this line vortex is spurious since the actual doublet strength does not jump at the panel edge; that is, the discretization has introduced velocities that should not exist.

In subsonic flow these spurious velocities decay rapidly with distance from the edge and usually do not cause serious problems. In supersonic flow, these velocities persist, their effect propagating down the Mach cones. Consequently, erroneous incremental flows continue to exist at control points within the domain of influence of the disturbance points, thereby introducing errors in the AIC matrix. These errors are frequently serious enough to produce a totally incorrect solution for the flow.

Now, if it were known in advance that the discretized doublet strength would always be continuous in value,

then the resultant line-vortex term along common panel edges of adjacent panels would always be zero. Hence, the line-vortex term in equation (23) would not even have to be computed, but could be simply discarded. This approach is taken in the subsonic-supersonic-flow PAN AIR and HISSS codes: the doublet strengths are made continuous by construction and the line-vortex terms are thrown away.

A comparison of results for a 3%-thick swept wing at $M_\infty = 2.05$, based on discontinuous and continuous quadratic-doublet distributions, is shown in figure 15 (figs. 9 and 10 in ref. 36; figs. 48 and 62 in ref. 37). In the discontinuous-distribution case, there is a pressure spike at about 80% chord of the station just inboard of the tip. This is caused by a doublet-strength discontinuity near the leading-edge region of the wing tip, the effect of which propagates down the Mach cone originating at the tip leading edge. The spike is not present in the continuous doublet-distribution case.

Summary of Methods

Table 1 summarizes the basic features of several panel codes. Codes that handle only subsonic flow are listed separately from those that treat both the subsonic and supersonic cases. The QUADPAN code is listed twice because it was originally a subsonic-only code and was later revised to do supersonic flow. The year given next to each code's name is the approximate year the code was introduced. The panel geometry and the singularity types and their spatial distributions are listed for each code. A footnote indicates that geometry or singularity type is continuous from panel to panel. The table includes what are probably the best known, or most generally available codes; other codes (often proprietary) also exist. References 39 through 41, as well as other sources (material distributed at the 1985 AIAA Workshop on Aerodynamic Analysis Using Panel Methods), compare results from several of the codes for various configurations.

Codes for subsonic-only flow— The lower-order Hess code (also known as the Douglas-Neumann code) is considered by many to be the first practical implementation of the panel method for quite general geometry (ref. 2). It actually exists in several versions, the first being a source-only version that did not treat lifting problems. The lifting case was later added. The Hess family of codes is one of the few that enforce the Kutta condition with a nonlinear pressure rule. As shown in reference 40 this can sometimes give a better trailing-edge pressure result than is possible with a linear approximation to the pressure rule.

MCAERO uses higher-order continuous doublet distributions on piecewise flat continuous panels (ref. 17). One of its important capabilities is the use of analytically differentiated (with respect to panel coordinates) influence-coefficients. These are used to efficiently implement the so-called design problem, that is, the problem of determining the geometric shape required to produce a specified pressure distribution.

SOUSSA stands for steady, oscillatory, and unsteady subsonic and supersonic aerodynamics (ref. 8). Although it produced some supersonic results by using a small but nonzero reduced frequency, it turned out to be incapable of doing steady supersonic flow. One of its legacies was to popularize the so-called Morino boundary-condition formulation, which is discussed in section 5. This formulation led to renewed interest in lower-order subsonic codes and resulted in the development of the VSAERO and QUADPAN codes.

VSAERO (from vortex separation aerodynamics analysis) is one of the few codes that contain a procedure for calculating the shape and location of the trailing-wake system (ref. 18).

The LEV code (leading-edge vortex; ref. 27) is also known as the free-vortex sheet code. It was designed specifically to model the vorticity shed from sharp leading edges of swept wings (fig. 5).

The higher-order Hess code (ref. 32) is the most recent version of the Hess family of codes. It uses parabolically curved panels in conjunction with linear source and linear vorticity (quadratic doublet) distributions.

Codes for subsonic or supersonic flow— The Woodward-Carmichael code (refs. 4, 5) (also known as the constant-pressure panel code and the Woodward-I code) was described in the introduction. It is still used for simple configurations that can be approximated with the mean-surface representation of figure 1(b).

USSAERO (unified subsonic/supersonic aerodynamics) is also known as the Woodward-II code (ref. 7). It differs from the Woodward-I code in that the line distributions used for bodies were changed to constant-strength source panels, and the constant-strength vorticity panels were changed to distributions wherein the strength varies linearly in the chordwise direction and is constant in the spanwise direction. The corresponding doublet strength (quadratic-linear) is not continuous, so flat mean-surface models of lifting surfaces are usually required for supersonic flow.

PAN AIR (panel aerodynamics) is generally considered to be the first actual-surface paneling code with reliable numerics for supersonic flow (refs. 9-14). In addition to using continuous doublet distributions, it was also necessary to incorporate forward-weighted splines for the supersonic case. This is somewhat analogous to the use of forward-differencing in the finite-difference computational fluid dynamics (CFD) codes. The basic technology in PAN AIR is also used in the HISSS code (higher-order subsonic/supersonic singularity method, refs. 16 and 42).

QUADPAN (quadrilateral panel aerodynamics program) started out as a subsonic-only code and used constant-strength sources and doublets (ref. 19). Later, the doublets were changed to a linear-continuous distribution so that supersonic flow could be handled (from 1985 AIAA Workshop on Aerodynamic Analysis Using Panel Methods).

It has been well established that continuous doublet distributions are essential for reliable numerics in supersonic flow. However, it is probably fair to say that there is not a unanimous agreement between panel code developers about the need for higher-order approaches for the subsonic-flow codes. The advantages that lower-order codes offer over higher-order codes are (1) less work to derive the influence-coefficient equations; (2) simpler coding implementation (because the higher-order approaches must relate information involving different panels, which leads to special cases and logic); and (3) far fewer arithmetic operations, hence lower run costs. One reason some subsonic-only codes use higher-order approaches is that their developers believe the numerics are more reliable than those of the lower-order approaches for highly complex geometry. In the case of two codes that use parabolic panels with linear sources and quadratic doublets, numerical calculations have demonstrated that fewer panels are required than for lower-order methods to obtain a given accuracy (refs. 32, 33). This seems to be especially true for internal flows.

5. MODELING

Modeling refers to particular techniques used to simulate flow about an object. The modeling tools at the disposal of a panel-method user are (1) the geometric generality that panel codes provide, (2) the use of sources and doublets, individually or in combination, and (3) boundary conditions. In this section we will discuss boundary conditions, their interplay with the source-doublet jump properties introduced in section 4, and how the combination can be used to model in different ways. There is also a brief look at wake modeling.

In section 2 we discussed the general limitations inherent in the Prandtl-Glauert equation derivation, namely, the flow is represented as being inviscid, irrotational (potential), and linear. If the free-stream Mach number is supersonic, there are additional geometric restrictions; these are illustrated in figure 16.

In supersonic flow, the Prandtl-Glauert equation admits solutions for solid surfaces only if the surfaces are swept back more sharply than the Mach cone. Thus, the higher the Mach number, the more streamlined must be the aircraft. This restriction means that forebodies must be pointed, not blunt. Wing leading edges can be blunt only if they are swept behind the Mach cone (a so-called subsonic leading edge).

Surfaces can be swept at angles smaller than the Mach cone only if they do not represent solid surfaces. These so-called superinclined panels (ref. 11) are used for nacelle inlet faces and nozzle exit planes. Superinclined panels use both sources and doublets, and both boundary conditions must be prescribed on the downstream side of the panel. Numerical experiments indicate that these downstream boundary conditions must also be of a specific type, namely, that the potential and its normal derivative must be specified. This is analogous to an initial value problem. Superinclined panels have no upstream influence. The panels generate a downstream flow only and simply absorb any flows that run into them. Reference 11, appendixes A and B in reference 12, and reference 37 are recommended sources of information on the supersonic aspects of modeling.

Mass-Flux and Velocity Boundary Conditions

The physical description of a real flow at a surface is given by the no-slip boundary condition

$$\vec{V} = 0 \quad (24a)$$

or

$$(\rho \vec{V}) = 0 \quad (24b)$$

These equations state that the total velocity vector \vec{V} , or the mass flux vector $(\rho \vec{V})$, is zero at a solid surface. For inviscid flow, the tangential component of the velocity cannot be prescribed (unless the pressure is known) and equations (24) are replaced with the zero normal-flow boundary conditions,

$$\vec{V} \cdot \hat{n} = 0 \quad (25a)$$

or

$$(\rho \bar{\mathbf{V}}) \cdot \hat{\mathbf{n}} = 0 \quad (25b)$$

which must be supplemented with a Kutta condition for subsonic trailing edges.

Equation (25b) is nonlinear since the density is a function of the unknown velocity; a linear approximation to equation (25b) is (from sec. 1.11 of ref. 30)

$$\rho \bar{\mathbf{V}} \doteq \rho_\infty \bar{\mathbf{V}}_\infty + \rho_\infty \bar{\mathbf{V}}\phi \quad (26)$$

Equation (26) involves neglecting terms that are of the same order of magnitude as those neglected in deriving the Prandtl-Glauert equation. Dividing by ρ_∞ gives

$$\bar{\mathbf{W}} \equiv \frac{\rho}{\rho_\infty} \bar{\mathbf{V}} \doteq \bar{\mathbf{V}}_\infty + \bar{\mathbf{w}} \quad (27a)$$

where, from equation (8)

$$\bar{\mathbf{w}} = \bar{\mathbf{V}}\phi = (\beta^2 \phi_x, \phi_y, \phi_z) \quad (27b)$$

The quantities $\bar{\mathbf{W}}$ and $\bar{\mathbf{w}}$ are called the linearized total and perturbation mass flux, respectively. Thus, equation (25b) is approximated by the mass-flux boundary condition

$$\bar{\mathbf{W}} \cdot \hat{\mathbf{n}} = 0 \quad (28)$$

which is linear in the components of the perturbation velocity, and depends on the free-stream Mach number. If the panel is not meant to be impermeable, for example, at an inlet face, then the right-hand side of equation (28) is replaced with a specified nonzero value.

For a fixed subsonic Mach number, a solution for $\phi(x,y,z)$ can be obtained in either of two ways. The first is to solve the "true" compressible problem, that is, solve the Prandtl-Glauert equation as it stands, using the mass-flux boundary condition applied to the true geometry. The second (and better known) way is to solve the equivalent incompressible problem by using the Prandtl-Glauert transformation to convert equation (1) to Laplace's equation (sec. 7-1 in ref. 35):

$$\phi'_{xx'} + \phi'_{yy'} + \phi'_{zz'} = 0 \quad (29)$$

using the velocity boundary condition

$$\bar{\mathbf{V}}' \cdot \hat{\mathbf{n}}' = 0 \quad (30)$$

applied to the transformed geometry. In equations (29) and (30) the primes indicate that all the variables are in the transformed coordinates, for example, $\bar{\mathbf{V}}' = \bar{\mathbf{V}}'_\infty + (\phi'_{x'}, \phi'_{y'}, \phi'_{z'})$. Transforming the solution for ϕ' back to the true (physical) variables gives the solution for ϕ for the true geometry. The important point is that the solution for ϕ obtained from the first approach will be the same as that obtained from the second approach (ref. 43). Thus, solving for the flow about the true geometry by using the subsonic Prandtl-Glauert equation with mass flux (instead of velocity) boundary conditions, is mathematically the same as solving the equivalent incompressible problem with velocity boundary conditions applied to the transformed geometry. The first approach has the advantage that it can also be used for supersonic flow (where there is no equivalent incompressible problem).

Note that the linearized mass flux defined by equations (27) is not parallel to the true mass flux $\rho \bar{\mathbf{V}}$, and, hence, is not parallel to the velocity vector $\bar{\mathbf{V}} = \bar{\mathbf{V}}_\infty + \bar{\mathbf{v}}$. This inconsistency is one of the prices paid for the linearization. The consequences of this will be illustrated with the following two examples. (Theoretical discussions of mass-flux and velocity boundary conditions appear in refs. 44-46.)

The first example demonstrates the accuracy of the mass-flow boundary condition and the Prandtl-Glauert equation for supersonic flow over a thin wedge. It also demonstrates the jump properties of the mass-flux and velocity vectors across shocks predicted with the Prandtl-Glauert equation.

Panel-method results obtained from the PAN AIR code are shown in figure 17 (from ref. 9). The boundary condition applied to the exterior side of the panels is the linearized mass flux condition $\bar{\mathbf{W}} \cdot \hat{\mathbf{n}} = 0$. This forces the linearized mass flux vector $\bar{\mathbf{W}}$, instead of the resultant velocity vector $\bar{\mathbf{V}}$, to be parallel to the wedge faces. Pressures have been computed with the isentropic and the second-order pressure rules (eqs. (8.10) and (8.11), respectively, in ref. 23). Also shown are the pressure distributions computed from shock-expansion theory and from classic linear thin-airfoil theory (secs. 4.16 and 4.17, respectively, in ref. 23). The PAN AIR results are very close to those of nonlinear shock-expansion theory, having a greater pressure magnitude on the frontward-facing compression surface than on the rearward-facing expansion surface. This contrasts with the classic linear thin-airfoil theory, which predicts equal and opposite pressures on the two inclined faces.

How does one explain that PAN AIR, which solves the linear Prandtl-Glauert equation, produces results that agree more closely with nonlinear shock-expansion theory than with classic linear thin-airfoil theory? Apparently, for this particular problem, the velocities are small enough to make negligible the nonlinear terms in the differential equation. This conclusion is justified by the close agreement between the isentropic and second-order pressure rules. (It is good practice to always compute the pressures by these two rules; a substantial disagreement in the results is a sure sign that the small-perturbation assumptions of the Prandtl-Glauert equation are being violated.) Since classic thin-airfoil theory is also based on the Prandtl-Glauert equation, but in addition depends on complete linearization of the boundary conditions, the explanation must reside in the boundary conditions. Although PAN AIR uses the linearized mass-flow \vec{W} in the boundary condition $\vec{W} \cdot \hat{n} = 0$, the unit normals \hat{n} act at the actual wedge surfaces. In the classic linear-theory solution the boundary conditions are not applied to the true geometry. Instead, the boundary conditions are applied along the straight upper side of the wedge, and the flow is made to turn through the wedge angles, as in the mean-surface modeling of the Woodward-Carmichael code (see sec. 1). So, this appears to be an example of an instance in which the solution is more affected by approximations made to the boundary conditions than it is by those made to the differential equation.

The mass-flux and velocity vectors at two points on opposite sides of the Mach line emanating from the wedge apex are shown in figure 18. We first note that for expansive flow about a corner, such as at the wedge apex, the Prandtl-Mayer solution predicts an expansion fan. That is, away from the apex the flow properties change gradually through the fan. However, the Prandtl-Glauert equation predicts abrupt changes that occur along the apex Mach line. This "expansion shock" approximation to an expansion fan is a poor representation at large distances from the apex, but is accurate near the apex. Our point here is to illustrate what happens to a panel-method solution across such a shock (whether expansive or compressive). Both the mass-flux and velocity vectors are discontinuous across the Mach line; they jump in both magnitude and direction. For the mass flux, the tangential component jumps, and the normal component is continuous. For the velocity, the tangential component is continuous, and the normal component jumps. This is the same behavior as predicted by the nonlinear Rankine-Hugoniot relations, thus providing some measure of confidence in the linearized mass-flux approach.

The second example (fig. 19) shows the pressure at any point on 10° and 15° half-angle cones at zero angle of

attack, for free-stream Mach numbers between 1.0 and 4.0 (fig. 4.1 in ref. 15). At the lower Mach numbers, the mass-flux-boundary-condition solution agrees more closely with the exact Euler-equation solution than does the velocity-boundary-condition solution. As the Mach number increases, the mass-flux and velocity-boundary-condition solutions become less accurate. The mass-flux-boundary-condition solution rapidly diverges from the exact solution, and crosses the less rapidly diverging velocity-boundary-condition solution. As the cone angle increases, the Mach number at which the mass-flux and velocity-boundary-condition solutions cross one another becomes smaller. This supersonic "thick-body" behavior is responsible for the fact that when panel methods are applied to nonslender fighter forebodies, the velocity-boundary condition often gives superior answers to the mass-flux boundary condition in the region just ahead of the canopy (refs. 47, 48). For such cases, the mass-flux boundary condition can actually produce negative pressure coefficients, as suggested by the 15° cone solution behavior of figure 19. For bodies that are adequately slender, the linear Prandtl-Glauert equation with mass-flux boundary conditions can provide good answers, for example, the Mach 1.6 pressures on the B-1 forebody presented in references 36 and 37. The important conclusion to be drawn from figure 19, and from other examples in ref. 15, is that inviscid supersonic flow solutions based on the Prandtl-Glauert equation can be substantially in error if the Mach number, thickness, or angle of attack are too large. In such cases, codes based on nonlinear theories (for example, the full-potential equation or Euler equations) must be used for reliable answers.

Interior Potential

An actual-surface panel model of an aircraft generally produces a set of panels that separates space into two or more distinct regions: enclosed interior volumes and an external volume extending from infinity to the external side of the panels. The flow in the external volume corresponds to the physical flow field being modeled. The flow in the interior volumes is fictitious but, as will be shown, can be used to advantage.

Newcomers to panel methods often find the idea of an internal flow field to be strange in that no such flow exists inside a real wing. However, it must be remembered that we are using sources, doublets, and boundary conditions to create the flow fields, and flow will exist on either side of the source-doublet panels. The external-internal flow fields are in general independent of one another; they depend on the boundary conditions on the external-internal sides of the panels. These include direct boundary conditions explicitly imposed on each side of

the panel and indirect boundary conditions resulting from some specification of the source or doublet strength. The indirect boundary conditions arise because of the jump in flow properties produced by sources and doublets.

The boundary condition implied by the equation (20) jump property is the cause of a common mistake made by new users of panel methods, namely, not specifying the potential at a point of an interior volume. When an interior volume is totally enclosed by panels that all have doublet distributions, the potential must be specified at one or more interior points, and this must be done with a source distribution. If this is not done, the problem is ill-posed, that is, it does not have a unique solution, and the AIC matrix will theoretically be singular (will not possess an inverse). (In practice, numerical round-off error often changes a theoretically singular matrix to just an ill-conditioned matrix.)

The reason for the problem being ill-posed is generally explained as follows. At $\bar{x} = \infty$ the value of the potential owing to a source or doublet is zero (this is called the far-field boundary condition). At the exterior side of panels enclosing an interior volume the potential will have some distribution $\phi_{\text{ext}}(x,y,z)$ that depends on the surface boundary conditions and on the resulting source-doublet strength distribution. On the interior side of the panels, the potential is $\phi_{\text{int}}(x,y,z)$, which by equation (20), differs from the external distribution by an amount equal to the doublet-strength distribution $\mu(\xi,\eta)$. Now, if at some interior point, a constant c , arbitrary except that it must satisfy any boundary condition associated with the point, were to be added to $\phi_{\text{int}}(x,y,z)$, then $\phi_{\text{int}}(x,y,z) + c$ would also satisfy the Prandtl-Glauert equation and, hence, be another solution. The way to make the interior solution unique is to specify a value for the potential at an interior point, thus determining the constant c . (The same argument can be made for the exterior side of the panels, which requires that the arbitrary constant be zero to satisfy the far-field boundary condition $\phi_{\infty} = 0$. Thus, no explicit specification of the potential at an exterior point has to be made.)

The interior potential at a point must be specified with a source panel, and not a doublet panel, because of the "physically" different behavior between sources (or sinks) and doublets. With any paneled geometry, the boundary conditions are enforced only at the control points. Hence, when a finite number of control points is used to impose boundary conditions there will be some degree of "leakage." That is, the integral of the source strength (jump in normal component of mass flux) over the surface enclosing the interior volume will not be exactly zero. When a source panel is used to specify velocity potential in the interior domain, the panel is

capable of generating or consuming fluid to conserve mass that is leaked out of or into the interior domain. (The source strength is one of the unknowns that are solved for.) The doublet panel does not have the ability to generate or swallow fluid (at least, in a net sense), and consequently is not capable of handling the leaked flow. Numerical examples demonstrating this behavior are given in cases 5 and 6 of reference 49 (pp. 6-7).

Another interesting example in reference 49 is case 7. Here, a thick wing is modeled using doublets-only for the wing upper and lower surfaces and sources-only for the panels closing off the wing-tip opening. Using only a single type of distribution on all panels allows only one boundary condition per panel, which was chosen to be $\vec{W} \cdot \hat{n} = 0$ on the exterior panel sides. The interior potential was not specified anywhere inside the wing. At first glance this also appears to be an ill-posed problem, but it is not. The source-only tip-closure panels do not produce a potential jump. Therefore, as far as the potential is concerned, this model behaves as if there were no tip closure, and in this sense the wing interior is not a separate domain from the exterior domain. Hence, the constant $\phi_{\infty} = 0$ applies to both the exterior and interior part of the single domain. The zero-normal-flow boundary condition applied at the tip, however, does separate the flow into two regions.

In actual practice, the interior potential is set not at just a single point, but at the interior-side control point locations of all panels. If the boundary condition $\phi_{\text{int}}(x,y,z) = 0$ is used at all such control points there will be no internal perturbation flow (assuming an adequate number of panels), giving uniform free-stream flow in the interior volume. If both sources and doublets are used with each panel, then another boundary condition is needed, and it is selected to control the flow on the exterior sides of the panels. Two alternative ways of doing this, for flow about a solid (impermeable) aircraft surface, are described next. The first is a direct approach, the second is an indirect one.

The direct approach is illustrated in figure 20(a). On the exterior panel side, the zero normal mass flux boundary condition (eq. (28)) is imposed. The resulting boundary condition pair at each panel control point is

$$(\vec{W} \cdot \hat{n})_{\text{ext}} = 0 \quad (31a)$$

$$\phi_{\text{int}} = 0 \quad (31b)$$

The indirect approach (sometimes referred to as the Morino formulation) is illustrated in figure 20(b). Here, equation (31a) is replaced by a condition imposed on the source strength, and the boundary condition pair is

$$\sigma = -\tilde{V}_\infty \cdot \hat{n} \quad (32a)$$

$$\phi_{\text{int}} = 0 \quad (32b)$$

The equivalence between these two boundary condition pairs can be shown by starting with the definition of the source strength (see eq. (8)):

$$\sigma = (\tilde{w}_{\text{ext}} - \tilde{w}_{\text{int}}) \cdot \hat{n} \quad (33)$$

If the perturbation potential is zero everywhere in the interior region, then its derivative is zero in every direction and \tilde{w}_{int} is then zero. (Equation (32b), applied to the interior side of every panel normally produces a good approximation to this condition.) Then equation (33) becomes (using the definition for \tilde{W} given by eq. (27a))

$$\begin{aligned} \sigma &= \tilde{w}_U \cdot \hat{n} \\ &= (\tilde{W}_U - \tilde{V}_\infty) \cdot \hat{n} \\ &= \tilde{W}_U \cdot \hat{n} - \tilde{V}_\infty \cdot \hat{n} \end{aligned} \quad (34)$$

Now imposing the $\tilde{W}_U \cdot \hat{n} = 0$ condition sought (eq. (31a)), we get equation (32a).

The indirect approach has two features that reduce run cost. First, only the influence-coefficients for the potential, and not the three components of velocity, have to be computed. Second, since the source strengths are specified, only the doublet strengths have to be solved for, cutting the size of the [AIC] matrix roughly in half. (The reason the size is not necessarily cut exactly in half is that some codes use more doublet unknowns than source unknowns, e.g., for wakes, and for doublet matching in the continuous-doublet codes.)

The direct approach requires that both potential and velocity influence-coefficients be computed, and both source and doublet strength must be solved for. For a given number of panels this causes the direct approach to be more costly than the indirect approach. The advantage of the direct approach is that it is sometimes more accurate than the indirect approach. This is apparently because the indirect approach depends on the internal perturbation potential being zero everywhere for equations (32) to accurately represent equations (31). In practice, the poten-

tial is set to zero only at discrete interior points; consequently, the indirect formulation sometimes produces more error than does the direct approach.

An additional advantage, common to both formulations, is the property that the internal flow is everywhere uniform (it equals the free-stream velocity). For supersonic free-stream Mach numbers this prevents the formation of internal disturbances that otherwise would propagate along Mach lines and reflect from the internal sides of the panels. If not eliminated, these reflections can cause severe internal flow disturbances that are "felt through the panels" and degrade the external flow-field solution. Although there are no Mach-line disturbances in subsonic flow, large velocities are normally produced by the line-vortex behavior of constant-strength doublet panels. These large velocities are eliminated in the internal flow region by the internal potential being set to zero. This is apparently why solutions obtained with the newer constant-strength source-doublet formulations are not as sensitive to the panel layout as were earlier constant-strength codes (which did not use a zero interior-perturbation potential).

A final example uses doublet-only panels to represent a wing, including the tip closure. Since the interior volume is totally enclosed with doublet panels, the potential must be set in the interior volume for the problem to be well-posed. Also, having only one type of singularity distribution means that only one boundary condition can be employed per control point. The direct approach would be to set the interior potential with an additional source panel located inside the wing, and specify $\tilde{W} \cdot \hat{n} = 0$ on the exterior. A clever indirect approach is to simply set the total (instead of the perturbation) potential to zero on the interior side of each panel. For sufficiently dense paneling, this will make the total potential close to uniformly zero at all interior points. Hence the gradient of the total potential in any direction, which is the total (linearized) mass-flux in that direction, will also be zero. Consequently, the total mass-flux component normal to the interior side of the panels will be zero. Then, since doublets do not produce a jump in normal mass flux, the normal mass flux on the exterior sides of the panels will also be zero, that is, $\tilde{W} \cdot \hat{n} = 0$ on the exterior is produced.

Wakes

Wake panels are used to enforce the Kutta condition at sharp (usually the trailing) edges of lifting surfaces. Since wakes trail downstream from these edges, they also influence the flow experienced by downstream components. For example, the load experienced by a wing will

depend on the proximity of the wake from an upstream canard.

Figure 21 shows a PAN AIR model of a supersonic fighter wing-canard concept (ref. 50). Two of three wake models tried for this configuration are shown in figure 22. Simple, flat wakes for both the wing and canard are used in the first model, the wakes being positioned approximately in the wing-canard mean plane (fig. 22(a)). For each angle of attack, the resulting span loadings were then used by a multiple lifting-surface code to compute the approximate rolled-up shape of the canard wake. The rolled-up canard wakes were used for the second model (fig. 22(b)). The third model (not shown) again used flat wakes, but for each angle of attack the canard wake was aligned with the free-stream velocity direction. The results in reference 50 indicate that for this configuration, the second and third models give essentially the same lift and moment, and these agree more closely with wind-tunnel results than do the results from the first wake model. Lift and pitching moment coefficients at Mach 2.2, obtained from the third wake model, are shown in figure 23. There is a noticeable difference in the PAN AIR-predicted lift-curve slopes for the isentropic and second-order pressure rules, indicating that nonlinear effects are beginning to become important. Also shown are results from the USSAERO (version B) program; it does less well at predicting the moment.

Another wing-canard configuration is shown in figure 24 (ref. 51). The effect of aligning a flat-canard wake model with the free stream instead of with the chord plane (unaligned position of fig. 25) for this close-coupled wing-canard is illustrated in figure 26. This figure shows the spanwise circulation distribution of the canard and the wing for the aligned and unaligned flat-canard wakes. The canard-wake position does not significantly affect the lift distribution along the canard. It does, however, have an important effect on the wing-lift distribution. Moving the canard wake from the unaligned position to the aligned position causes two major changes in the flow over the wing, the dominant one of which is an increase in wing lift inboard of the canard-tip station. This is due to the diminished canard-wake downwash field, raising the effective angle of attack of the inboard wing section. The secondary effect is a loss in wing lift outboard of the canard-tip station. This loss in lift is due to diminished spanwise velocity imparted on the upper surface of the wing by the canard wake, which is due to the increased distance between the canard wake and the wing. The net effect of these changes caused by the aligned wake model is an increase in total lift over that predicted by the unaligned wake model.

The final example, taken from reference 52, is a PAN AIR flaps-down analysis of the Boeing 737-300 (fig. 27). The actual and computational flap geometries for the flaps-15 setting, used for most takeoffs, are shown in figure 28(a). The assumed flap, wing, and slat wake positions are shown in figure 28(b). Leading- and trailing-edge spanwise geometry discontinuities owing to the deflected flaps and slats also had to be treated; these are discussed in reference 52.

The drag buildup was obtained from a combination of methods. The profile drag for everything but the wing was estimated from handbook data. The wing profile drag was estimated from a two-dimensional multielement-airfoil panel code coupled with a viscous model (ref. 53). The induced drag was obtained from PAN AIR's surface-pressure integrations. Figure 29(a) shows the drag contributions for both the flaps-15 (F15) setting, and a lower setting called flaps-1 (F1). The resulting computational lift-to-drag ratios are compared with flight data in figure 29(b).

6. TRANSONIC FLOW

Panel-method codes have existed for about 25 years and are still the only codes routinely used to analyze flow about complex three-dimensional configurations. Their general inability to solve nonlinear problems is a serious drawback, however, and most current CFD research involves finite-difference, finite-volume, or finite-element approaches to solving nonlinear flow equations. In the United States, the finite-difference and finite-volume approaches currently seem to be in most favor. Unfortunately, most finite-difference and finite-volume approaches require well-structured flow-field grids that conform to the surface of an aircraft. It "is the difficulty in generating 'suitable grids'" (ref. 54) that is the major technical obstacle to routinely computing inviscid transonic flow about realistic aircraft. In contrast, it is relatively easy to produce panel-method-type grids that are only on the aircraft surface.

This raises a question: Is it possible to combine the surface geometry grid used by panel methods, with some easy-to-generate flow-field grid and use the combination to solve nonlinear fluid flow problems? The answer is yes, as demonstrated by the TRANAIR code and the work that led to it (refs. 55-59). This section provides a brief introduction to the technique, and how it evolved. To the user, TRANAIR appears to be a panel code since the input is panel-code-like; however, the solution techniques TRANAIR uses are not those of a panel code.

The basic approach used in TRANAIR is to embed the surface panels in a rectangular box of grid points, as shown in figure 30. The initial formulation (sec. II of ref. 56) was based on Green's third theorem (eq. (7)), and combined the surface-integral-generated influence-coefficients with the volume integrals. The rectangular grid was used to evaluate the volume integral, for every point of the rectangular and surface grids, with fast Fourier transforms. This Green's theorem approach was able to solve the nonlinear full-potential equation if there were no shocks, but proved to be unstable when shocks were present. By resorting to more powerful mathematical methods involving optimization, supercritical results using influence-coefficients were subsequently obtained (refs. 55, 56); however, the computational cost was extremely high.

The most recent version of TRANAIR (refs. 57-59) still uses panels and the rectangular grid, but does not use influence-coefficients. Instead, the cells formed by the rectangular grid are used to discretize the full-potential equation with tri-linear basis-function finite elements. The surface panels, which slice through some of the finite-element cells, alter the finite-element discretization in the vicinity of boundary surfaces.

At the perimeter of the rectangular grid, the equation set being solved changes from the full-potential equation to the Prandtl-Glauert equation. As a consequence, the rectangular computational grid need only encompass the nonlinear flow regions (which are only near the aircraft). The far-field boundary condition of zero potential at infinity is automatically satisfied by the discrete Green's function (for the Prandtl-Glauert equation) used in the formulation. Consequently, the solution domain extends to infinity, even though the computational grid is finite, as indicated in figure 30.

The finite-element discretization yields a set of nonlinear algebraic equations which are solved iteratively, using Newton linearization, multiple preconditioners, and an optimization algorithm called GMRES (generalized minimal residual). Details are given in references 58-60. The computer run cost based on this approach is much less than with the original influence-coefficient/optimization approach.

The input to TRANAIR is essentially that of the PAN AIR code, that is, the surface grids of panel corner points supplemented by the box of rectangular flow-field grid points. This enables transonic flow to be computed about very complex configurations without having to generate a surface-conforming flow-field grid. For example, TRANAIR has been used to compute transonic full-

potential solutions for the F-16A, using the rectangular grid box and paneled geometry of figure 30. For the half geometry shown, the grid box contains $129 \times 33 \times 33$ points, and the aircraft contains about 3,500 panels. Two views of the surface paneling are shown in figure 31. In this model, the wing-tip missiles and launchers are not included.

F-16A supercritical wing-pressure results (ref. 57) are shown in figure 32. The free-stream Mach number is 0.9 and the angle of attack is 4° . The experimental data for the outboard station indicates separated flow near the trailing edge. This is probably a result of the wing-tip missiles and launcher that were part of the wind-tunnel model. The wind-tunnel data indicate a shock at approximately 75% chord for the four inboard stations. TRANAIR also indicates a shock, but it is slightly downstream of the shock predicted by the wind tunnel. This result is generally expected from a conservative full-potential solution, a result of the absence of a boundary-layer correction (fig. 40 in ref. 61). The shock predicted by TRANAIR is smeared over 5 to 6 grid cells, and at the 2 outboard stations where there are only about 11 rectangular-grid points spanning the chord, the shock is completely washed out. Increasing the grid density in the x-direction (streamwise) greatly reduces the shock smearing. To better resolve rapidly varying flow behavior without increasing the flow-field grid density everywhere, techniques such as local grid refinement, wherein individual cells of the rectangular grid are subdivided into smaller cells, or higher-order finite-element-basis functions are needed.

The coarseness of the rectangular grid is particularly evident in the leading-edge region of the wing. An example is shown in figure 33, at about 70% semispan. The first 18% of the wing chord is spanned by only three cells of the rectangular grid. Consequently, with this coarse uniform grid, TRANAIR fails to capture the leading-edge pressure peaks. The subsequent addition of local grid refinement has enabled these pressure peaks to be resolved (ref. 62).

7. CONCLUDING REMARKS

An attempt has been made to give an overview of the basics of the panel method and to provide some fairly specific details on how the basics can be implemented. The tools at the disposal of the panel-method user are (1) surface panels of source-doublet-vorticity distributions that can represent nearly arbitrary geometry, and (2) extremely versatile boundary-condition capabilities that can frequently be used for creative modeling.

Panel methods have reached a relatively mature stage of development. Their fundamental limitation is that they solve only linear differential equations. Even so, they are widely used in the aerospace industry because they can be used to model extremely complicated geometry.

Recently, panel-method technology has been combined with other procedures to solve transonic flow problems. For example, the TRANAIR code has been able to solve the full-potential equation for the F-16A at supercritical Mach numbers. It does this by combining surface

panels with a rectangular flow-field grid, thereby eliminating the often difficult task of creating three-dimensional, surface-fitted, flow-field grids. To the user, TRANAIR appears to be a panel code because the input is essentially the same as that of a panel code; however, the actual solution process is based on finite-element and optimization techniques.

Ames Research Center
National Aeronautics and Space Administration
Moffett Field, CA 94035-1000, February 13, 1990

APPENDIX A

PAN AIR IMPLEMENTATION OF SECTION 3 MATERIAL

The general approach common to panel methods was described in section 3. Here, a brief description is presented of how that approach is actually implemented in the PAN AIR code.

Recall that PAN AIR breaks each panel into eight triangular subpanels to maintain doublet-strength continuity within a network of panels. Consequently, separate linear source and quadratic doublet distributions are used over each subpanel, instead of there being a single source and single doublet distribution over the entire panel. The source distributions are chosen to be linear polynomials

$$\sigma(\xi, \eta) = \sigma_0 + \sigma_\eta \eta + \sigma_\xi \xi \quad (35)$$

and the doublet distributions are chosen to be quadratic polynomials

$$\mu(\xi, \eta) = \mu_0 + \mu_\xi \xi + \mu_\eta \eta + \mu_{\xi\xi} \frac{\xi^2}{2} + \mu_{\xi\eta} \xi \eta + \mu_{\eta\eta} \frac{\eta^2}{2} \quad (36)$$

where ξ and η are the in-plane coordinates of a local (ξ, η, ζ) coordinate system associated with each subpanel.

Panel and Network Singularity Parameters

The linear sources contribute three unknown coefficients ($\sigma_0, \sigma_\xi, \sigma_\eta$) per subpanel, and the quadratic doublets contribute six additional unknown coefficients per subpanel, giving a total of 72 unknowns per panel. To solve a system of equations involving 72M unknowns, where M is the number of panels, would be extremely inefficient. A better approach is to relate the 72 subpanel coefficients to values of the source-doublet strengths at a small number of discrete points. PAN AIR uses two sets of points: one is used to define panel singularity parameters, and the other is used to define the network singularity parameters. The panel singularity parameters are used to evaluate panel influence-coefficients, and to relate the 72 coefficients to the network singularity parameters $\{\lambda\}$ appearing in equation (17) in section 3:

$$[AIC]\{\lambda\} = \{b\}$$

The eight subpanels of a panel are shown in figure 34, along with the network singularity-parameter points (locations). Both source and doublet singularity parameters are defined at panel center points. Only doublet singularity parameters are defined along the network edges; these are used to enforce doublet strength continuity across network abutments. We will not discuss this aspect of PAN AIR; we will only discuss the relationships between the 72 coefficients and the panel and network singularity parameters.

The panel singularity-parameter points are shown in the lower portion of figure 35. There are five points for the source and nine points for the doublet. The panel source and doublet singularity parameters are the values of the source and doublet strengths at these points; they are labeled $\sigma_1, \dots, \sigma_5$, and μ_1, \dots, μ_9 , respectively. These panel source and doublet singularity parameters are expressed in terms of 9 network source and 21 doublet singularity parameters, $\{\lambda^S\}$ and $\{\lambda^D\}$, respectively, located at the panel center point and at the neighboring panel center points indicated by the asterisks in the upper portion of figure 35. (When a panel is nearer a network edge than is shown in fig. 35, neighboring singularity parameters that are different from those shown are used.) This is done through what the PAN AIR theory document calls source and doublet "outer" spline matrices $[B^S]$ and $[B^D]$, respectively (ref. 11). There is one each of these two matrices for each panel.

To relate the panel singularity-strength parameters (shown in the lower half of fig. 35) to the three source and six doublet coefficients appearing in equations (35) and (36), PAN AIR uses source and doublet "subpanel" spline matrices $[SPSPL^S]$ and $[SPSPL^D]$, respectively. There is one each of these two matrices for each subpanel.

The actual construction of the outer and subpanel spline matrices is described in appendix I of reference 11. Here, we simply show how they are used. For the sources, we can now use equation (35) and the matrices $[SPSPL^S]$ and $[B^S]$ to obtain, for subpanel k,

$$\begin{aligned}
\sigma(\xi, \eta)_k &= \begin{bmatrix} 1 & \xi & \eta \end{bmatrix}_k \begin{Bmatrix} \sigma_o \\ \sigma_\xi \\ \sigma_\eta \end{Bmatrix}_k \\
&= \begin{bmatrix} 1 & \xi & \eta \end{bmatrix}_k \begin{bmatrix} \text{SPSPL}^S \end{bmatrix}_k \begin{Bmatrix} \sigma_1 \\ \sigma_2 \\ \sigma_3 \\ \sigma_4 \\ \sigma_5 \end{Bmatrix} \\
&\quad \begin{matrix} 3 \times 5 & 5 \times 9 & 9 \times 1 \end{matrix} \\
&= \begin{bmatrix} 1 & \xi & \eta \end{bmatrix}_k \begin{bmatrix} \text{SPSPL}^S \end{bmatrix}_k \begin{bmatrix} B^S \end{bmatrix} \begin{Bmatrix} \lambda^S \end{Bmatrix} \quad (37)
\end{aligned}$$

Similarly, equation (36) gives, for the doublet distribution on subpanel k ,

$$\begin{aligned}
\mu(\xi, \eta)_k &= \begin{bmatrix} 1 & \xi & \eta & \frac{\xi^2}{2} & \xi\eta & \frac{\eta^2}{2} \end{bmatrix}_k \begin{Bmatrix} \mu_o \\ \mu_\xi \\ \mu_\eta \\ \mu_{\xi\xi} \\ \mu_{\xi\eta} \\ \mu_{\eta\eta} \end{Bmatrix}_k \\
&= \begin{bmatrix} 1 & \xi & \eta & \frac{\xi^2}{2} & \xi\eta & \frac{\eta^2}{2} \end{bmatrix}_k \begin{bmatrix} \text{SPSPL}^D \end{bmatrix}_k \begin{Bmatrix} \mu_1 \\ \vdots \\ \mu_9 \end{Bmatrix} \\
&\quad \begin{matrix} 6 \times 9 & 6 \times 9 & 9 \times 21 & 21 \times 1 \end{matrix} \\
&= \begin{bmatrix} 1 & \xi & \eta & \frac{\xi^2}{2} & \xi\eta & \frac{\eta^2}{2} \end{bmatrix}_k \begin{bmatrix} \text{SPSPL}^D \end{bmatrix}_k \begin{bmatrix} B^D \end{bmatrix} \begin{Bmatrix} \lambda^D \end{Bmatrix} \quad (38)
\end{aligned}$$

Panel Influence Coefficient Matrices

Equations (37) and (38) relate the source and doublet distributions, respectively, of a subpanel, to the panel and network singularity parameters. Equations (9) and (11) are then used to obtain the perturbation potential and velocity

components at an arbitrary point P in terms of the panel singularity parameters (five for the source, nine for the doublet). That is, a relationship of the form

$$\begin{Bmatrix} \phi(P) \\ \bar{v}(P) \end{Bmatrix} = \begin{bmatrix} \text{PIC}^S \end{bmatrix} \begin{Bmatrix} \sigma_1 \\ \vdots \\ \sigma_5 \end{Bmatrix} + \begin{bmatrix} \text{PIC}^D \end{bmatrix} \begin{Bmatrix} \mu_1 \\ \vdots \\ \mu_9 \end{Bmatrix} \quad (39)$$

is determined, where $[\text{PIC}^S]$ and $[\text{PIC}^D]$ are panel influence-coefficient matrices for the sources and doublets, respectively. This is done as follows. To determine the potential, we start with equation (9):

$$\phi(P) = \frac{1}{k} \iint_S \left[\frac{-\sigma(Q)}{R} + \mu(Q) \hat{n} \cdot \bar{v}_Q \frac{1}{R} \right] dS_Q \quad (40)$$

Using equation (37), the potential owing to the panel source distributions is

$$\begin{aligned}
\phi^S(P) &= \frac{-1}{4\pi} \iint_S \frac{\sigma(Q)}{R} dS_Q \\
&= \frac{-1}{4\pi} \sum_{k=1}^8 \iint_{\Delta_k} \frac{1}{R} \begin{bmatrix} 1 & \xi & \eta \end{bmatrix} \begin{bmatrix} \text{SPSPL}^S \end{bmatrix} \begin{Bmatrix} \sigma_1 \\ \vdots \\ \sigma_5 \end{Bmatrix} d\xi d\eta \quad (41)
\end{aligned}$$

where Δ_k represents one of the panel's eight subpanels. The subpanel spline matrix and the vector of panel source singularity parameters are not functions of the local sub-panel coordinates and can be extracted from the integral, giving

$$\phi^S(P) = \frac{-1}{4\pi} \sum_{k=1}^8 \left[\iint_{\Delta_k} \frac{1}{R} \begin{bmatrix} 1 & \xi & \eta \end{bmatrix} d\xi d\eta \right] \begin{bmatrix} \text{SPSPL}^S \end{bmatrix} \begin{Bmatrix} \sigma_1 \\ \vdots \\ \sigma_5 \end{Bmatrix} \quad (42)$$

Comparing equations (42) and (39), we see that the underlined portion of equation (42) gives the elements of the first row of the $[\text{PIC}^S]$ matrix. The same approach is used to obtain the other rows of both matrices appearing in equation (40). Of course all the surface integrals similar to the one appearing in equation (42) must still be evaluated. This step is described in appendix B.

Assembled Influence Coefficients

Equation (39) gives the contribution of a single panel to the perturbation potential and velocity at a point. To arrive at the equation $[AIC]\{\lambda\} = \{b\}$, we have to assemble the effects of each panel. This is simply done with superposition, which is allowed since we are solving discretized equations corresponding to a linear partial differential equation.

The first step is to use the outer spline matrices to express equation (39) in terms of the network singularity parameters, namely

$$\begin{Bmatrix} \phi(P) \\ \vec{v}(P) \end{Bmatrix} = \underbrace{[PIC^S][B^S]}_{[IC^S]_{\text{panel}}} \{\lambda^S\} + \underbrace{[PIC^D][B^D]}_{[IC^D]_{\text{panel}}} \{\lambda^D\} \quad (43)$$

The next step is to move to another panel, repeat the construction of equation (43), and superimpose the results. An example of this, for the source contribution to the potential at point P owing to two adjacent panels, is shown in figure 36. Applying this process to all the panels of each network then produces an equation of the form

$$\begin{Bmatrix} \phi(P) \\ \vec{v}(P) \end{Bmatrix} = \begin{bmatrix} IC^S & IC^D \end{bmatrix} \begin{Bmatrix} \lambda^S \\ \lambda^D \end{Bmatrix} \quad (44)$$

where N_S = the number of network source singularity parameters, N_D = the number of network doublet singularity parameters, and $N = N_S + N_D$ is the total number of singularity parameters for all the networks of the configuration (except for those involved with doublet matching across network abutments, which we have ignored). Equation (44) gives the effect of all panels on the (perturbation) potential and velocity at point P, in terms of all the network singularity parameters. Next, further partition equation (44) as

$$\begin{Bmatrix} \phi(P) \\ \vec{v}(P) \end{Bmatrix} = \begin{bmatrix} [IC^S] & [IC^D] \end{bmatrix} \begin{Bmatrix} \lambda^S \\ \lambda^D \end{Bmatrix} \quad (45a)$$

or

$$\begin{Bmatrix} \phi(P) \\ \vec{v}(P) \end{Bmatrix} = \begin{bmatrix} [IC] \\ [VIC] \end{bmatrix} \{\lambda\} \quad (45b)$$

or

$$\phi(P) = [IC] \{\lambda\} \quad , \quad \vec{v}(P) = [VIC] \{\lambda\} \quad (45c)$$

The latter form is what we need to use with the boundary conditions to finally arrive at $[AIC]\{\lambda\} = \{b\}$.

The Aerodynamic Influence Coefficient Matrix Equation

Recall from section 4 that the velocity boundary condition for an impermeable panel is

$$(\vec{V}_\infty + \vec{v}) \cdot \hat{n} = 0 \quad (46)$$

This is a specific example of the more general boundary condition, for point P, namely

$$c\phi(P) + (a\hat{n} + \vec{t}) \cdot \vec{v}(P) = b(P) \quad (47)$$

where c and a are arbitrary constants, and \vec{t} is a vector tangent to the panel.

Equation (46) is obtained from (47) by setting $c = 0$, $a = 1$, $\vec{t} = 0$, and $b(P) = -\vec{V}_\infty \cdot \hat{n}$. Equation (47) can be written as

$$c\phi(P) + \{a\hat{n} + \vec{t}\}^T \{\vec{v}(P)\} = b(P) \quad (48)$$

Then, using equations (45c), we obtain

$$\begin{bmatrix} c[IC] + \{a\hat{n} + \vec{t}\}^T [VIC] \end{bmatrix} \{\lambda\} = b(P) \quad (49)$$

The underlined portion of equation (49) is a row of what we have been calling the [AIC] matrix, since if N boundary conditions are imposed, we will have N equations like (49) relating the N unknown singularity parameters; that is

$$[AIC]\{\lambda\} = \{b\} \quad (50)$$

Two issues have been sidestepped in the above discussion. First is the question of doublet matching at network abutments. The reader is referred to the PAN AIR theory document (appendix F of ref. 11) for information on the doublet matching. Second is the question of how to analytically evaluate the surface integrals of the type appearing in equation (42). The complete story is contained in appendix J of reference 11 (approximately 200 pages). An abbreviated version, restricted to incompressible flow, is given herein in appendix B. Finally,

there is a third point which was mentioned in the Summary of Methods portion of section 4. For supersonic flow, the outer doublet spline matrices have to be "forward-weighted" to obtain stable results at high Mach numbers. The weighting refers to the weights used in a least-squares construction of the outer spline matrix. The forward-weighting obtains more information from upstream points than from downstream points. This is somewhat analogous to the use of forward-differencing in supersonic zones by finite-difference codes. This forward-weighting scheme is described in section I.1.2.4 of reference 11.

APPENDIX B

EVALUATION OF INFLUENCE-COEFFICIENT SURFACE INTEGRALS

In appendix A, equation (40) contained the expression

$$\phi(P) = \frac{1}{k} \iint_S \frac{-\sigma(Q)}{R} dS_Q \quad (51)$$

for the potential at P owing to a source distribution over a panel. The equations following equation (40) were for the PAN AIR implementation wherein a panel is subdivided into eight triangular subpanels. Here, we focus on a flat quadrilateral (or triangular) panel wherein a single source distribution covers the entire panel. This eliminates the subpanel spline matrices of appendix A, thereby simplifying the discussion (but it also prevents the doublet strength from being continuous). We also restrict our discussion to incompressible flow. The approach is that of sections D.5 and G.1 in reference 33. The general scheme is to integrate the surface integrals by parts (where possible); this reduces, by one, the singularity order of the resulting surface integrals, and introduces line integrals along the panel edges. The resulting expressions for the potential and velocity field are expressed below in terms of surface integrals denoted $H(M,N,K)$, and line integrals denoted $F(M,N,K)$, where M,N,K are integer exponents appearing in the integrands. We then show how $H(1,1,3)$ and $F(1,1,1)$ are evaluated analytically. These two integrals are the fundamental ones because, as shown in reference 33, all the remaining integrals can be computed recursively in terms of these two. It is $H(1,1,3)$ that causes the jump properties discussed earlier. The jump behavior will also be derived.

Velocity Owing to a Flat, Linear Source Panel

For a flat panel with a linear source distribution and incompressible flow, equation (51) becomes

$$\phi(x,y,z) = \frac{-1}{4\pi} \iint_S \frac{\sigma(\xi,\eta)}{R(\xi,\eta;x,y,z)} d\xi d\eta \quad (52)$$

where

$$\sigma(\xi,\eta) = \sigma_o + \sigma_\xi \xi + \sigma_\eta \eta$$

and

$$R = [(\xi - x)^2 + (\eta - y)^2 + z^2]^{1/2} = [r^2 + h^2]^{1/2} \quad (53)$$

and, as shown in figure 37, Σ denotes the flat panel, $Q(\xi,\eta,0)$ is a variable point of the panel, $P(x,y,z)$ is the influenced point, and h is the height of P above or below the panel (h is positive above the panel, and negative below it). The x-component of velocity at P is

$$v_x = \frac{\partial \phi}{\partial x} = \frac{-1}{4\pi} \frac{\partial}{\partial x} \iint_\Sigma \frac{\sigma}{R} d\xi d\eta = \frac{-1}{4\pi} \iint_\Sigma \frac{\partial}{\partial x} \left(\frac{1}{R} \right) \sigma d\xi d\eta \quad (54)$$

Noting that

$$\frac{\partial(1/R)}{\partial x} = -\frac{\partial(1/R)}{\partial \xi} \quad (55)$$

equation (54) is written as

$$v_x = \frac{1}{4\pi} \iint_\Sigma \frac{\partial}{\partial \xi} \left(\frac{1}{R} \right) \sigma d\xi d\eta \quad (56)$$

This form allows us to integrate by parts, using the formula shown in figure 38 (this result can be derived from the equations on p. 499 of ref. 63), to obtain

$$v_x = \frac{1}{4\pi} \left[\sum_1^4 \int_{\ell} \frac{1}{R} \sigma v_\xi d\ell - \iint_\Sigma \frac{1}{R} \frac{\partial \sigma}{\partial \xi} d\xi d\eta \right] \quad (57a)$$

where the sum is over the four panel edges. Similarly, the y-component of velocity is

$$v_y = \frac{1}{4\pi} \left[\sum_1^4 \int_{\ell} \frac{1}{R} \sigma v_\eta d\ell - \iint_\Sigma \frac{1}{R} \frac{\partial \sigma}{\partial \eta} d\xi d\eta \right] \quad (57b)$$

The z-component of velocity is

$$\begin{aligned} v_z &= \frac{\partial \phi}{\partial z} = -\frac{1}{4\pi} \iint_\Sigma \frac{\partial(1/R)}{\partial z} \sigma d\xi d\eta \\ &= \frac{1}{4\pi} \iint_\Sigma \frac{h}{R^3} \sigma d\xi d\eta \end{aligned} \quad (57c)$$

We now collect terms:

$$\begin{aligned}
\vec{v} &= v_x \hat{i} + v_y \hat{j} + v_z \hat{k} \\
&= -\frac{1}{4\pi} \iint_{\Sigma} \left[\frac{1}{R} \frac{\partial \sigma}{\partial \xi} \hat{i} + \frac{1}{R} \frac{\partial \sigma}{\partial \eta} \hat{j} + 0 \cdot \hat{k} \right] d\xi d\eta \\
&\quad + \frac{1}{4\pi} \sum_1^4 \iint_{\ell} \left[\frac{\sigma}{R} v_{\xi} \hat{i} + \frac{\sigma}{R} v_{\eta} \hat{j} + 0 \cdot \hat{k} \right] d\ell \\
&\quad + \frac{1}{4\pi} \iint_{\Sigma} \left[0 \cdot \hat{i} + 0 \cdot \hat{j} + \frac{\sigma h}{R^3} \hat{k} \right] d\xi d\eta \quad (58)
\end{aligned}$$

and for convenience, write the above as the vector equation

$$\vec{v} = \vec{v}_A + \vec{v}_B + \vec{v}_C \quad (59)$$

where the three terms on the right-hand side of equation (59) are simply shorthand notations for the three lines, respectively, on the right-hand side of equation (58).

The next step is to express the various integrals appearing in equation (58) in terms of $(\xi - x)$ and $(\eta - y)$. This is done to put the integrals in a form that can be integrated analytically. To demonstrate how this is done, we will show the process for \vec{v}_B and \vec{v}_C . The process is the same for \vec{v}_A .

Starting with \vec{v}_B , the line integral contribution from edge ℓ is

$$\begin{aligned}
\vec{v}_B &= \frac{(v_{\xi}, v_{\eta}, 0)}{4\pi} \int_{\ell} \frac{\sigma}{R} d\ell \\
&= \frac{(v_{\xi}, v_{\eta}, 0)}{4\pi} \int_{\ell} (\sigma_o + \sigma_{\xi} \xi + \sigma_{\eta} \eta) \frac{1}{R} d\ell \\
&= \frac{(v_{\xi}, v_{\eta}, 0)}{4\pi} \int_{\ell} [(\sigma_o + \sigma_{\xi} x + \sigma_{\eta} y) + \sigma_{\xi} (\xi - x) \\
&\quad + \sigma_{\eta} (\eta - y)] \frac{1}{R} d\ell \quad (60)
\end{aligned}$$

Now define

$$\begin{aligned}
\sigma(x, y) &\equiv \sigma_o + \sigma_{\xi} x + \sigma_{\eta} y \\
\sigma_x &\equiv \sigma_{\xi} \\
\sigma_y &\equiv \sigma_{\eta} \quad (61)
\end{aligned}$$

This is done to emphasize that these terms are independent of ξ and η . Also define the general line integral $F(M, N, K)$ as

$$F(M, N, K) = \int_{\ell} \frac{(\xi - x)^{M-1} (\eta - y)^{N-1}}{R^K} d\ell \quad (62)$$

Then, equation (60) becomes

$$\begin{aligned}
\vec{v}_B &= \frac{(v_{\xi}, v_{\eta}, 0)}{4\pi} \{ \sigma(x, y) F(1, 1, 1) + \sigma_x F(2, 1, 1) \\
&\quad + \sigma_y F(1, 2, 1) \} \quad (63)
\end{aligned}$$

At this point let us pause and reflect on what is known and unknown. In principle, for an arbitrary point P the line integrals $F(M, N, K)$ can be evaluated for each edge of a panel and are, therefore, known. The coefficients σ_o , σ_{ξ} , and σ_{η} , are unknown. They are, however, related to the source singularity parameters through an outer spline matrix as discussed in appendix A. (The actual spline matrix used in ref. 33 is given by eq. (B-7) of that reference.) Thus, once the singularity parameters $\{\lambda\}$ are determined from $[AIC]\{\lambda\} = \{b\}$, everything in equation (63) is known, and the velocity at P (from the \vec{v}_B term) can be computed.

The procedure for the surface integrals is similar, as we illustrate for the contribution of \vec{v}_C to equation (58):

$$\begin{aligned}
\vec{v}_C &= \frac{(0, 0, 1)}{4\pi} \iint_{\Sigma} \frac{\sigma h}{R^3} d\xi d\eta \\
&= \frac{(0, 0, 1)}{4\pi} \left\{ \sigma(x, y) h \iint_{\Sigma} \frac{d\xi d\eta}{R^3} \right. \\
&\quad \left. + \sigma_x h \iint_{\Sigma} \frac{(\xi - x) d\xi d\eta}{R^3} + \sigma_y h \iint_{\Sigma} \frac{(\eta - y) d\xi d\eta}{R^3} \right\} \quad (64)
\end{aligned}$$

where equations (61) have been used. Now defining the general surface integrals $H(M, N, K)$ as

$$H(M, N, K) = \iint_{\Sigma} \frac{(\xi - x)^{M-1} (\eta - y)^{N-1}}{R^K} d\xi d\eta \quad (65)$$

permits us to write equation (64) as

$$\bar{v}_C = \frac{(0,0,1)}{4\pi} \left\{ \sigma(x,y) \cdot hH(1,1,3) + \sigma_x \cdot hH(2,1,3) + \sigma_y \cdot hH(1,2,3) \right\} \quad (66)$$

If we had analytic expressions for the $H(M,N,K)$ integrals, the \bar{v}_C contribution to the velocity field could be computed (in terms of the three unknown source coefficients) from equation (66). A similar expression is likewise obtained for the \bar{v}_A contribution.

Velocity Owing to a Flat, Quadratic Doublet Panel

Before showing how the fundamental integrals $H(1,1,3)$ and $F(1,1,1)$ are evaluated, let us first discuss some of the properties of the various integrals (in practice, one only knows these properties after evaluating and studying the integrals). A more complete discussion appears in appendix D of reference 33. We will do this by first giving the complete equation for the velocity owing to a flat panel with the quadratic doublet distribution given by equation (36), and then describing the significance of the various terms. This equation is obtained from equations (D.130) through (D.140) of reference 33; the derivation follows the procedures described above for the source panel:

$$\begin{aligned} 4\pi\bar{v} = & (0,0,1) \cdot [\mu_{xx} + \mu_{yy}] \cdot H(1,1,1) \\ & + [(\mu_x, \mu_y, 0) \cdot hH(1,1,3) + (\mu_{xx}, \mu_{xy}, 0) \cdot hH(2,1,3) \\ & + (\mu_{xy}, \mu_{yy}, 0) \cdot hH(1,2,3)] + E1 + E2 \end{aligned} \quad (67)$$

where

$$\begin{aligned} E1 = & \sum_1^4 \underbrace{\left(\frac{-h\nu_\xi}{g}, \frac{-h\nu_\eta}{g}, \frac{-\bar{a}}{g} \right)}_{\substack{\text{unit vector in} \\ \text{direction of } \hat{\ell} \otimes \hat{g}}} \cdot g \cdot \left[\mu(x,y) F(1,1,3) \right. \\ & + \mu_x F(2,1,3) + \mu_y F(1,2,3) + \frac{1}{2} \mu_{xx} F(3,1,3) \\ & \left. + \mu_{xy} F(2,2,3) + \frac{1}{2} \mu_{yy} F(1,1,3) \right] \end{aligned} \quad (68a)$$

$$\begin{aligned} E2 = & \sum_1^4 (0,0,-1) \left[(\mu_x \nu_\xi + \mu_y \nu_\eta) F(1,1,1) \right. \\ & + (\mu_{xx} \nu_\xi + \mu_{xy} \nu_\eta) F(2,1,1) \\ & \left. + (\mu_{xy} \nu_\xi + \mu_{yy} \nu_\eta) F(1,2,1) \right] \end{aligned} \quad (68b)$$

and

$$\begin{aligned} \mu(\xi, \eta) = & \mu_0 + \mu_\xi \xi + \mu_\eta \eta + \frac{1}{2} \mu_{\xi\xi} \xi^2 + \mu_{\xi\eta} \xi\eta \\ & + \frac{1}{2} \mu_{\eta\eta} \eta^2, \quad (\xi, \eta) \in \Sigma \\ \mu(x, y) = & \mu_0 + \mu_\xi x + \mu_\eta y + \frac{1}{2} \mu_{\xi\xi} x^2 + \mu_{\xi\eta} xy \\ & + \frac{1}{2} \mu_{\eta\eta} y^2 \\ \mu_x(x, y) = & \mu_\xi + \mu_{\xi\xi} x + \mu_{\xi\eta} y \\ \mu_{xx} = & \mu_{\xi\xi} \end{aligned} \quad (69)$$

and so forth.

The first two terms in equation (67) arise from the surface integrals produced by the integration by parts—the last two terms arise from the line integrals. The first and last terms give velocity contributions that are in a direction normal to the panel; the second gives contributions that are in directions parallel to the panel. The third term is the “line-vortex” contribution and produces a velocity that is in the direction of $\hat{\ell} \times \hat{g}$, which is shown in figure 39.

Both $F(1,1,1)$ and $F(1,1,3)$ would be singular if they were to be evaluated at a point of the panel edge. In practice, this problem is avoided by having edge control points (if used at all) located slightly interior to the panel. For points near a panel edge, $F(1,1,1)$ is the weaker singularity, varying as $\ln(1/g^2)$, whereas $F(1,1,3)$ varies as $1/g$ (like a line vortex).

The quantity $hH(1,1,3)$ in the second term is what causes a panel's jump properties. Here, we see that it multiplies the in-plane first derivatives of the doublet strength; this is what causes the tangential velocities of a doublet panel to be discontinuous across the panel. Note that this property would not be predicted if the panel doublet strength were assumed to be constant.

The surface integral $H(1,1,3)$ is singular if computed at an interior point of the panel, but $hH(1,1,3)$ is well behaved (just having the jump behavior). For a point on the panel edge, $hH(1,1,3)$ depends on the angle at which the point is approached. This nonuniqueness is avoided as done for the F integral singularity behavior, that is, by using edge control points withdrawn slightly into the interior of the panel. The behavior of the doublet velocity near a panel edge can be used to impose the Kutta condition (see fig. 10 in ref. 9).

If the doublet strength is continuous from panel to panel (as in the PAN AIR, HISSS, MCAERO, and QUADPAN codes), the line-vortex contributions from adjacent panel edges will be equal and opposite and will cancel, and thus will not produce a resultant velocity field. (In general, a correct potential flow solution to flow about a general shape does not contain concentrated line-vortex-induced velocities.)

Ironically, if a constant-doublet-strength panel is used, the linear and quadratic terms in equation (67) disappear, and the only nonvanishing term is the spurious line-vortex term associated with $F(1,1,3)$; that is

$$\vec{v} = \frac{1}{4\pi} \sum_1^4 \hat{t} \otimes \hat{g} \mu_o g F(1,1,3) \quad (70)$$

If the above expression is evaluated for a specific panel geometry, the velocity field obtained will be the same as that produced by four line-vortex filaments all of strength $\Gamma = \mu_o$, placed head-to-tail around the panel perimeter. That is, a constant-strength-doublet panel is equivalent to a ring vortex. Although many subsonic-only codes use the line-vortex model (and often get away with it numerically), such an approach causes numerical disaster in supersonic flows.

Evaluation of $H(1,1,3)$

The surface integrals $H(M,N,K)$ were defined by equation (65). The fundamental integral $H(1,1,3)$ is then

$$H(1,1,3) = \iint_{\Sigma} \frac{d\xi d\eta}{R^3} \quad (71)$$

This integral can be evaluated by making two changes of variable. The first is to use polar coordinates in the plane of the panel, as indicated in figure 40, giving

$$\begin{aligned} H(1,1,3) &= \sum_{i=1}^4 \int_{\phi_i}^{\phi_{i+1}} \left[\int_0^r \frac{r dr}{(r^2 + h^2)^{3/2}} \right] d\phi \\ &= \sum_{i=1}^4 \int_{\phi_i}^{\phi_{i+1}} \left[\frac{1}{|h|} - \frac{1}{\sqrt{r^2 + h^2}} \right] d\phi \end{aligned} \quad (72)$$

The upper limit r extends to the boundary of Σ ; h is a constant as far as the integration is concerned; and i is the panel corner point number.

Next, the integration on ϕ is changed to a line integral along the panel edges. Referring to figures 40 and 41, equation (72) becomes

$$H(1,1,3) = \sum_{i=1}^4 \int_{\ell_i}^{\ell_{i+1}} \left[\frac{1}{|h|} - \frac{1}{\sqrt{\ell^2 + g^2}} \right] \frac{\bar{a} d\ell}{(\ell^2 + \bar{a}^2)} \quad (73a)$$

where

$$g^2 = \bar{a}^2 + h^2 \quad (73b)$$

and where \bar{a} is a different value for each edge L . The geometrical significance of g is shown in figure 42. The indefinite integrals of the two terms appearing in equation (73) can be found in tables (e.g., on p. 49, line 3 of ref. 64 for the second term, called I_2 below). The result is

$$H(1,1,3) = \sum_{i=1}^4 \left(\frac{\bar{a}}{|h|} I_1 - \bar{a} I_2 \right)_i \quad (74)$$

where

$$I_1 = \int_{\ell_i}^{\ell_{i+1}} \frac{d\ell}{\ell^2 + \bar{a}^2} = \frac{1}{|\bar{a}|} \tan^{-1} \left(\frac{\ell}{|\bar{a}|} \right) \Big|_{\ell_i}^{\ell_{i+1}} \quad (75a)$$

and

$$\begin{aligned} I_2 &= \int_{\ell_i}^{\ell_{i+1}} \frac{d\ell}{(\ell^2 + \bar{a}^2) \sqrt{\ell^2 + g^2}} \\ &= \frac{1}{|\bar{a}| |h|} \tan^{-1} \left(\frac{|h| \ell}{|\bar{a}| \sqrt{\ell^2 + g^2}} \right) \Big|_{\ell_i}^{\ell_{i+1}} \end{aligned} \quad (75b)$$

Thus, we can write

$$H(1,1,3) = \sum_{i=1}^4 \left(\frac{\bar{a}}{|\bar{a}|} \beta \right) \Big|_{\ell_i}^{\ell_{i+1}} \quad (76)$$

where

$$\beta = \tan^{-1} \left(\frac{\ell}{\bar{a}} \right) - \tan^{-1} \left(\frac{|h|\ell}{|\bar{a}|\sqrt{\ell^2 + g^2}} \right) \quad (77a)$$

and

$$\frac{\bar{a}}{|\bar{a}|} = \pm 1, \text{ see figure 41} \quad (77b)$$

Equation (76) contains 4 arctangents per edge, giving 16 arctangents to compute for a four-edged panel. After considerable effort, the above can be reduced to the following form, which contains only one arctangent per edge:

$$H(1,1,3) = \frac{1}{|\bar{h}|} \sum_{j=1}^4 (\beta_2 - \beta_1)_j \quad (78)$$

where

$$\begin{aligned} \beta_2 - \beta_1 &= \tan^{-1} \left(\frac{\bar{a}(\ell_2 c_1 - \ell_1 c_2)}{c_1 c_2 + \bar{a}^2 \ell_1 \ell_2} \right) \\ c_1 &= g^2 + |h|s_1 \\ c_2 &= g^2 + |h|s_2 \\ s_1 &= \sqrt{\ell_1^2 + g^2} \\ s_2 &= \sqrt{\ell_2^2 + g^2} \end{aligned} \quad (79)$$

and the subscripts 1 and 2 refer to the first and second end-points of each panel edge j . All the quantities in equations (78) and (79) can be computed from the coordinates of the panel corner points and the coordinate of the influenced point P . (For compressible flow the expression for $H(1,1,3)$ would also contain the free-stream Mach number since M_∞ is contained in the expression for R (see eqs. (5)).)

The Jump Property of $hH(1,1,3)$

Equation (78) can also be written as

$$hH(1,1,3) = \frac{h}{|\bar{h}|} \sum_{j=1}^4 (\beta_2 - \beta_1)_j \quad (80)$$

where

$$\tan \beta_i = \frac{\cos \theta \tan \alpha_i}{1 + \sin \theta \sqrt{1 + \tan^2 \alpha_i}}, \quad i = 1 \text{ or } 2 \quad (81)$$

and the meanings of the various new symbols are shown in figure 43. For an interior point of the panel, $h = 0$ and

$$\begin{aligned} \theta &= 0 \\ \alpha_1 &= \phi_1, \quad \alpha_2 = \phi_2 \\ \beta_1 &= \alpha_1, \quad \beta_2 = \alpha_2 \end{aligned} \quad (82)$$

Thus, equation (82) becomes

$$hH(1,1,3) = \frac{h}{|\bar{h}|} \sum_{j=1}^4 (\phi_2 - \phi_1)_j = 2\pi \frac{h}{|\bar{h}|} \quad (83)$$

And, as the point P passes through the panel, $hH(1,1,3)$ jumps by the value 4π . (The reader is encouraged to show that $hH(1,1,3) = 0$ when P is in the plane of the panel, but at a point exterior to the perimeter.)

We can now finally derive equation (21). Referring to equation (67), we see that the only nonzero term contributing to the tangential component of velocity at an interior point of the panel is $hH(1,1,3)$. Thus, equation (83) gives

$$4\pi \vec{v}_T = (\mu_x, \mu_y, 0) \cdot 2\pi \frac{h}{|\bar{h}|} \quad (84)$$

Denoting the two sides of the panel as the upper (U) and lower (L) sides, we use equation (84) to obtain

$$4\pi (\vec{v}_{TU} - \vec{v}_{TL}) = \vec{\nabla} \mu \cdot 2\pi [1 - (-1)] \quad (85)$$

and thus

$$\vec{v}_{TU} - \vec{v}_{TL} = \vec{\nabla} \mu \quad (86)$$

which is equation (21), except total rather than perturbation velocity appears in that equation. Both equations are correct, since the total and perturbation velocities differ only by the free-stream value, which is a constant.

The Line Integral $F(1,1,1)$

From equation (62), and figure 41, the fundamental line integral $F(1,1,1)$, for edge L, is

$$\begin{aligned} F(1,1,1) &= \int_L \frac{d\ell}{R} = \int_L \frac{d\ell}{\sqrt{(\xi-x)^2 + (\eta-y)^2 + h^2}} \\ &= \int_L \frac{d\ell}{\sqrt{a^2 + \ell^2 + h^2}} \\ &= \int_L \frac{d\ell}{\sqrt{\ell^2 + g^2}} = \ell n \left(\sqrt{\ell^2 + g^2} + \ell \right) \Big|_{\ell_1}^{\ell_2} \quad (87) \end{aligned}$$

This can be put in several forms, for example,

$$F_1(1,1,1) = \ell n \left(\frac{\sqrt{\ell_2^2 + g^2} + \ell_2}{\sqrt{\ell_1^2 + g^2} + \ell_1} \right) \quad (88a)$$

$$F_2(1,1,1) = \ell n \left(\frac{\sqrt{\ell_1^2 + g^2} - \ell_1}{\sqrt{\ell_2^2 + g^2} - \ell_2} \right) \quad (88b)$$

$$F_3(1,1,1) = \ell n \left[\frac{\left(\sqrt{\ell_1^2 + g^2} - \ell_1 \right) \left(\sqrt{\ell_2^2 + g^2} + \ell_2 \right)}{g^2} \right] \quad (88c)$$

Analytically, these three forms are identical. However, depending on the location of point P, the different forms produce different numerical results with a computer's finite precision arithmetic. Referring to figure 41, the following choice is recommended in reference 33 as the best for numerical accuracy.

<u>When</u>	<u>Use</u>
$\ell_1, \ell_2 \geq 0$	$F_1(1,1,1)$
$\ell_1, \ell_2 < 0$	$F_2(1,1,1)$
$\ell_1 < 0, \ell_2 \geq 0$	$F_3(1,1,1)$

APPENDIX C

IMPROPER INTEGRALS AND THEIR FINITE PART

The velocity equations for the source and doublet distributions both contain the term $hH(1,1,3)$ (see eqs. (66) and (67), respectively). The integral contained therein was evaluated for an arbitrary point P at (x,y,z) . In particular, z was nonzero. For P being an interior point of the panel, $z = h = 0$, we found that $hH(1,1,3)$ is generally well behaved. It has different values on opposite sides of the panel, but it is not singular.

If $z = 0$ had been used before evaluating the integral, the resulting integrand would have been simpler, but it would also have been singular. It turns out that singular (improper) integrals obtained in this manner can actually be correctly evaluated. This behavior is illustrated with the following two-dimensional example.

We are going to compute the two-dimensional velocity field owing to a doublet sheet (panel) in the x - y plane. The panel extends to infinity in the positive and negative y -directions, the doublet strength varies only in the x -direction, and the doublet axis is in the z -direction (normal to the panel).

We start with the expression for the potential at $P(x,z)$ owing to a line doublet extending from $y = -\infty$ to $y = +\infty$, passing through the point $x = z = 0$. The strength per unit length of the y -direction is $\bar{\mu}$, and the doublet axis is aligned with the z -direction:

$$\phi(x,z) = \frac{\bar{\mu}}{2\pi} \frac{z}{x^2 + z^2} \quad (89)$$

If instead of a single line doublet, we have an x -distribution of them located between $x = a$ and $x = b$, of strength $\mu(x_1)$ per unit length of the x -direction, the potential at (x,z) is

$$\phi(x,z) = \frac{1}{2\pi} \int_{x_1=a}^b \frac{\mu(x_1)z}{(x-x_1)^2 + z^2} dx_1 \quad (90)$$

Letting $\mu(x_1) = \mu_0$, a constant, we have for the potential and z -component of velocity, the expressions

$$\phi(x,z) = \frac{\mu_0}{2\pi} \int_{x_1=a}^b \frac{z}{(x-x_1)^2 + z^2} dx_1 \quad (91)$$

$$w(x,z) = \frac{\mu_0}{2\pi} \frac{\partial}{\partial z} \int_{x_1=a}^b \frac{z}{(x-x_1)^2 + z^2} dx_1 \quad (92)$$

We are going to evaluate the expression for $w(x,0)$ in two different ways. The first is to do the integration first, and then set $z = 0$ to find $w(x,0)$. This is how we did it in appendix B for $hH(1,1,3)$. The second way is to do the integration after setting $z = 0$; this will produce an improper integral containing a nonintegrable singularity.

Integration Before Setting $z = 0$

Performing the differentiation in equation (92) gives

$$w(x,z) = \frac{\mu_0}{2\pi} \left\{ \int_{x_1=a}^b \frac{(x-x_1)^2 dx_1}{[(x-x_1)^2 + z^2]^2} - z^2 \int_{x_1=a}^b \frac{dx_1}{[(x-x_1)^2 + z^2]^2} \right\} \quad (93)$$

If the velocity is wanted at a point x in the interval $a < x < b$, the term $(x-x_1)$ will become zero as the dummy variable of integration, x_1 , passes through the point x . However, the integrand will remain finite if we do not let $z = 0$ at this stage.

Performing the integration yields

$$w(x,z) = \frac{\mu_0}{2\pi} \left[\frac{x-x_1}{(x-x_1)^2 + z^2} \right]_{x_1=a}^{x_1=b} \quad (94)$$

Now we let $z = 0$, obtaining

$$w(x,0) = \frac{\mu_0}{2\pi} \left[\frac{-1}{x-a} + \frac{1}{x-b} \right] \quad (95)$$

This expression gives the z -component of velocity at any point along the x -axis; it is the same as that owing to a pair of concentrated line vortices (each of which produces a velocity $v = \Gamma/(2\pi r)$) located at $x = a$ and at $x = b$, whose strengths are equal and opposite, and of magnitude $\Gamma = \mu_0$. This is a confirmation of our earlier conclusion that the velocity field owing to a constant-strength doublet

panel is the same as that produced by line-vortex filaments (having the same strength as the doublet) being placed along the panel edges.

Integration After Setting $z = 0$

Here, we set $z = 0$ in equation (93), yielding the integral

$$w(x, 0) = \frac{\mu_0}{2\pi} \int_{x_1=a}^b \frac{dx_1}{(x - x_1)^2} \quad (96)$$

This is an improper integral, since if x is wanted at a point between a and b , the denominator is zero at $x_1 = x$. Because the integrand becomes infinite, this integral has no meaning in the ordinary sense. However, let us ignore this problem, and proceed as if the integrand were not singular. We then obtain

$$w(x, 0) = \frac{\mu_0}{2\pi} \frac{1}{x - x_1} \Big|_{x_1=a}^{x_1=b} = \frac{\mu_0}{2\pi} \left[\frac{-1}{x - a} + \frac{1}{x - b} \right] \quad (97)$$

Amazingly, we have obtained the correct answer, that is, we have obtained equation (95) again, even though the integrand is singular. This result is not a fluke. Reference 65 (p. 11) shows that, if

$$G(x, x_1) = \int \frac{f(x_1)dx_1}{(x - x_1)^{n+1}} \quad (98)$$

is the indefinite integral, for example, $G = 1/(x - x_1)$ in our simple example, then the correct finite value for the improper integral (that results from setting $z = 0$ before performing the integration) is

$$\int_{x_1=a}^b \frac{f(x_1)dx_1}{(x - x_1)^{n+1}} = G(x, b) - G(x, a) \quad n = 0, 1, 2, \dots \quad (99)$$

The expression on the left-hand side is merely notation used to indicate that the integrand is singular, but that the integral does in fact have a unique finite value. This value is usually called the "principal value" or the "finite part" of what appears to be an integral having an infinite value. Equation (99) says that this finite value can be computed from the indefinite integral by evaluating it at the two end-points a and b , as we did in our example. If the indefinite integral contains logarithmic terms, the absolute value of the arguments must be taken.

The reason for dealing with the finite part concept is that unlike our simple example, it may not be possible to

evaluate the nonsingular integral (the one containing the nonzero z), but it may be possible to find the indefinite integral when $z = 0$. Also, even if the nonsingular problem can be evaluated, it is usually simpler to evaluate the singular problem, as it was in our example.

There may be cases in which even the indefinite integral for the singular integral is not known. In such cases the finite part can be obtained numerically. One way is as follows. If

$$\int_{x_1=a}^b \frac{f(x_1)dx_1}{(x - x_1)^2} \quad (100)$$

is the improper integral obtained by setting $z = 0$ before doing the integration, the finite part can be computed from the formula

$$\begin{aligned} & \int_{x_1=a}^b \frac{f(x_1)dx_1}{(x - x_1)^2} \\ &= \lim_{\epsilon \rightarrow 0} \left\{ \int_{x_1=a}^{x-\epsilon} \frac{f(x_1)dx_1}{(x - x_1)^2} + \int_{x_1=x+\epsilon}^b \frac{f(x_1)dx_1}{(x - x_1)^2} - \frac{2f(x)}{\epsilon} \right\} \end{aligned} \quad (101)$$

where ϵ is a small number. For a fixed value of x and ϵ , the two integrals on the right-hand side of equation (101) can be evaluated numerically. Their sum will be a "large" number, from which is subtracted another large number given by the last term. The limiting value of this difference, as ϵ goes to zero, exists and is the finite part. Equation (101) is a special case of the more general formula given by equation (13) of reference 64. Another numerical approach is given in reference 66 (pp. 42-47).

Contrary to what one might assume based on the above discussion, performing the integration before setting $z = 0$ does not always eliminate the appearance of improper integrals. A counter-example appears in reference 33 (appendix D.2), where a curved panel is examined. In that case, the integration-by-parts step we went through in appendix B is not done. The resulting integrals are all expressed in terms of a nonzero z , but as z approaches zero some of the integrals become improper. However, the collection of all the improper integrals sums identically to zero, and the improper integrals can consequently be ignored.

Additional information on improper integrals can be found in reference 37 (pp. 15-18) and in reference 11 (appendix J).

REFERENCES

1. Rubbert, P. E.; and Saaris, G. R.: A General Three-Dimensional Potential-Flow Method Applied to V/STOL Aerodynamics. SAE Paper No. 680304, April 1968.
2. Hess, J. L.: Calculation of Potential Flow about Arbitrary Three-Dimensional Lifting Bodies. Report No. MDC J5679-01, Douglas Aircraft Co., Long Beach, Calif., Oct. 1972.
3. Kraus, W.: Panel Methods in Aerodynamics. Numerical Methods in Fluid Dynamics, H. J. Wirz and J. J. Smolderen, eds., McGraw-Hill Book Company, New York, 1978, pp. 237-297.
4. Woodward, F. A.: Analysis and Design of Wing-Body Combinations at Subsonic and Supersonic Speeds. *J. Aircraft*, vol. 5, no. 6, Nov.-Dec. 1968, pp. 528-534.
5. Carmichael, R. L.; and Woodward, F. A.: An Integrated Approach to the Analysis and Design of Wings and Wing-Body Combinations in Supersonic Flow. NASA TN D-3685, 1966.
6. Tinoco, E. N.; and Mercer, J. E.: FLEXSTAB—A Summary of the Functions and Capabilities of the NASA Flexible Airplane Analysis Computer System. NASA CR-2564, 1975.
7. Woodward, F. A.: An Improved Method for the Aerodynamic Analysis of Wing-Body-Tail Configurations in Subsonic and Supersonic Flow, Part I, Theory and Applications. NASA CR-2228, 1973.
8. Morino, L.: Steady, Oscillatory, and Unsteady Subsonic and Supersonic Aerodynamics—Production Version (SOUSSA-P.1.1), Vol. I, Theoretical Manual. NASA CR-159130, 1980.
9. Carmichael, R. L.; and Erickson, L. L.: PAN AIR—A Higher Order Panel Method for Predicting Subsonic or Supersonic Linear Potential Flows about Arbitrary Configurations. AIAA Paper 81-1255, June 1981.
10. Derbyshire, T.; and Sidwell, K. W.: PAN AIR Summary Document (Version 1.0), NASA CR-3250, 1982.
11. Magnus, A. E.; and Epton, M. A.: PAN AIR—A Computer Program for Predicting Subsonic or Supersonic Linear Potential Flows about Arbitrary Configurations Using a Higher Order Panel Method. Vol. I, Theory Document (Version 1.0). NASA CR-3251, 1980.
12. Sidwell, K. W.; Baruah, P. K.; and Bussoletti, J. E.: PAN AIR—A Computer Program for Predicting Subsonic or Supersonic Linear Potential Flows about Arbitrary Configurations Using a Higher Order Panel Method. Vol. II, User's Manual (Version 1.0). NASA CR-3252, 1980.
13. Magnus, A. E.; Sidwell, K. W.; and Epton, M. A.: PAN AIR—A Computer Program for Predicting Subsonic or Supersonic Linear Potential Flows about Arbitrary Configurations Using a Higher Order Panel Method. Vol. III, Case Manual (Version 1.0). R. T. Medan, ed., NASA CR-3253, 1981.
14. Baruah, P. K.; Bussoletti, J. E.; Chiang, D. T.; Massena, W. A.; Nelson, F. D.; Furdon, D. J.; and Tsurusaki, K.: PAN AIR—A Computer Program for Predicting Subsonic or Supersonic Linear Potential Flows about Arbitrary Configurations Using a Higher Order Panel Method. Vol. IV, Maintenance Document (Version 1.0). NASA CR-3254, 1980.
15. Moran, J.; Tinoco, E. N.; and Johnson, F. T.: User's Manual—Subsonic/Supersonic Advanced Panel Pilot Code. NASA CR-152047, 1978.
16. Fornasier, L.: HISSS—A Higher-Order Subsonic/Supersonic Singularity Method for Calculating Linearized Potential Flow. AIAA Paper 84-1646, June 1984.
17. Bristow, D. R.; and Hawk, J. D.: Subsonic Panel Method for Designing Wing Surfaces from Pressure Distribution. NASA CR-3713, 1983.
18. Maskew, B.: Prediction of Subsonic Aerodynamic Characteristics—A Case for Low-Order Panel Methods. AIAA Paper 81-0252, Jan. 1981.
19. Maskew, B.: PROGRAM VSAERO—A Computer Program for Calculating the Non-Linear Aerodynamic Characteristics of Arbitrary Configurations: User's Manual. NASA CR-166476, 1982.

20. Youngren, H. H.; Bouchard, E. E.; Coopersmith, R. M.; and Miranda, L. R.: Comparison of Panel Method Formulations and Its Influence on the Development of QUADPAN, an Advanced Low Order Method. AIAA Paper 83-1827, July 1983.
21. Johnston, C. E.; Youngren, H. H.; and Sikora, J. S.: Engineering Applications of an Advanced Low-Order Panel Method. SAE Paper 851793, Oct. 1985.
22. von Karman, Theodore: Aerodynamics. McGraw-Hill Book Co., New York, 1963.
23. Liepmann, H. W.; and Roshko, A.: Elements of Gasdynamics. John Wiley and Sons, New York, 1957.
24. Ashley, H.: Engineering Analysis of Flight Vehicles. Addison-Wesley Publishing Co., Reading, Mass., 1974.
25. Hess, J. L.: A Fully Automatic Combined Potential-Flow Boundary-Layer Procedure for Calculating Viscous Effects on the Lifts and Pressure Distributions of Arbitrary Three-Dimensional Configurations. Report MDC J7491, Douglas Aircraft Co., Long Beach, Calif., June 1977.
26. Roberts, D. W.: Flow Analysis of Nozzle Installations with Strong Airplane Flow Interactions. NASA CR-166466, 1982.
27. Johnson, F. T.; Tinoco, E. N.; Lu, P.; and Epton, M. A.: Recent Advances in the Solution of Three-Dimensional Flows over Wings with Leading-Edge Vortex Separation. AIAA Paper 79-0282, Jan. 1979.
28. Hoeijmakers, H. W. M.; and Vaatstra, W.: A Higher-Order Panel Method Applied to Vortex Sheet Roll-Up. AIAA Paper 82-0096, Jan. 1982.
29. Kellogg, O. D.: Foundations of Potential Theory. Dover Publications, New York, 1953 (originally published by J. Springer, 1929).
30. Ward, G. N.: Linearized Theory of Steady High-Speed Flow. Cambridge University Press, Cambridge, England, 1955.
31. Hess, J. L.: Improved Solution for Potential Flow about Arbitrary Axisymmetric Bodies by the Use of a Higher-Order Surface Source Method. Computer Methods in Applied Mechanics and Engineering, vol. 5, no. 3, 1975, pp. 297-308.
32. Hess, J. L.; Friedman, D. M.; and Clark, R. W.: Calculation of Compressible Flow about Three-Dimensional Inlets with Auxiliary Inlets, Slats, and Vanes by Means of a Panel Method. NASA CR-174975, 1985.
33. Johnson, F. T.: A General Panel Method for the Analysis and Design of Arbitrary Configurations in Incompressible Flows. NASA CR-3079 1980.
34. Timoshenko, S.; and Woinowsky-Krieger, S.: Theory of Plates and Shells. Second ed. McGraw-Hill Book Co, New York, 1959.
35. Ashley, H.; and Landahl, M. T.: Aerodynamics of Wings and Bodies. Addison-Wesley Publishing Co., Reading, Mass., 1965.
36. Ehlers, F. E.; Epton, M. A.; Johnson, F. T.; Magnus, A. E.; and Rubbert, P. E.: An Improved Higher Order Panel Method for Linearized Supersonic Flow. AIAA Paper 78-15, Jan. 1978.
37. Ehlers, F. E.; Epton, M. A.; Johnson, F. T.; Magnus, A. E.; and Rubbert, P. E.: A Higher Order Panel Method for Linearized Supersonic Flow. NASA CR-3062, 1979.
38. Hess, J. L.; and Smith, A. M. O.: Calculation of Potential Flow about Arbitrary Bodies. Progress in Aeronautical Sciences, vol. 8, D. Kuchemann, ed., Pergamon Press, Oxford, 1967, pp. 1-138.
39. Sytsma, H. S.; Hewitt, B. L.; and Rubbert, P. E.: A Comparison of Panel Methods for Subsonic Flow Computation. AGARD-AG-241, 1979.
40. Margason, R. J.; Kjelgaard, S. O.; Sellers, W. L. III; Morris, C. E. K., Jr.; Walker, K. B.; and Shields, E. W.: Subsonic Panel Methods—A Comparison of Several Production Codes. AIAA Paper 85-0280, Jan. 1985.
41. Strang, W. Z.; Berdahl, C. H.; Nutley, E. L.; and Murn, A. J.: Evaluation of Four Panel Aerodynamic Prediction Methods (MCAERO, PANAIR, QUADPAN, and VSAERO). AIAA Paper 85-4092, Oct. 1985.

42. Fornasier, L.: Linearized Potential Flow Analysis of Complex Aircraft Configurations by HISSS, a Higher-Order Panel Method. AIAA Paper 85-0281, Jan. 1985.
43. Butter, D. J.: Compressibility Corrections Used in Panel Methods. British Aerospace Aircraft Group Report No. HSA-MAE-R-FDM-0039, Nov. 1978.
44. Brune, G. W.; and Rubbert, P. E.: Boundary-Value Problem of Configurations with Compressible Free-Vortex Flow. AIAA J., vol. 15, no. 10, Oct. 1977, pp. 1521-1523.
45. Chin, W. C.: Gothert's Rule with an Improved Boundary Condition: Subsonic Flow Relation Modified to Supersonic Flow. AIAA J., vol. 15, no. 10, Oct. 1977, pp. 1516-1518.
46. Melnik, R. E.; and Mason, W. H.: Mass Flux Boundary Conditions in Linear Theory. AIAA J., vol. 22, no. 11, Nov. 1984, pp. 1691-1692.
47. Strande, S.; Erickson, L.; Snyder, L.; and Carmichael, R.: PAN AIR Modeling Studies II: Side Slip Option, Network Gaps, Three-Dimensional Forebody Flow, and Thick Trailing Edge Representation. AIAA Paper 84-0220, Jan. 1984.
48. Thomas, J. L.; and Miller, D. S.: Numerical Comparisons of Panel Methods at Subsonic and Supersonic Speeds. AIAA Paper 79-0404, Jan. 1979.
49. Towne, M. C.; Strande, S. M.; Strande, S. M.; Erickson, L. L.; Kroo, I. M.; Enomoto, F. Y.; Carmichael, R. L.; and McPherson, K. F.: PAN AIR Modeling Studies. AIAA Paper 83-1830, July 1983.
50. Miller, S. G.; and Youngblood, D. B.: Applications of USSAERO-B and the PANAIR Production Code to the CDAF Model—A Canard/Wing Configuration. AIAA Paper 83-1829, July 1983.
51. Madson, M. D.; and Erickson, L. L.: PAN AIR Analysis of the NASA/MCAIR 279-3: An Advanced Supersonic V/STOL Fighter/Attack Aircraft. NASA TM-86838, 1986.
52. Tinoco, E. N.; Ball, C. N.; and Rice, F. A., II: PAN AIR Analysis of a Transport High-Lift Configuration. AIAA Paper 86-1811, June 1986.
53. Henderson, M. L.: Two-Dimensional Separated Wake Modeling and Its use to Predict Maximum Section Lift Coefficient. AIAA Paper 78-156, Jan. 1978.
54. Holst, T. L.; Slooff, J. W.; Yoshihara, H.; and Ballhaus, W. F., Jr.: Applied Computational Transonic Aerodynamics. B.M. Spee and H. Yoshihara, eds., AGARD-AG-266, 1982, p. 86.
55. Johnson, F. T.; James, R. M.; Bussoletti, J. E.; Young, D. P.; and Woo, A. C.: A Transonic Rectangular Grid Embedded Panel Method. AIAA Paper 82-0953, June 1982.
56. Erickson, L. L.; and Strande, S. M.: A Theoretical Basis for Extending Surface-Paneling Methods to Transonic Flow. AIAA J., vol. 23, no. 12, Dec. 1985, pp. 1860-1867.
57. Erickson, L. L.; Madson, M. D.; and Woo, A. C.: Application of the TRANAIR Full-Potential Code to Complete Configurations. ICAS 15th Congress Proceedings, Volume 1, American Institute of Aeronautics and Astronautics, Inc., 1986, pp. 313-323.
58. Rubbert, P. E.; Bussoletti, J. E.; Johnson, F. T.; Sidwell, K. W.; Rowe, W. S.; Samant, S. S.; Sengupta, G.; Weatherill, W. H.; Burkhart, R. H.; and Woo, A. C.: A New Approach to the Solution of Boundary Value Problems Involving Complex Configurations. Symposium on Future Directions of Computational Mechanics, ASME Winter Annual Meeting, Anaheim, CA, Dec. 1986, pp. 49-84.
59. Samant, S. S.; Bussoletti, J. E.; Johnson, F. T.; Burkhart, R. H.; Everson, B. L.; Melvin, R. G.; Young, D. P.; Erickson, L. L.; and Madson, M. D.: TRANAIR: A Computer Code for Transonic Analyses of Arbitrary Configurations. AIAA Paper 87-0034, Jan. 1987.
60. Wigton, L. B.; Yu, N. J.; and Young, D. P.: GMRES Acceleration of Computational Fluid Dynamics Codes. AIAA Paper 85-1491, July 1985.
61. Holst, T. L.: Numerical Computation of Transonic Flow Governed by the Full-Potential Equation. NASA TM-84310, 1983.

62. Madson, M. D.; and Erickson, L. L.: Toward the Routine Aerodynamic Analysis of Complex Configurations. Applied Computational Aerodynamics, P. A. Henne, ed. Vol. 125, Progress in Astronautics and Aeronautics, American Institute of Aeronautics and Astronautics, Inc., Washington, DC, 1990, pp. 701-751.
63. Wylie, C. R., Jr.: Advanced Engineering Mathematics. Second ed. McGraw-Hill Book Company, Inc., New York, 1960.
64. Bois, G. Petit: Tables of Indefinite Integrals. Dover Publications, Inc., New York, 1961.
65. Mangler, K. W.: Improper Integrals in Theoretical Aerodynamics. RAE Report 2424, Royal Aircraft Establishment, London, June 1951.
66. Mercer, J. E.; Weber, J. A.; and Lesferd, E. P.: Aerodynamic Influence Coefficient Method Using Singularity Splines. NASA CR-2423, 1974.

TABLE 1.— COMPARISON OF FORMULATIONS

Code name	Approximate date introduced	Panel geometry	Singularity type			Reference
			σ	μ	$\bar{\gamma}$	
M _∞ , subsonic only						
Lower-Order Hess	1965	Flat	Constant		Linear	2,38
MCAERO	1980	Piecewise flat ^a	Constant	Quadratic ^a		17
SOUSSA	1980	Hyperbolic paraboloid ^a	Constant	Constant		8
VSAERO	1982	Flat	Constant	Constant		18,19
LEV	1979	Hyperbolic paraboloid ^a	Linear	Quadratic ^a		27
QUADPAN	1983	Flat	Constant	Constant		20,21
Higher-Order Hess	1985	Parabolic	Linear		Linear	32
M _∞ , subsonic/supersonic						
Woodward-Carmichael	1966	Flat	Line distributions for bodies		Constant	4,5
USSAERO	1973	Flat	Constant		Linear in x Constant in y	7
PAN AIR	1981	Piecewise flat ^a	Linear	Quadratic ^a		9-15, 36,37
HISSE	1984	Piecewise flat ^a	Linear	Quadratic ^a		16,42
QUADPAN	1985	Piecewise flat ^a	Constant	Linear ^a		<i>b</i>

^aContinuous panel edge geometry or doublet strength.^bFrom October 1985 AIAA Workshop on Aerodynamic Analysis Using Panel Methods.

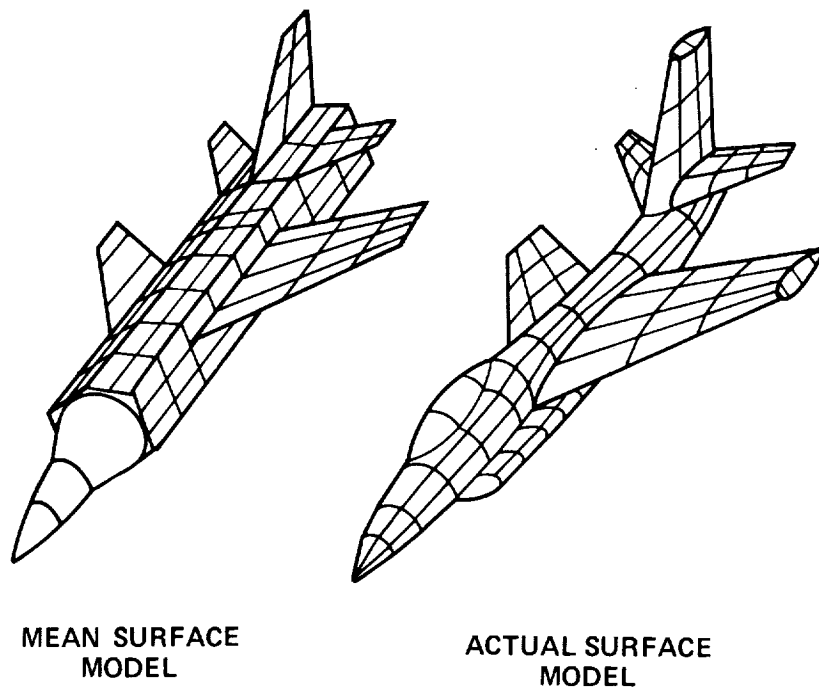


Figure 1.— Mean-surface and actual-surface panel models.

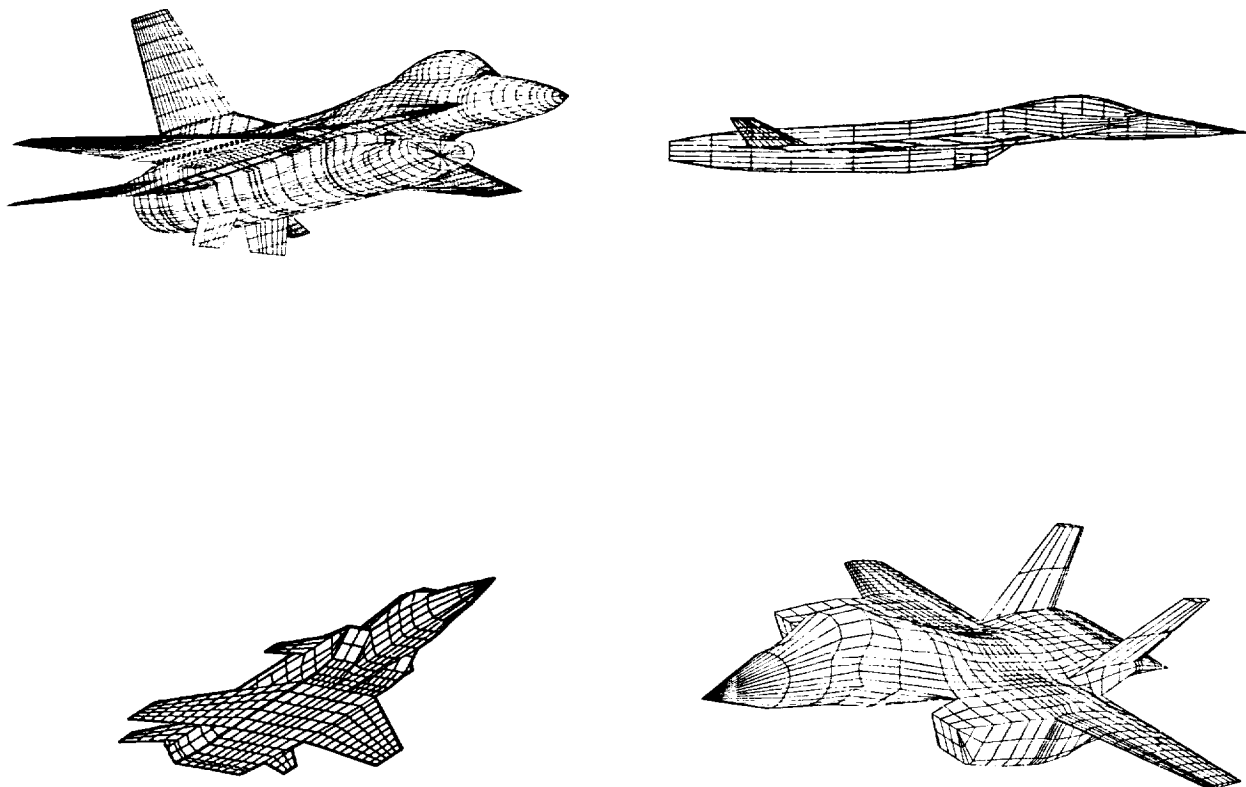
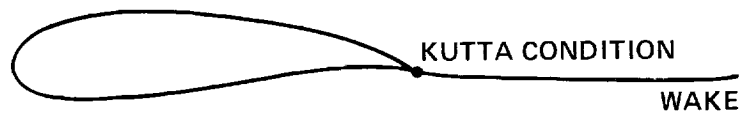
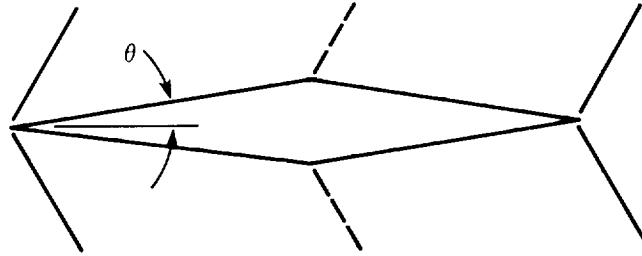


Figure 2.— Examples of surface paneling.



a) SUBSONIC $(1-M_\infty^2) \phi_{xx} + \phi_{yy} + \phi_{zz} = 0$



b) SUPERSONIC $(M_\infty^2-1) \phi_{xx} - \phi_{yy} - \phi_{zz} = 0$

Figure 3.- Panel methods predict linear potential flow by solving the Prandtl-Glauert equation. The weak shock solutions (small θ) of shock-expansion theory are predicted and yield wave drag.

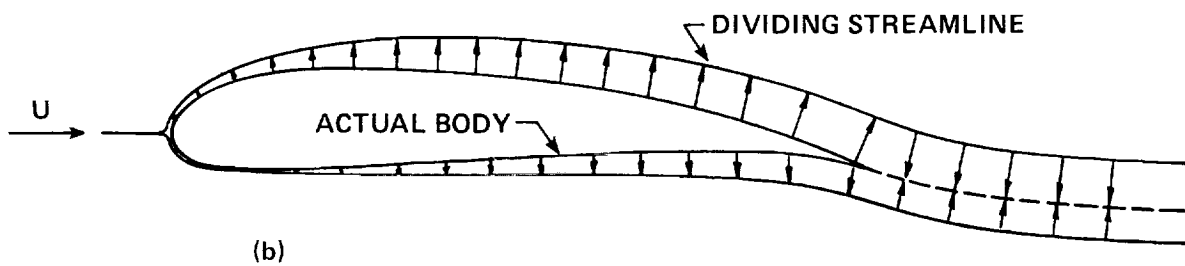
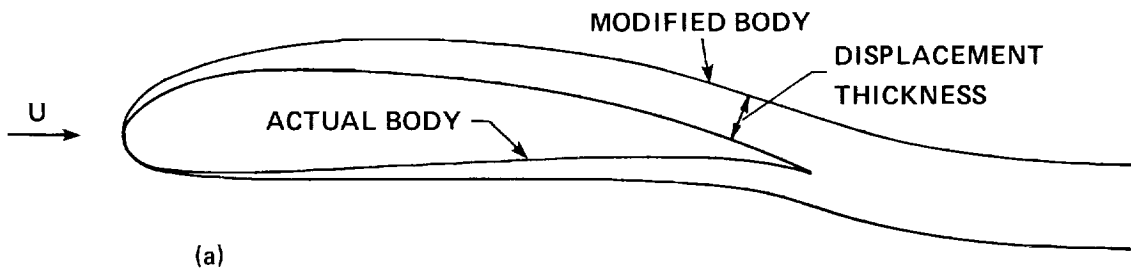


Figure 4.- Two methods of boundary-layer simulation (not to scale) (from reference 25). (a) Surface displacement; panels at modified body. (b) Surface blowing; panels at actual body.

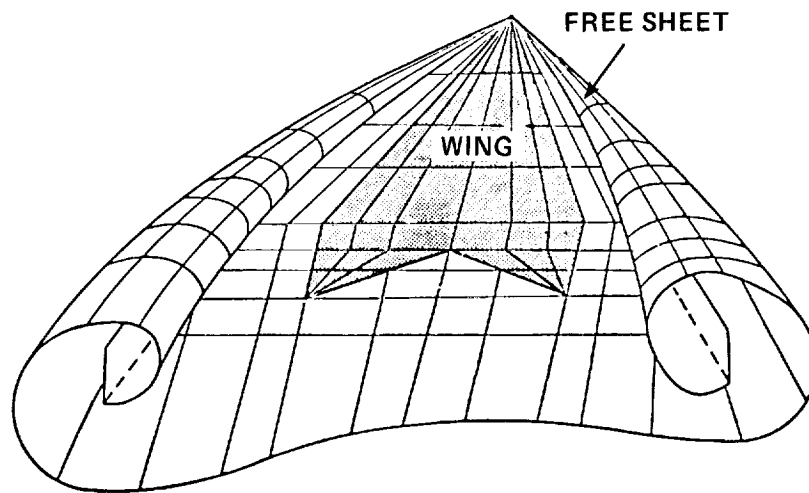


Figure 5.— Free vortex sheet model for sharp leading edges.

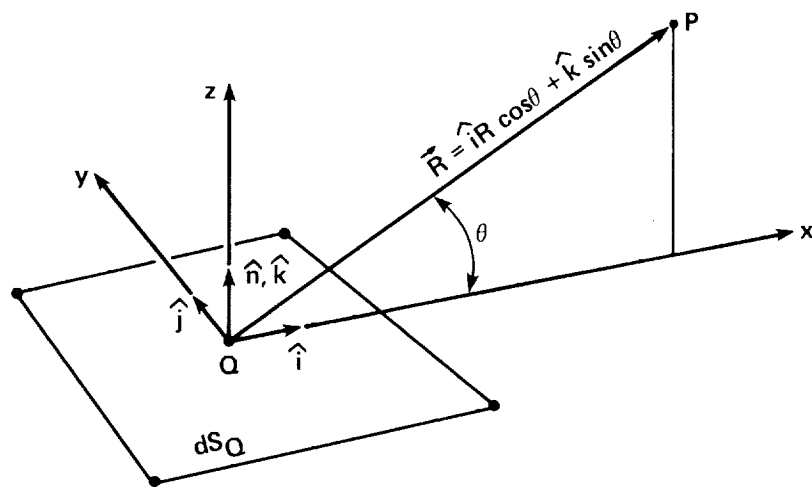


Figure 6.— Coordinate system used to obtain equation (6).

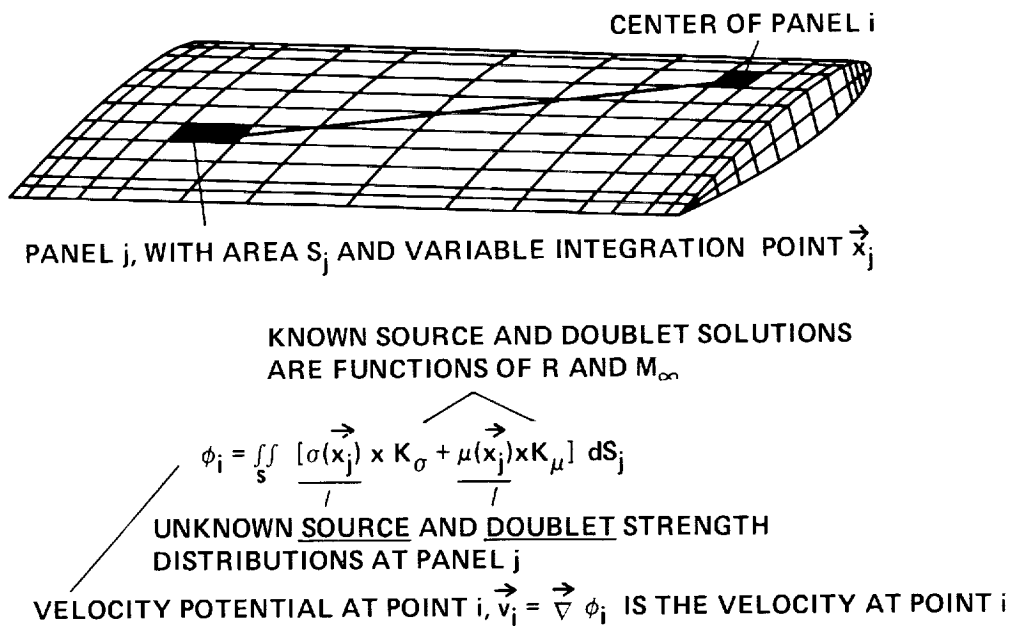


Figure 7.— The flow at center of panel i due to source and doublet distributions at panel j .

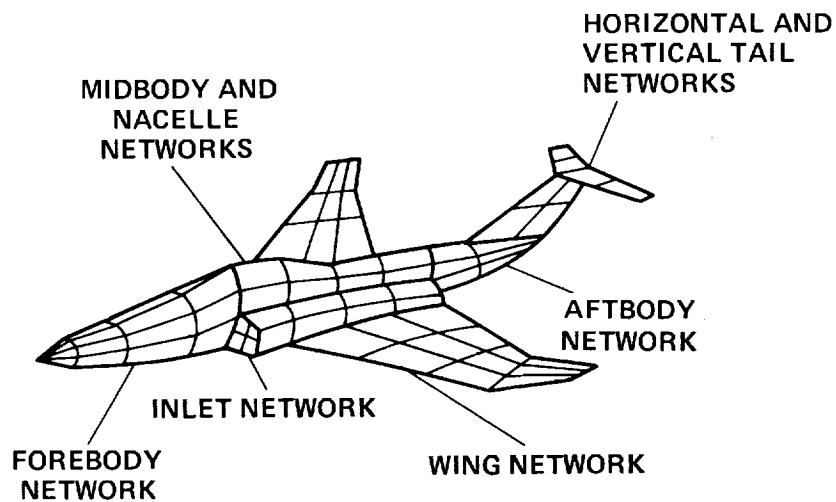
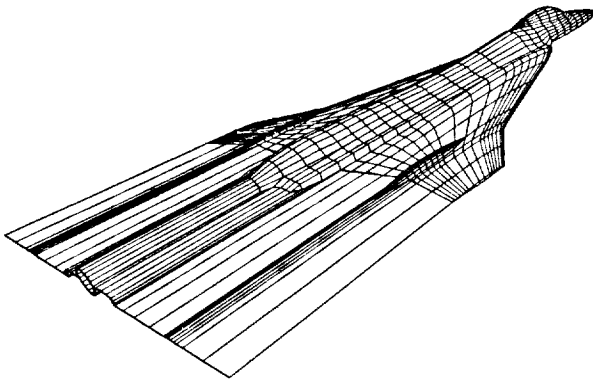
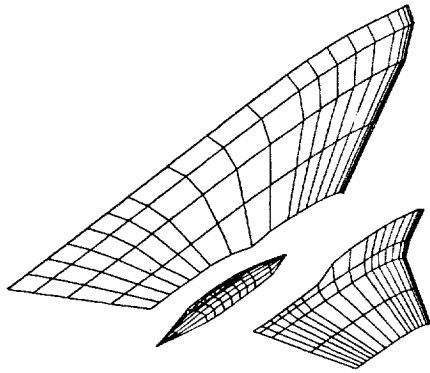
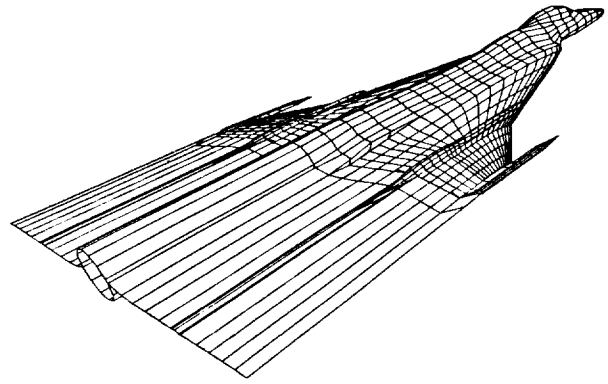


Figure 8.— Networks of surface panels. Each panel is a surface distribution of sources and doublets whose strengths are adjusted so as to satisfy the boundary conditions; for example, to make the flow tangent to the surfaces.



(a)



(b)

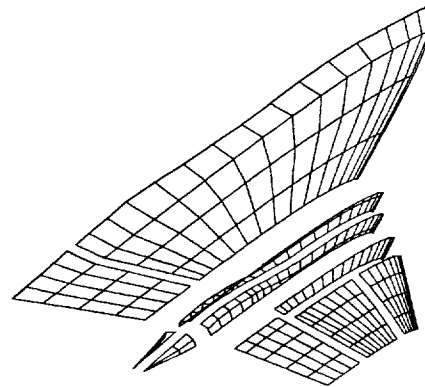


Figure 9.— Two models of the F-16XL showing different breakdowns of wing surface into networks. (a) Aircraft and wake paneling; wake has been truncated for visualization. (b) Exploded view of networks representing top half of wing.

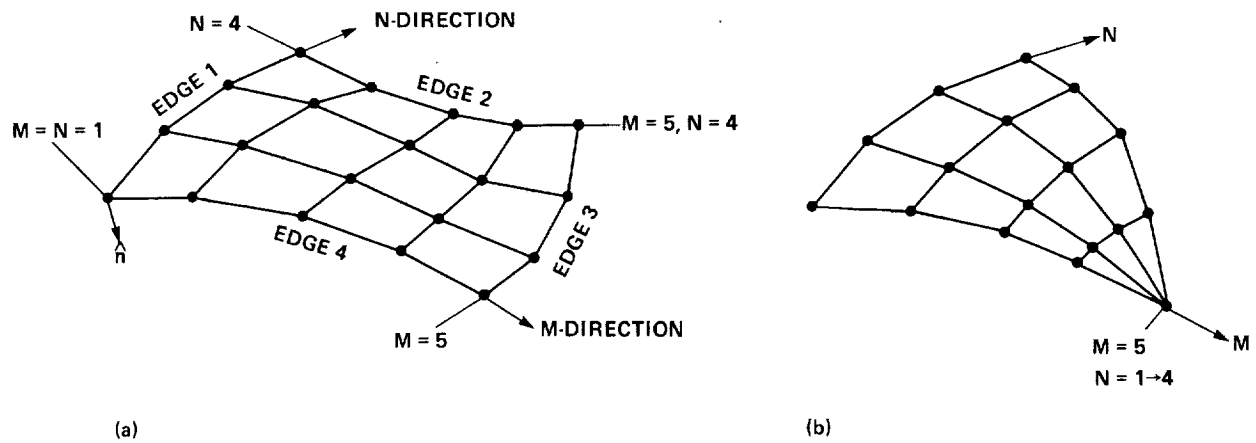


Figure 10.— $M \times N$ arrays of surface grid points used to define panel networks. The unit normal $\hat{n} = \hat{N} \times \hat{M}$ is used to distinguish between the two sides of a network or panel. (a) 5×4 grid. (b) 5×4 grid with collapsed edge.

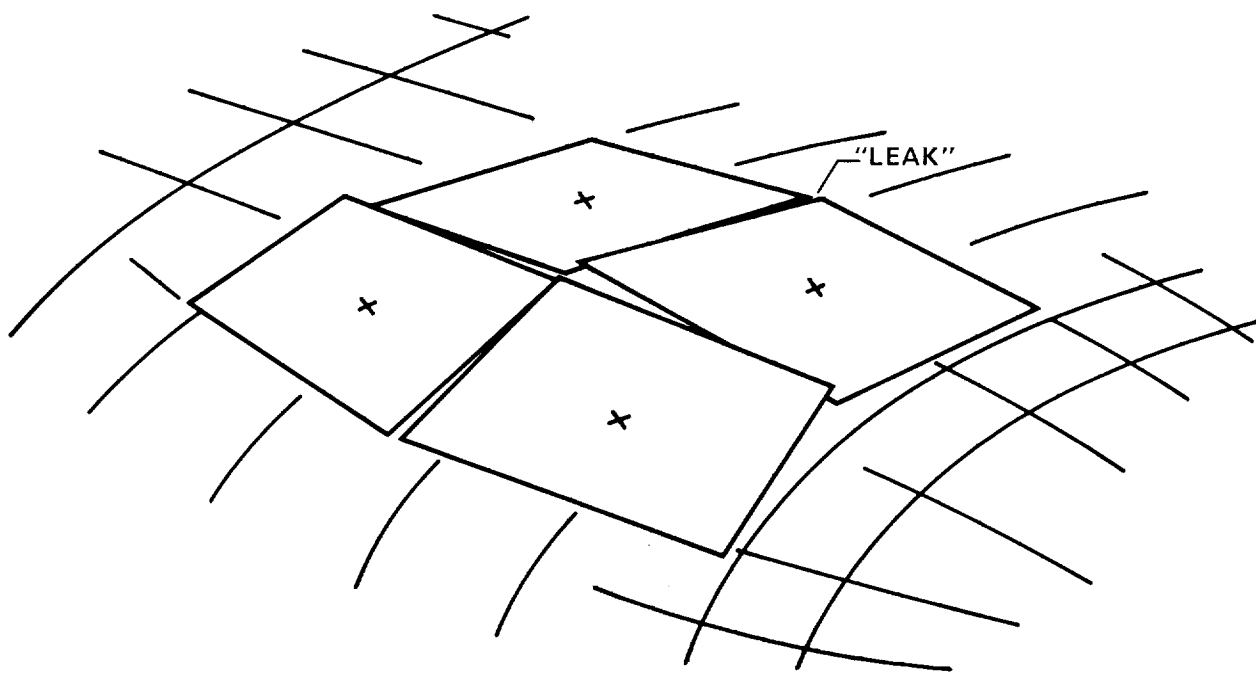
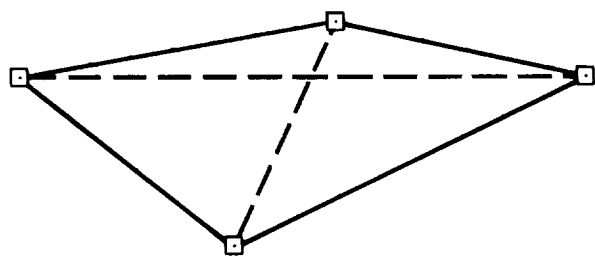
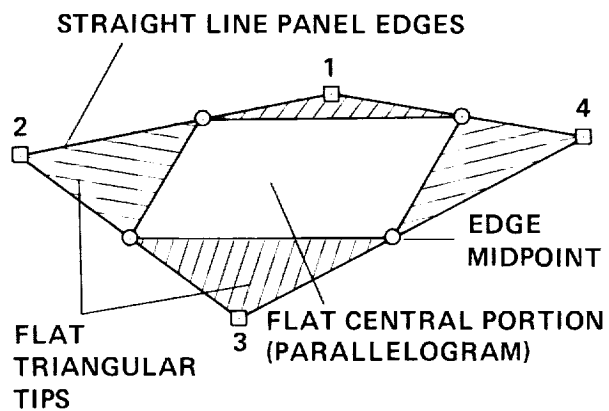


Figure 11.— Gaps produced by representing a curved surface with flat quadrilateral panels.

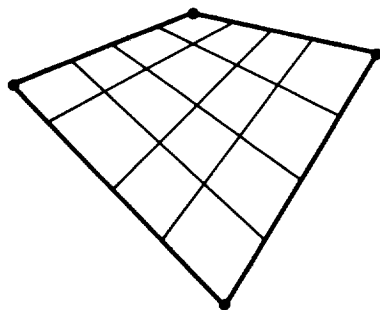


(a)

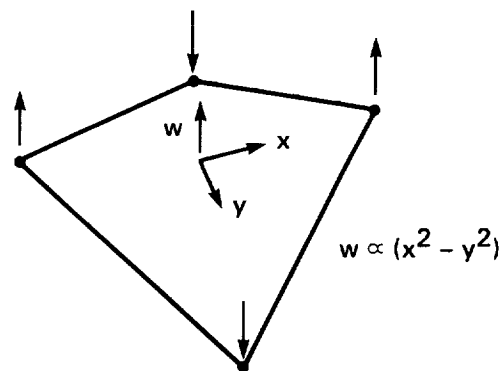
CORNER POINTS 1 AND 3 ARE BELOW THE PLANE OF THE FLAT CENTRAL PORTION AND CORNER POINTS 2 AND 4 ARE ABOVE THE PLANE OF THE FLAT CENTRAL PORTION



(b)



(c)



(d)

Figure 12.— Continuous panels constructed from four arbitrary points. (a) Piecewise flat; QUADPAN. (b) Piecewise flat; PAN AIR, HISSS, MCAERO. (c) Hyperbolic paraboloid; SOUSSA, LEV. (d) Figure 12(c) corresponds to the twisted shape a flat flexible plate takes when loaded as shown.

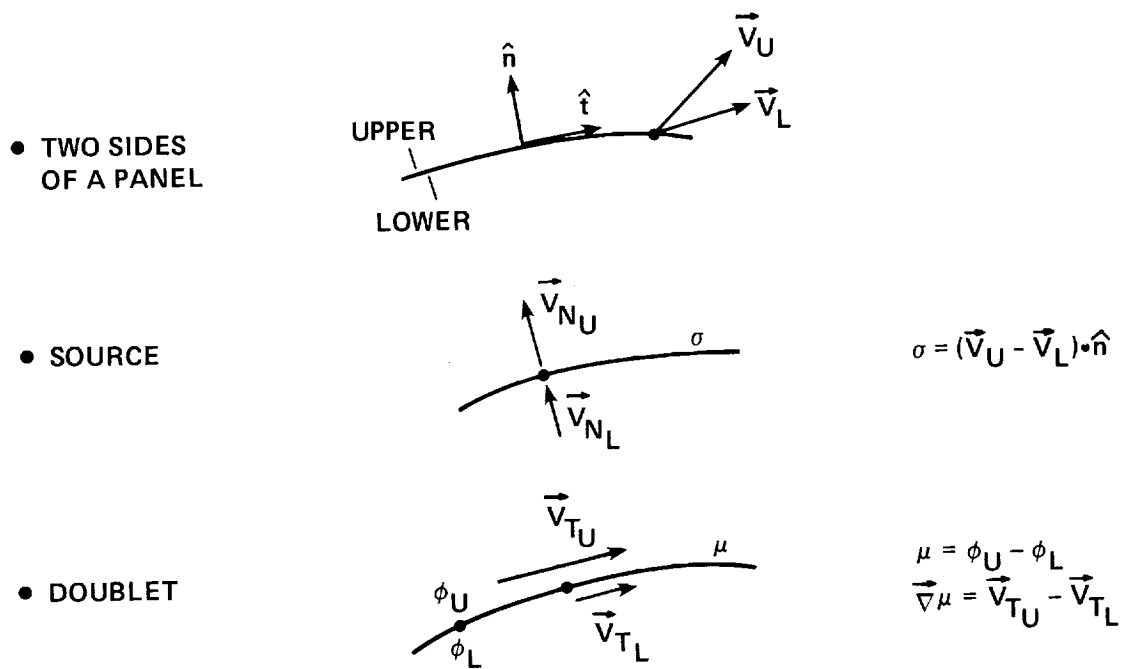
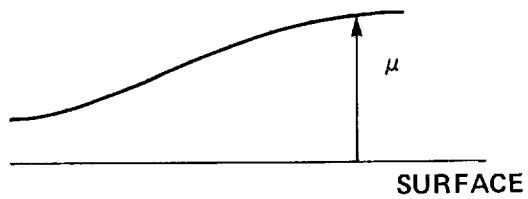


Figure 13.– The jump properties of source and doublet panels; incompressible flow.

ACTUAL



PANEL METHOD WITH
DISCONTINUOUS
DOUBLET STRENGTH

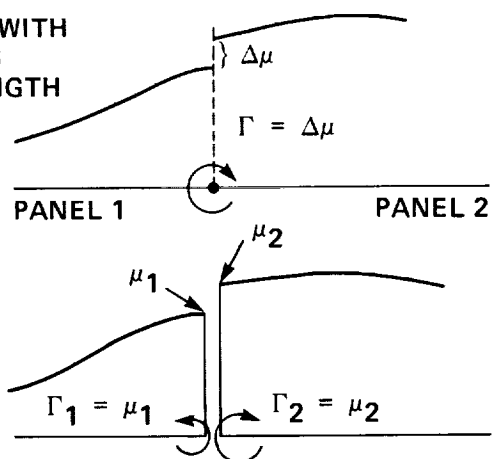


Figure 14.– The spurious line vortex that results from having a discontinuous doublet-strength distribution.

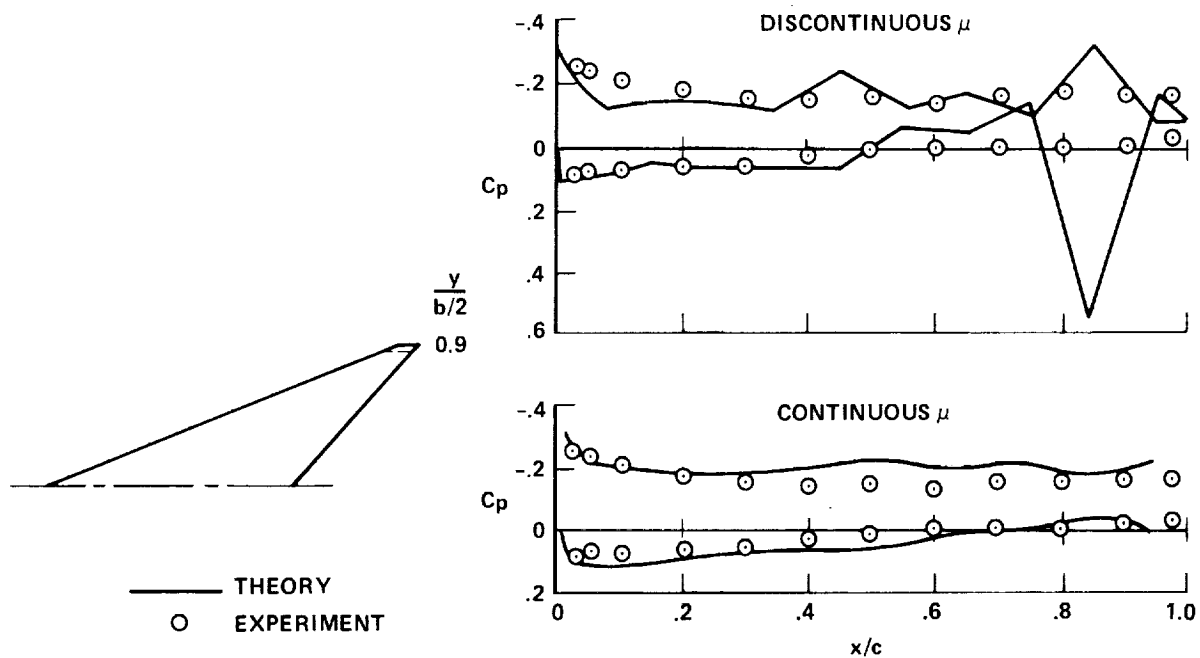


Figure 15.— Effect of discontinuous doublet strength in supersonic flow: $M_\infty = 2.05$, $\alpha = 2^\circ$, 3%-thick biconvex airfoil.

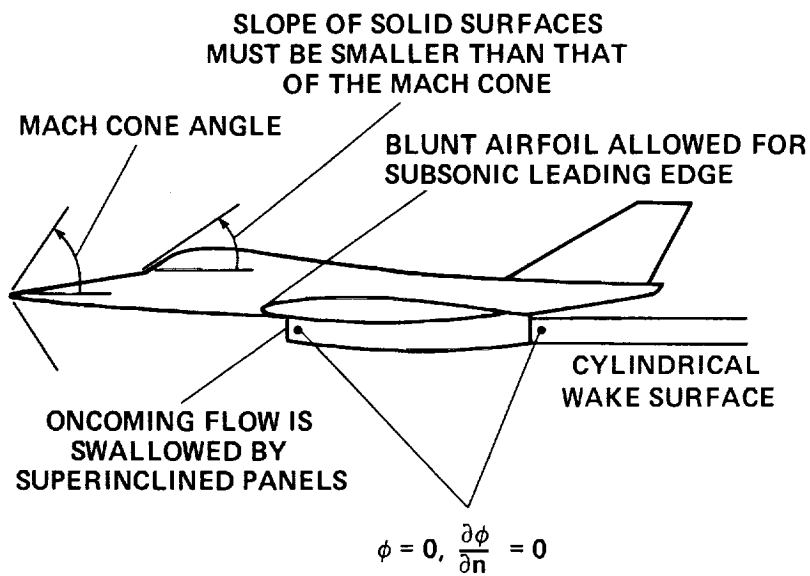
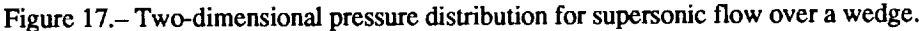


Figure 16.— Supersonic flow modeling constraints.



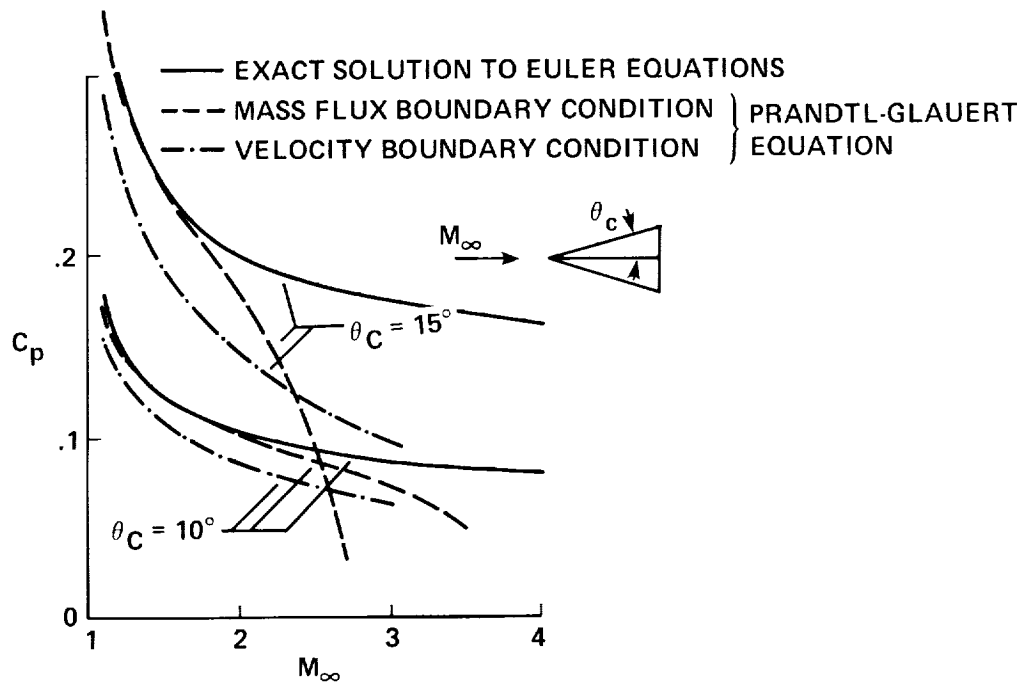


Figure 19.– Cone pressure solutions to Euler and Prandtl-Glauert equations at supersonic Mach numbers.

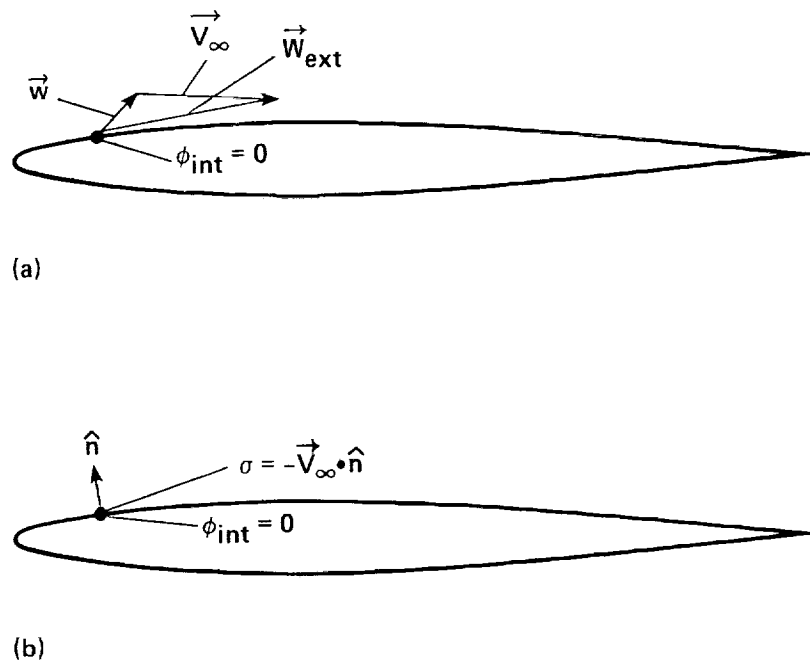


Figure 20.– Alternative ways of representing a solid surface with source/doublet panels. (a) Direct approach: $\phi_{\text{int}} = 0$, $\vec{w}_{\text{ext}} \cdot \hat{n} = 0$. (b) Indirect approach: $\phi_{\text{int}} = 0$, $\sigma = -\vec{V}_{\infty} \cdot \hat{n}$.

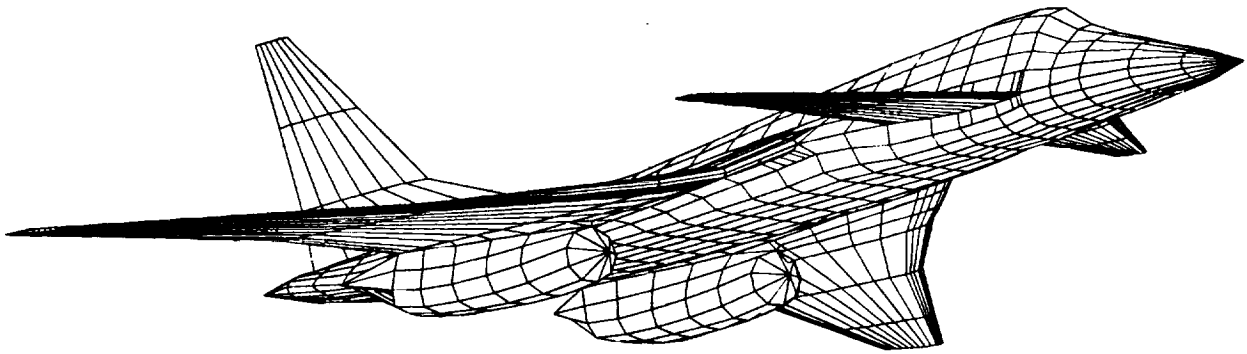
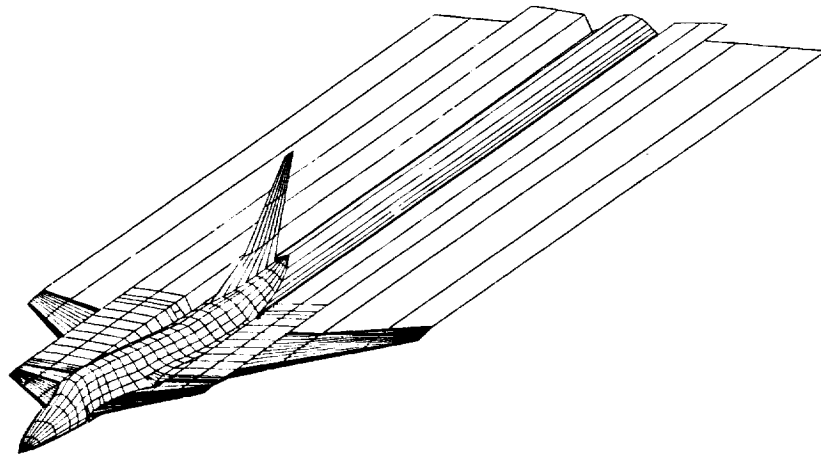
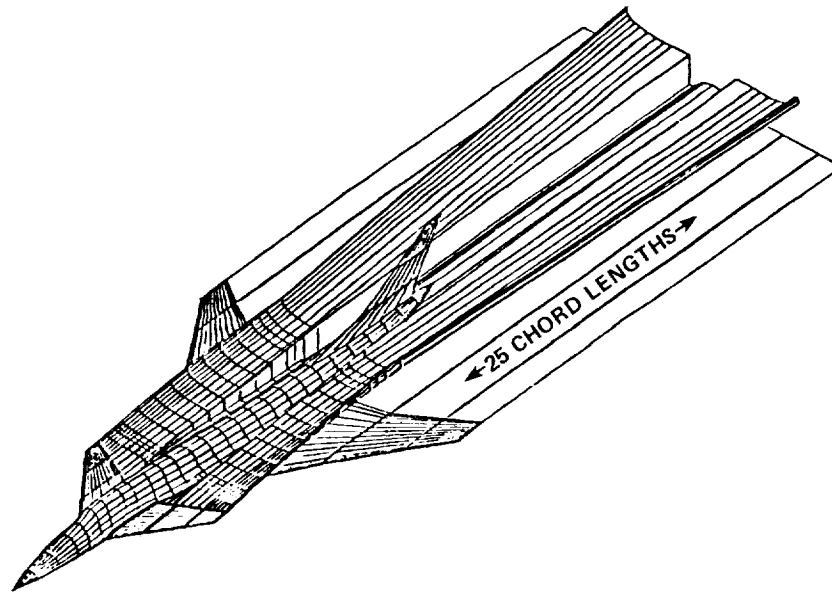


Figure 21.- PAN AIR model of supersonic fighter concept.



(a)



(b)

Figure 22.— Wake models. (a) Flat wakes in mean-chord planes. (b) Rolled-up canard wake.

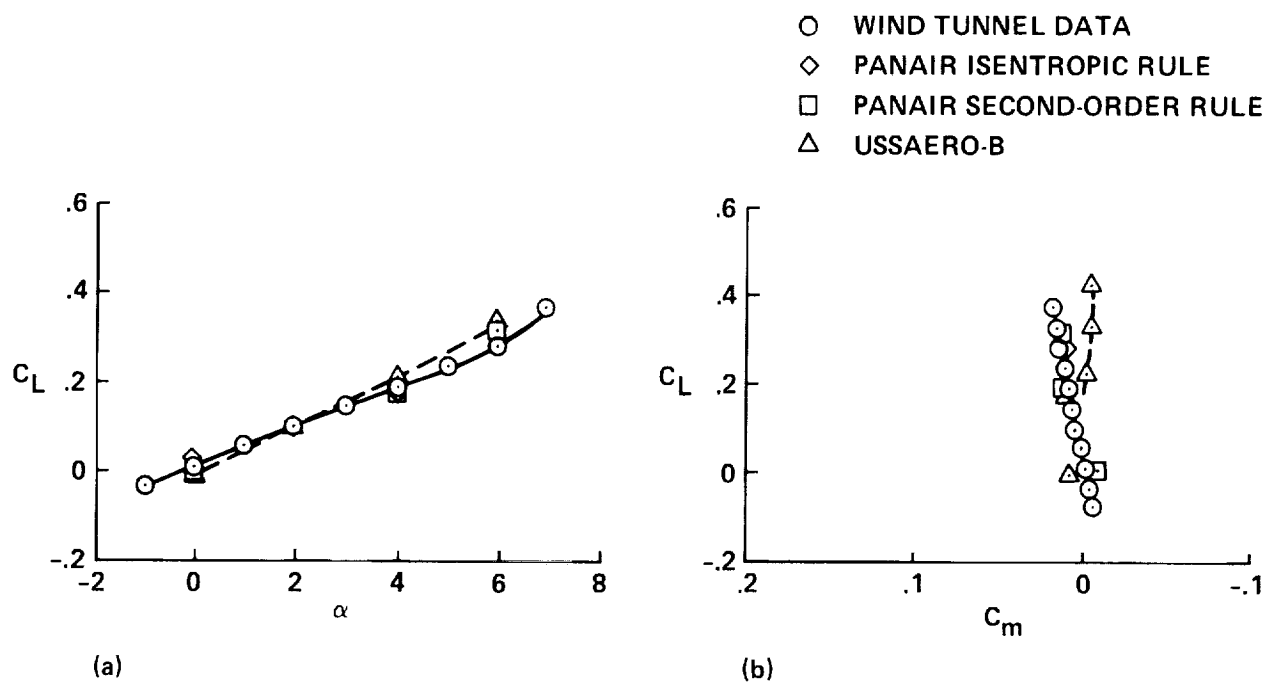


Figure 23.— Lift and moment coefficients for configuration of figure 21: $M_\infty = 2.2$. (a) Lift coefficient. (b) Pitching moment coefficient.

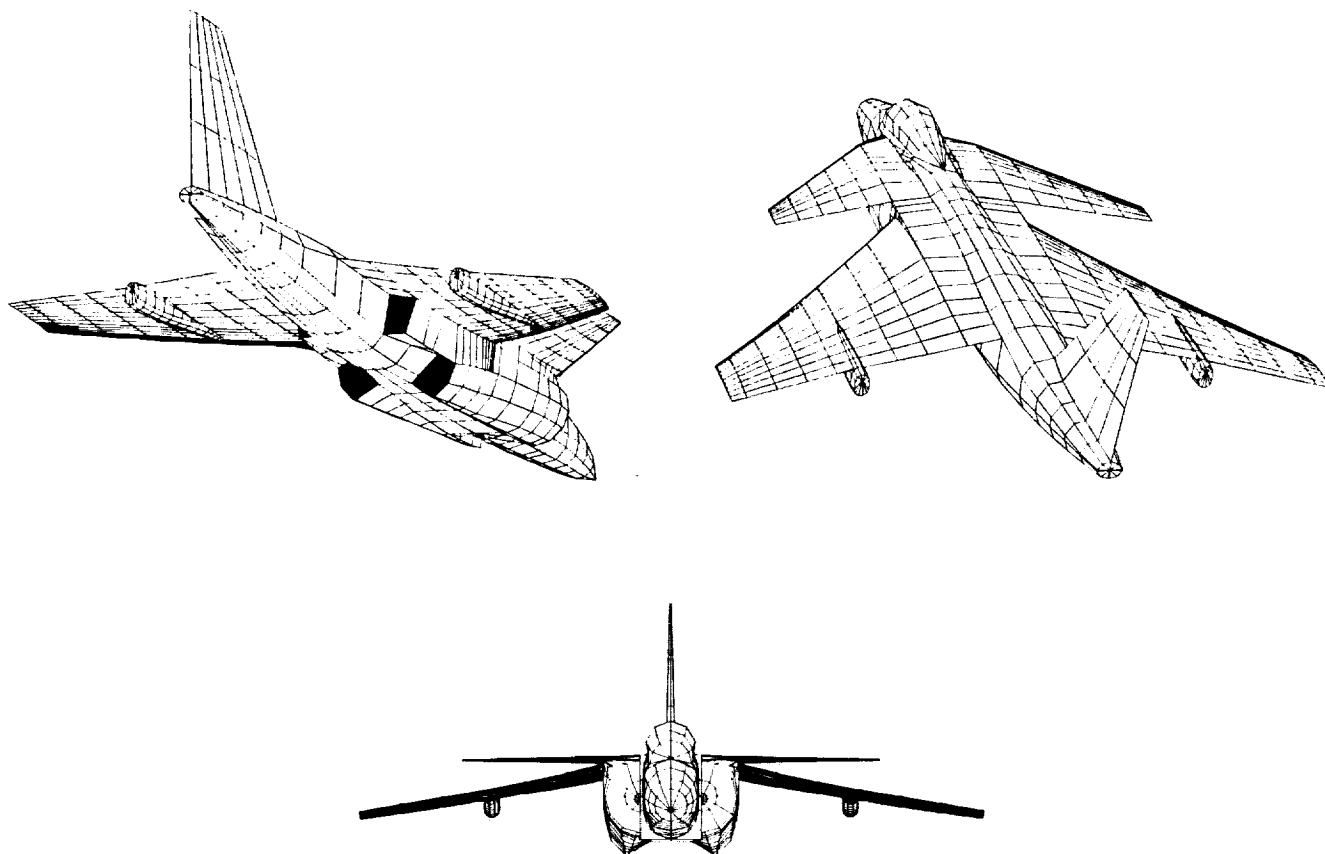


Figure 24.— A wing-canard VSTOL concept.

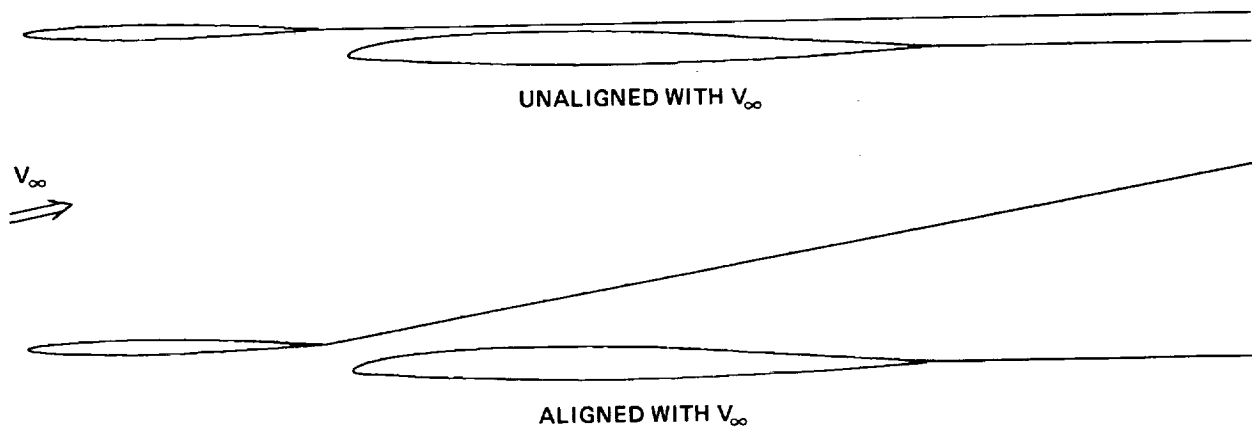


Figure 25.— Canard-wake models: $\alpha = 10^\circ$, root section.

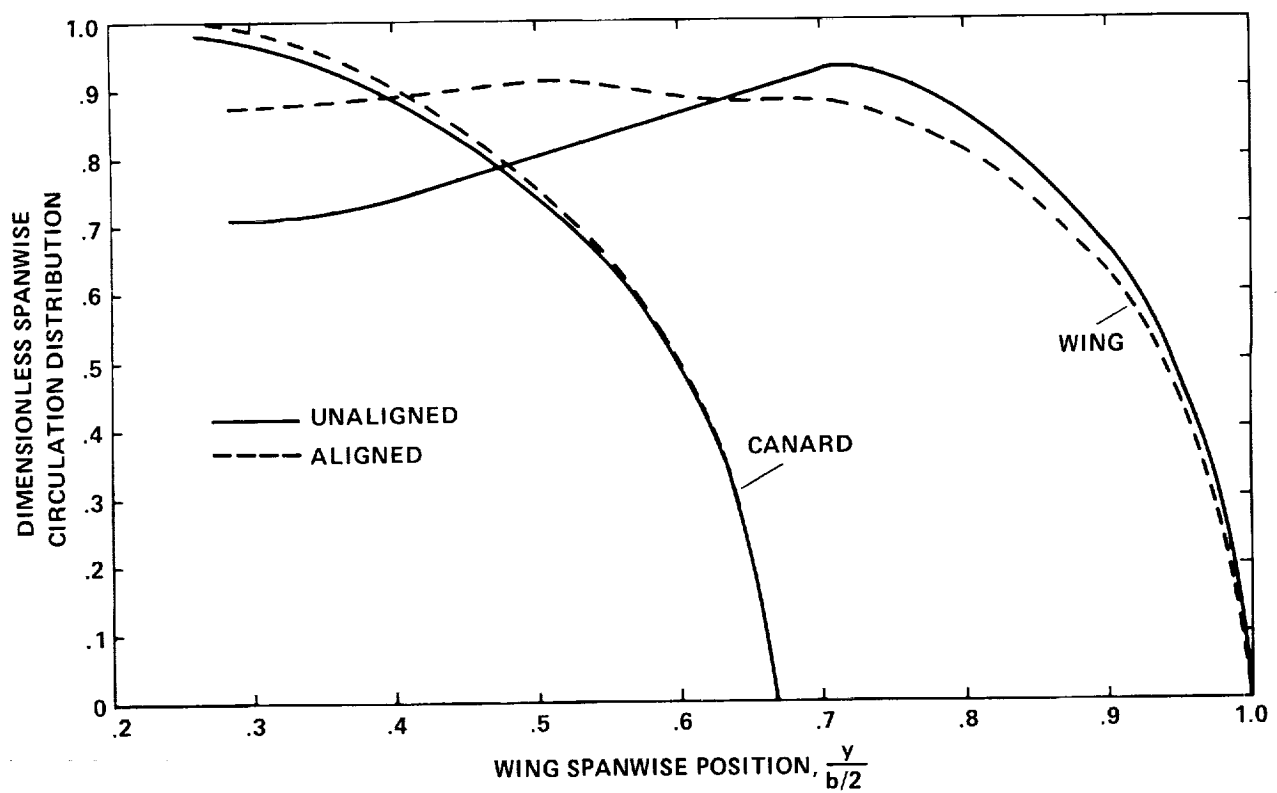


Figure 26.— Effect of canard-wake position on spanwise circulation distribution.

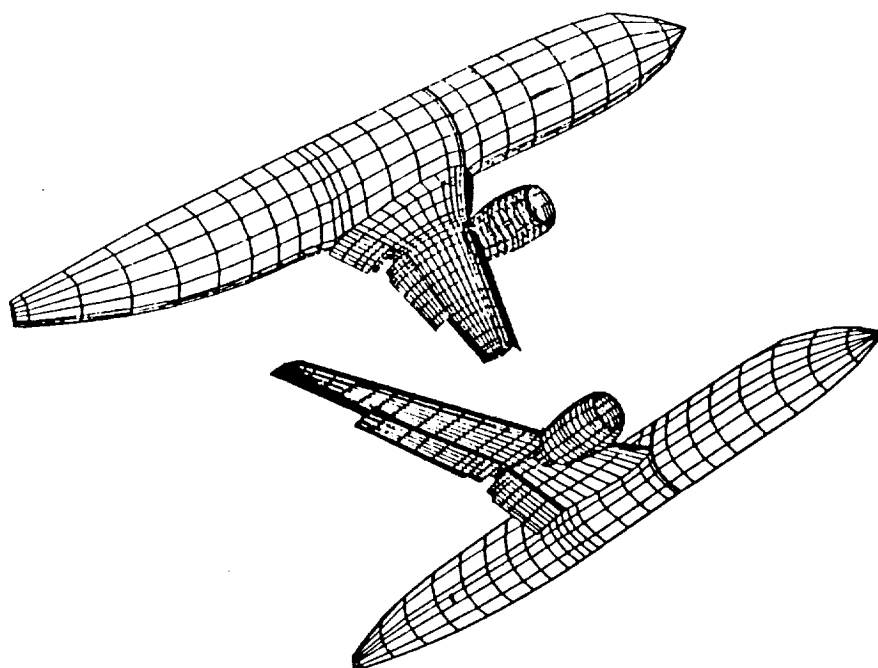


Figure 27.– Paneling of Boeing 737-300 flaps-15 configuration.

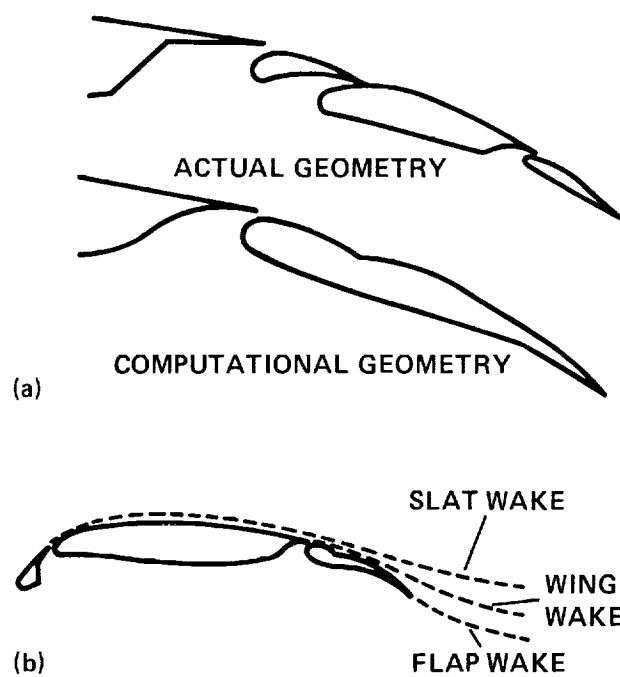


Figure 28.– Flaps-15 modeling. (a) Flap geometry. (b) Wakes.

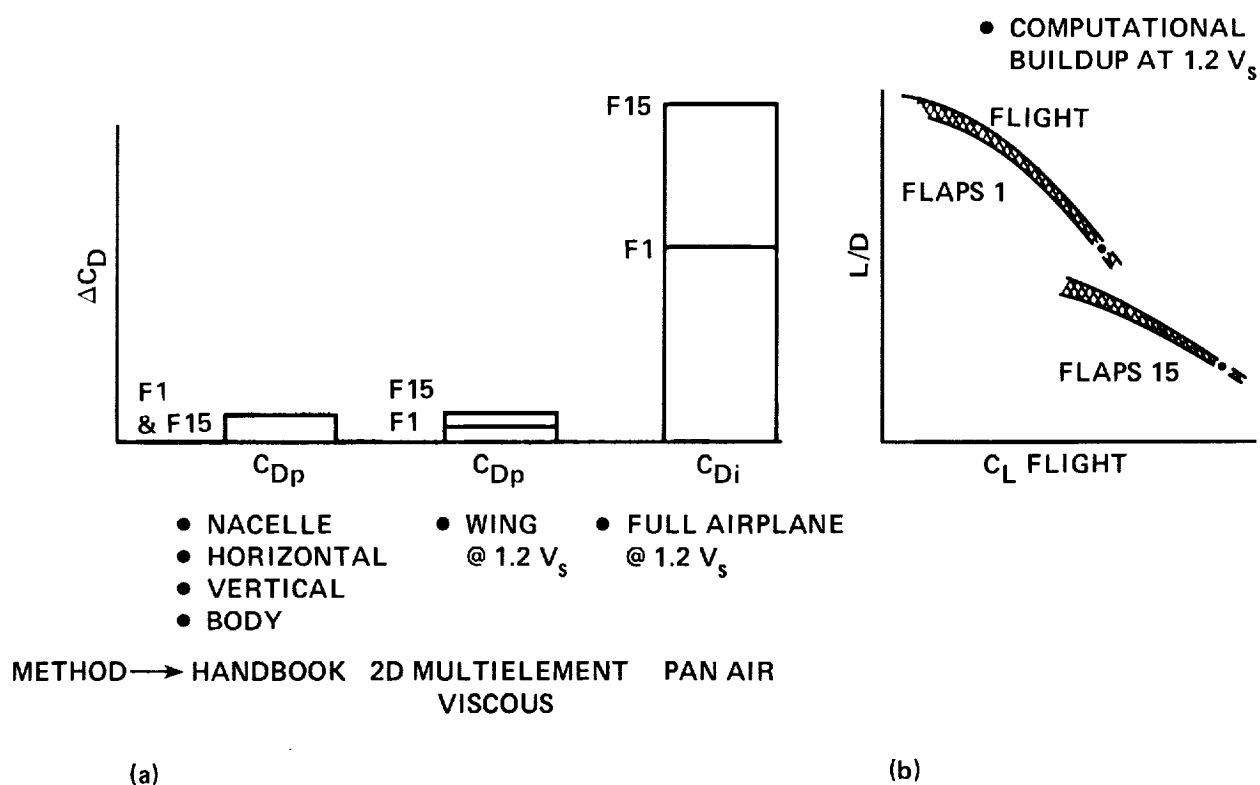
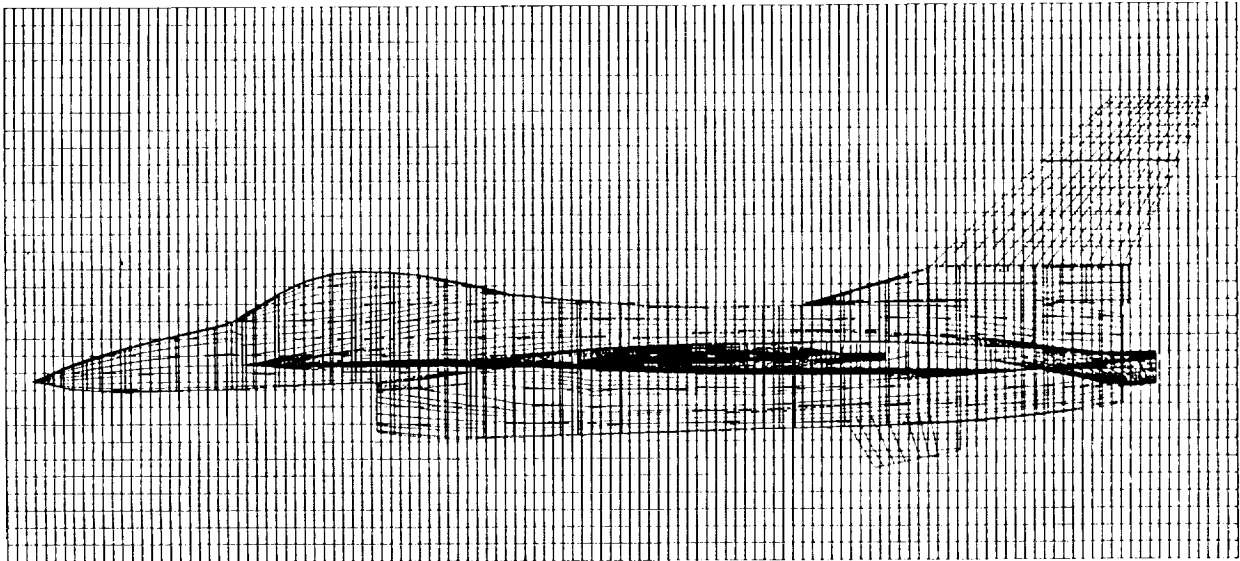
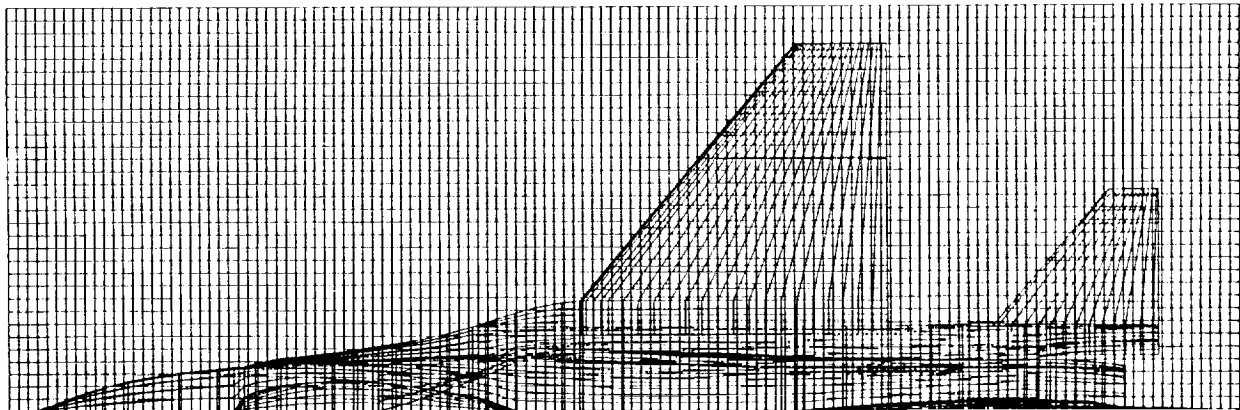


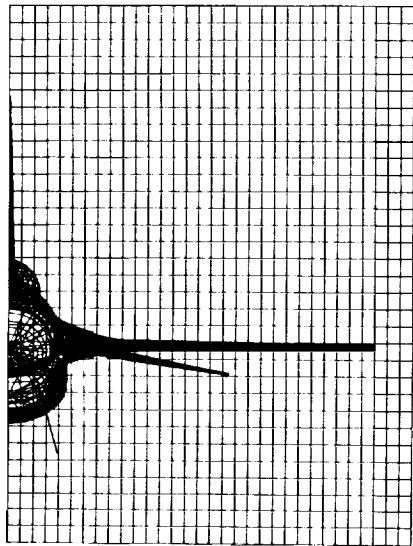
Figure 29.— Predicted and measured drag at $1.2V_s$; V_s = stall speed, C_{Dp} = profile drag, C_{Di} = induced drag, F1 = flaps-1 setting, F15 = flaps-15 setting. (a) Drag breakdown at two flap settings. (b) Aircraft lift-to-drag ratio.



(a) SIDE VIEW



(b) TOP VIEW



(c) REAR VIEW

Figure 30.— TRANAIR model of F-16A embedded in $129 \times 33 \times 33$ rectangular grid box.

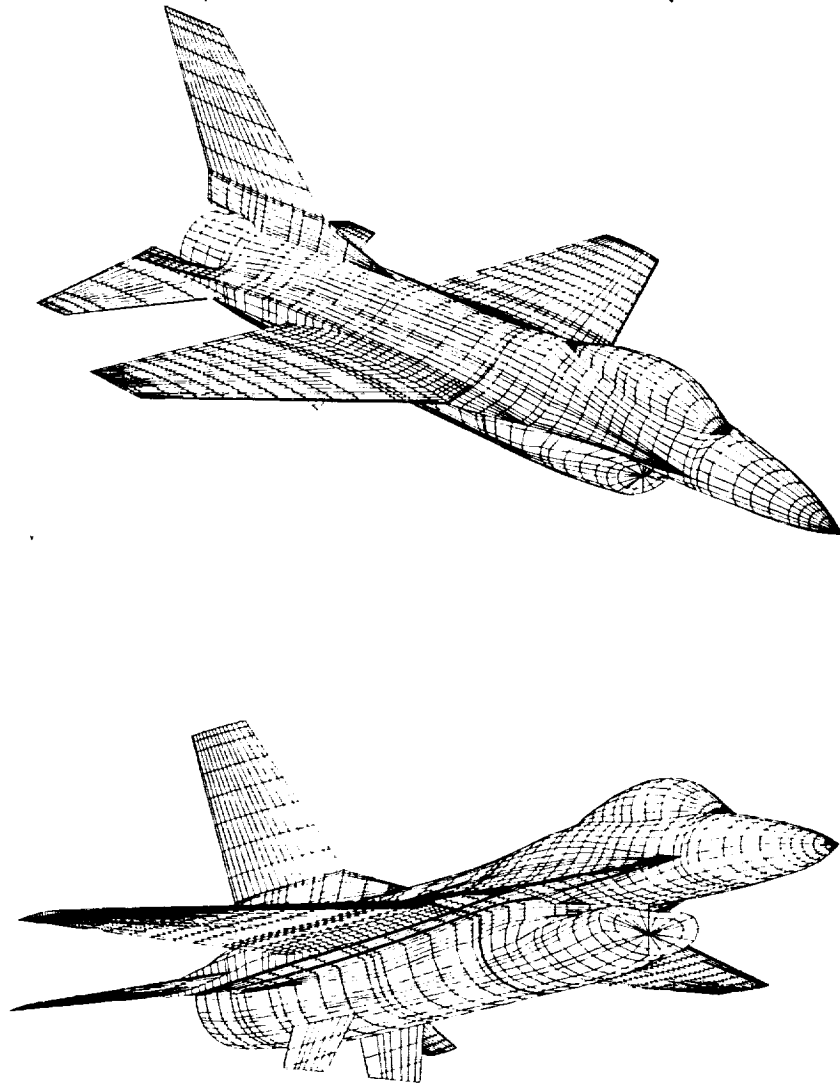


Figure 31.- PAN AIR surface panels used for input to TRANAIR.

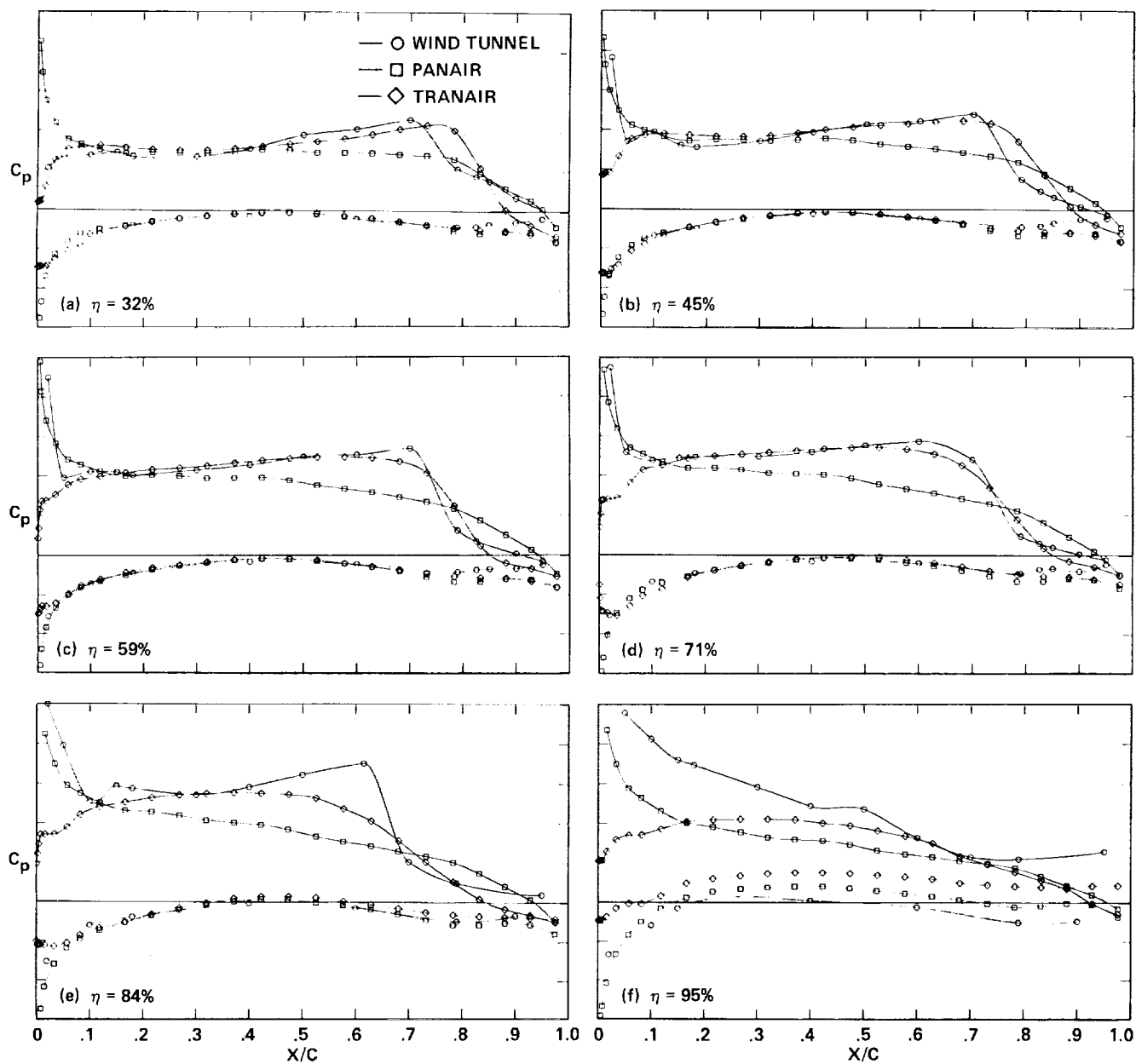


Figure 32.— F-16A supercritical wing-pressure results. Pressure distribution: $M_\infty = 0.90$, $\alpha = 4^\circ$.

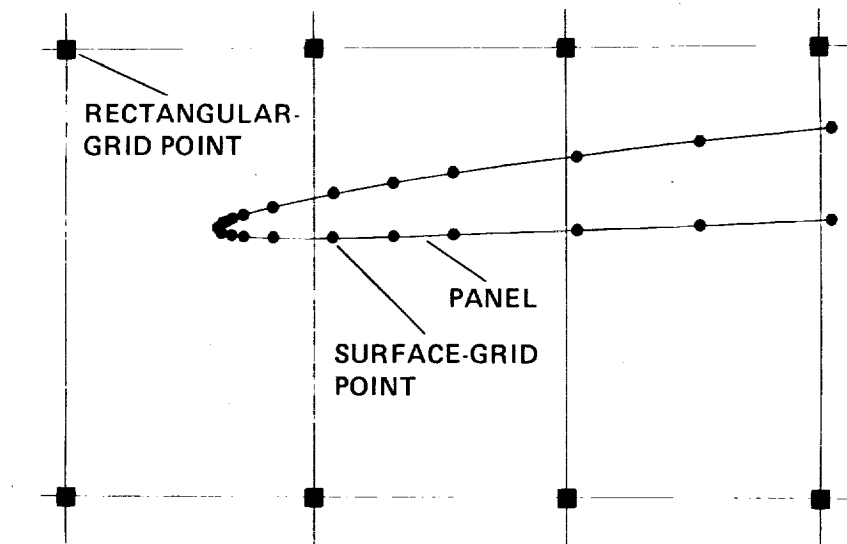
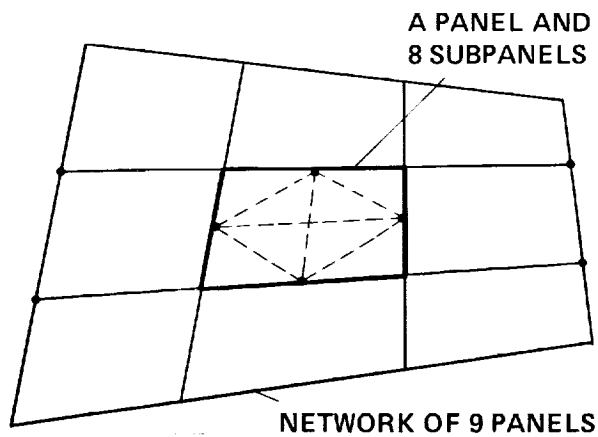


Figure 33.— Detail of leading-edge paneling embedded within the rectangular grid.

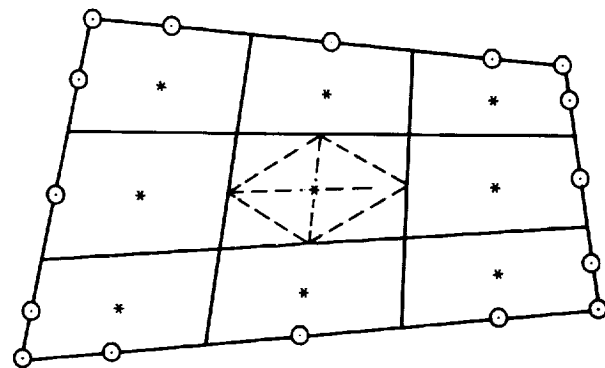
○ LOCATION OF DOUBLET SINGULARITY PARAMETERS λ_i^D

* LOCATION OF SOURCE AND DOUBLET SINGULARITY PARAMETERS λ_i^S, λ_i^D

λ_i^S AND λ_i^D ARE THE UNKNOWN, [AIC] $\{\lambda\} = \{b\}$



(a)



(b)

Figure 34.— A nine-panel network and its singularity parameter locations. (a) Network, panel, subpanels. (b) Location of network singularity parameters and corresponding control points.

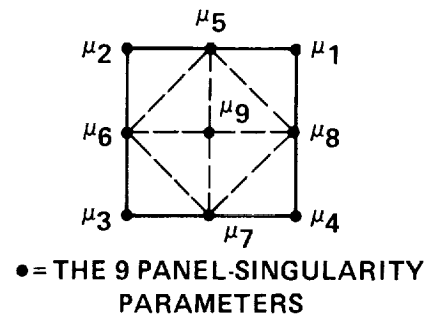
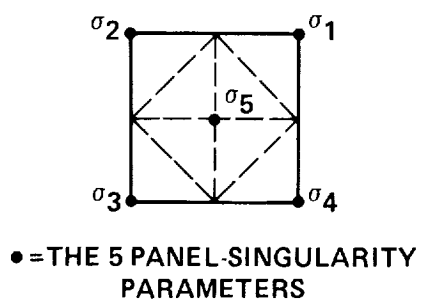
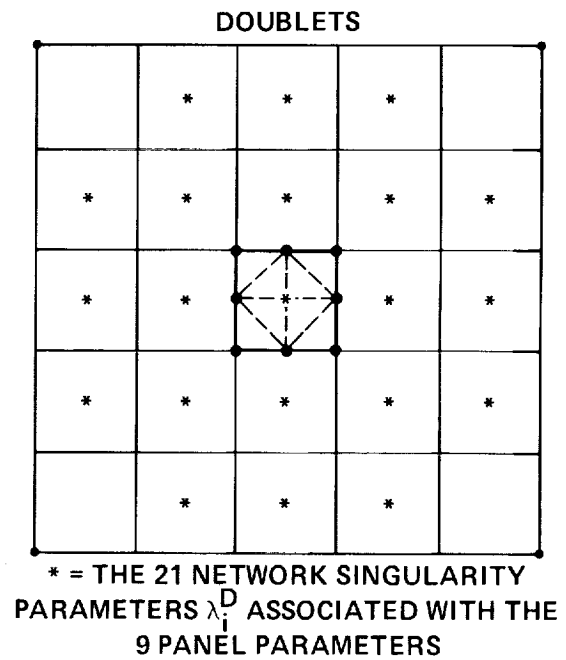
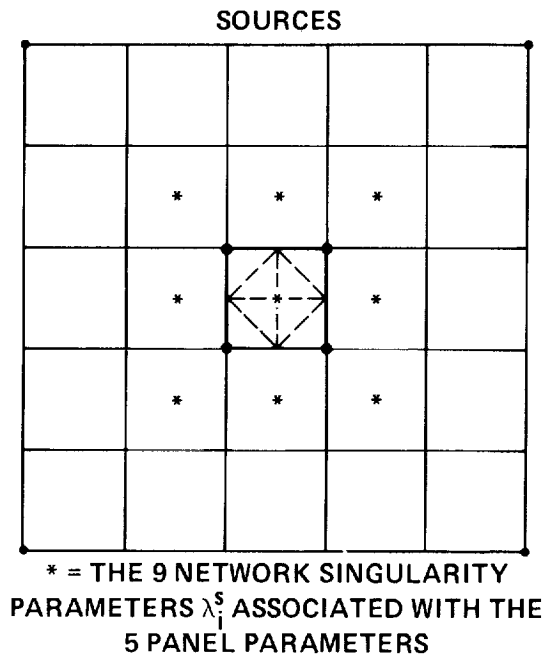


Figure 35.- Panel-singularity parameters and the associated network-singularity parameters.

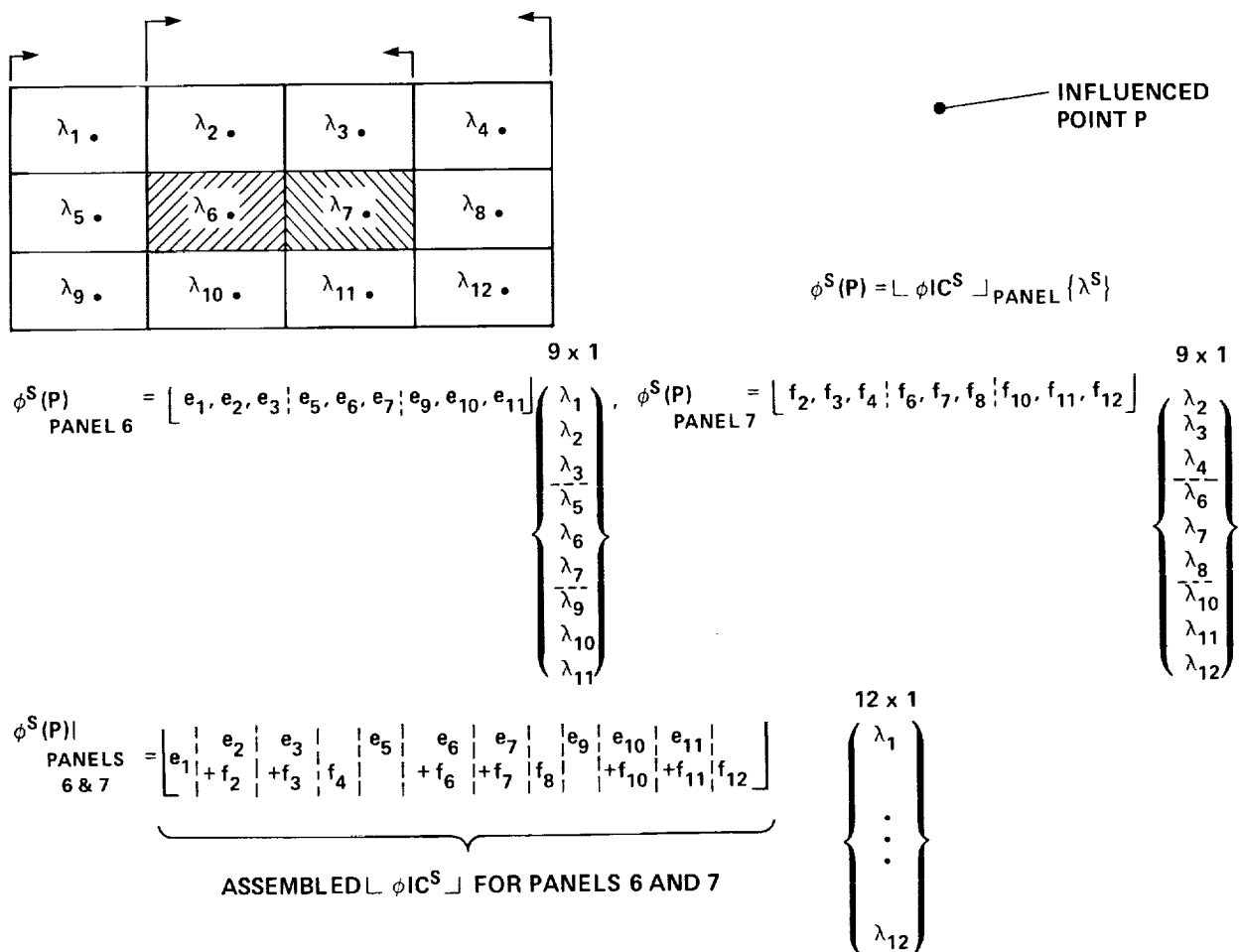


Figure 36.— The potential at P owing to the source distributions of panels 6 and 7, in terms of the associated network singularity parameters.

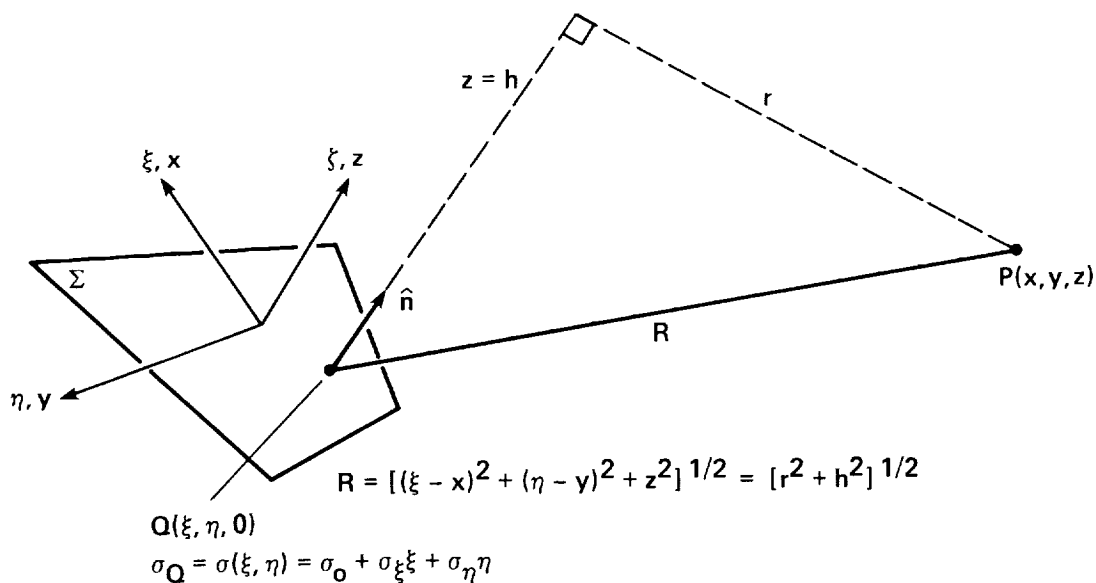


Figure 37.— Flat panel Σ with linear source σ_Q and influenced point P.

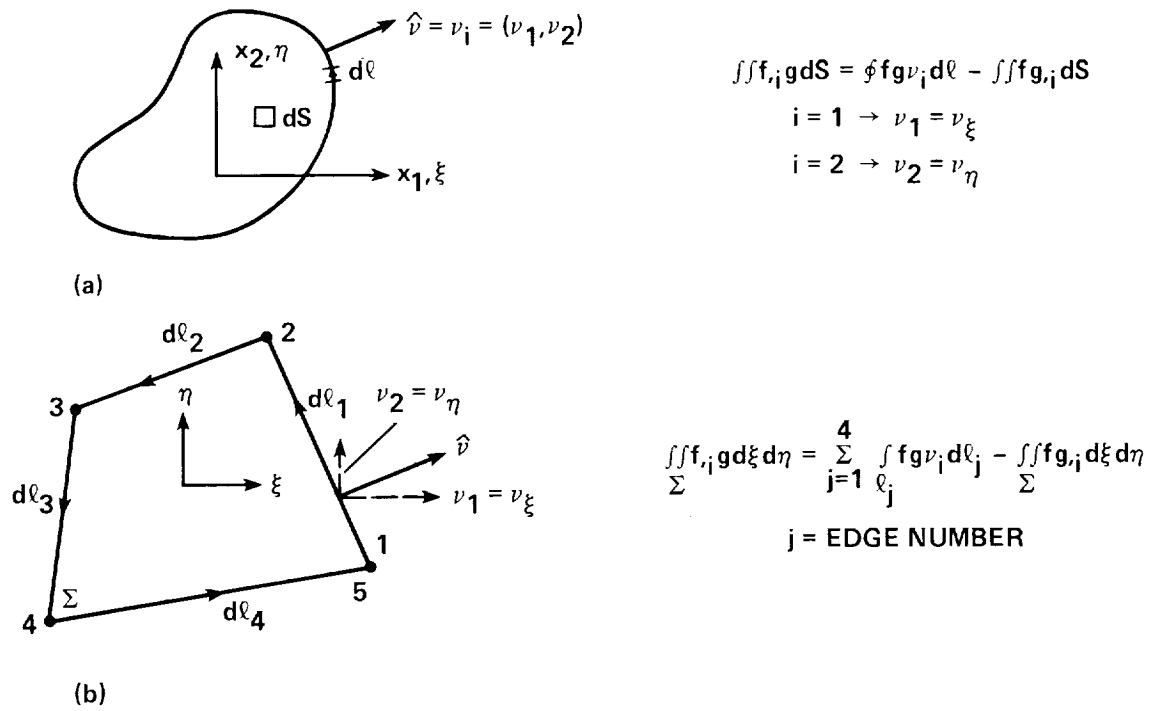


Figure 38.— Two-dimensional integration by parts. (a) General form. (b) Form for a quadrilateral panel.

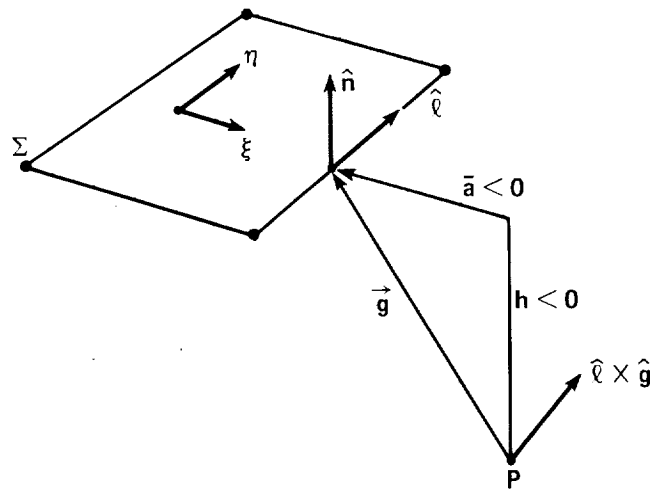


Figure 39.— The vector $\hat{\ell} \times \hat{g}$. See figure 41 for definition of \bar{a} .

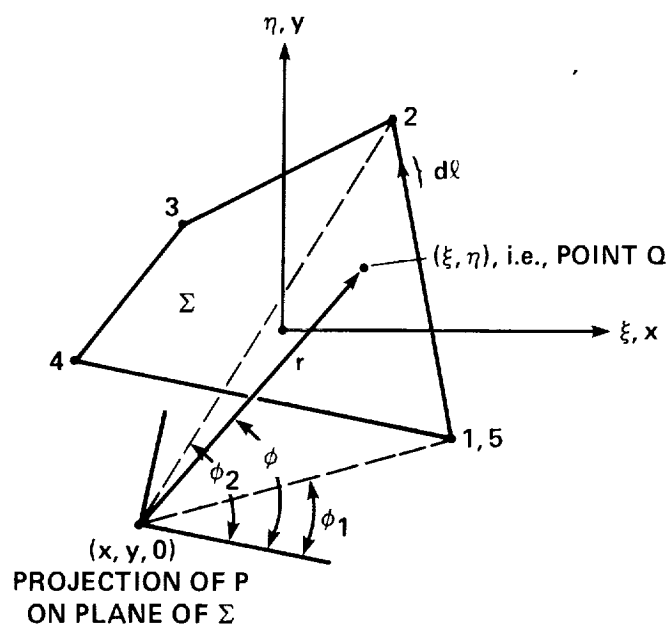


Figure 40.— Polar coordinates (r, ϕ) and edge coordinate $d\ell$.

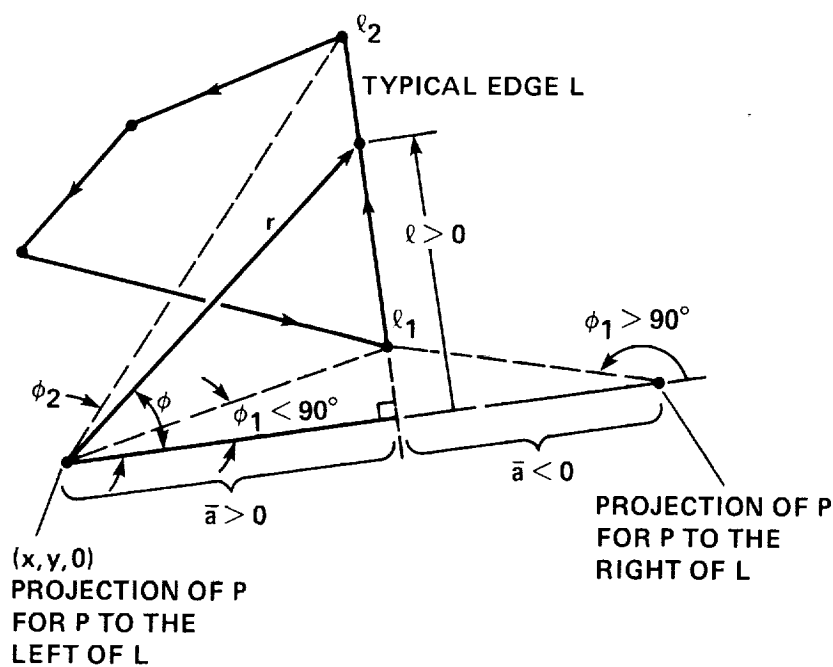


Figure 41.— Relationships between polar coordinates (r, ϕ) and the edge coordinate ℓ .

ALONG L WE HAVE

$$r^2 = \bar{a}^2 + \ell^2$$

$$\cos \phi = \frac{\bar{a}}{\sqrt{\ell^2 + \bar{a}^2}}$$

$$\sin \phi = \frac{\ell \text{sign}(\bar{a})}{\sqrt{\ell^2 + \bar{a}^2}}$$

$$\tan \phi = \ell / \bar{a}$$

$$\frac{d(\tan \phi)}{d\ell} = \sec^2 \phi \frac{d\phi}{d\ell} = \frac{1}{\bar{a}}$$

$$d\phi = \frac{\bar{a} d\ell}{\ell^2 + \bar{a}^2}$$

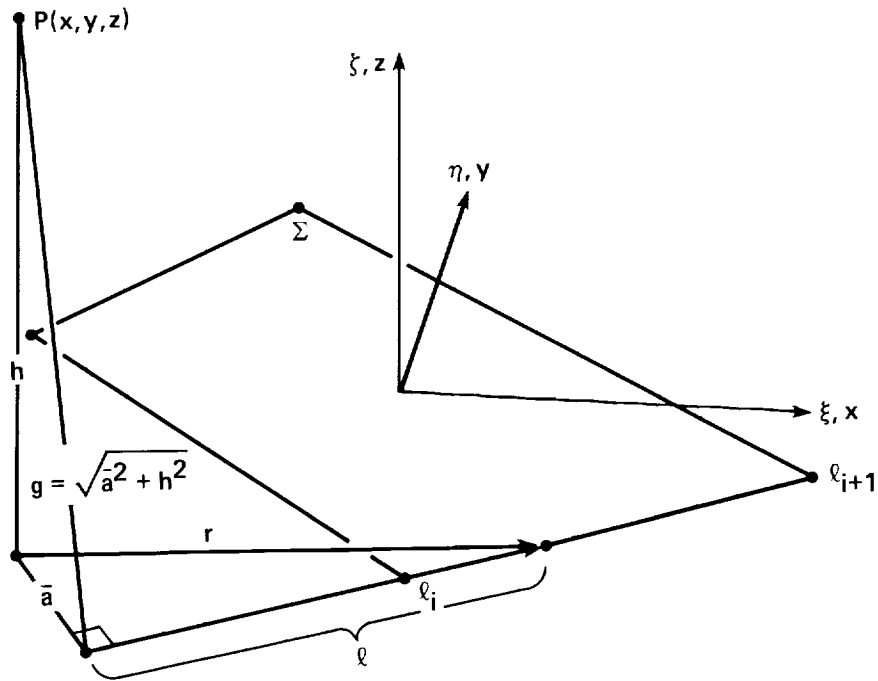


Figure 42.— The geometric quantities appearing in equations (73). As drawn, the values for h and \bar{a} are positive.

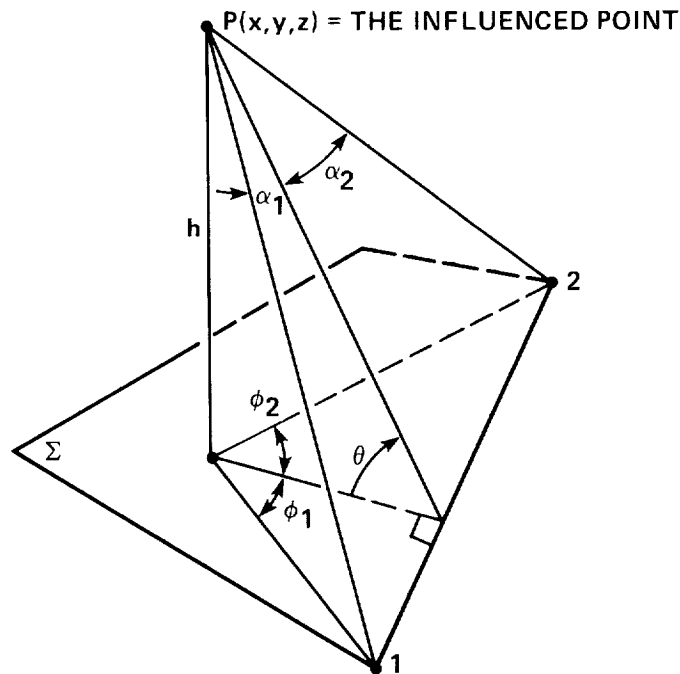


Figure 43.— The geometric quantities appearing in equation (81).

1. Report No. NASA TP-2995		2. Government Accession No.		3. Recipient's Catalog No.	
4. Title and Subtitle Panel Methods—An Introduction				5. Report Date December 1990	
				6. Performing Organization Code	
7. Author(s) Larry L. Erickson				8. Performing Organization Report No. A-89266	
				10. Work Unit No. 505-60-21	
9. Performing Organization Name and Address Ames Research Center Moffett Field, CA 94035-1000				11. Contract or Grant No.	
				13. Type of Report and Period Covered Technical Paper	
12. Sponsoring Agency Name and Address National Aeronautics and Space Administration Washington, DC 20546-0001				14. Sponsoring Agency Code	
15. Supplementary Notes Point of Contact: Larry L. Erickson, Ames Research Center, MS 227-2, Moffett Field, CA 94035-1000 (415) 604-6217 or FTS 464-6217					
16. Abstract Panel methods are numerical schemes for solving (the Prandtl-Glauert equation) for linear, inviscid, irrotational flow about aircraft flying at subsonic or supersonic speeds. The tools at the panel-method user's disposal are (1) surface panels of source-doublet-vorticity distributions that can represent nearly arbitrary geometry, and (2) extremely versatile boundary condition capabilities that can frequently be used for creative modeling. This report discusses panel-method capabilities and limitations, basic concepts common to all panel-method codes, different choices that have been made in the implementation of these concepts into working computer programs, and various modeling techniques involving boundary conditions, jump properties, and trailing wakes. An approach for extending the method to nonlinear transonic flow is also presented. Three appendixes supplement the main text. In appendix A, additional detail is provided on how the basic concepts are implemented into a specific computer program (PANAIR). In appendix B, we show how to evaluate analytically the fundamental surface integral that arises in the expressions for influence-coefficients, and evaluate its jump property. In appendix C a simple example is used to illustrate the so-called finite part of improper integrals.					
17. Key Words (Suggested by Author(s)) Panel method, Subsonic/supersonic aerodynamics, Potential flow, Sources and doublets, Aerodynamic influence coefficients, Aerodynamic analysis				18. Distribution Statement Unclassified-Unlimited Subject Category - 02	
19. Security Classif. (of this report) Unclassified	20. Security Classif. (of this page) Unclassified		21. No. of Pages 68	22. Price A04	

